Investigation of Hybrid Turbulence Modeling Techniques in the Context of Aeroacoustic Simulation

Vom Fachbereich Maschinenbau
an der Technischen Universität Darmstadt
zur Erlangung des akademischen Grades eines
Doktor-Ingenieurs (Dr.-Ing.) genehmigte

Dissertation

vorgelegt von

Xin Huang M.Sc.

aus Haicheng, VR China

Berichterstatter:	Prof. Dr. rer. nat. Michael Schäfer
Mitberichterstatter:	Prof. Dr. -Ing. Johannes Janicka
Tag der Einreichung:	22. Mai 2018
Tag der mündlichen Prüfung:	06. November 2018

Darmstadt 2018
D17

Huang, Xin: Investigation of Hybrid Turbulence Modeling Techniques in the Context of Aeroacoustic Simulation
Darmstadt, Technische Universität Darmstadt
Jahr der Veröffentlichung der Dissertation auf TUprints: 2019
URN: urn:nbn:de:tuda-tuprints-84164
Tag der mündlichen Prüfung: 06.11.2018

ACKNOWLEDGEMENT

This dissertation is a scientific work completed at the Institute of Numerical Methods in the Mechanical Engineering at Technische Universität Darmstadt. At this place, I would like to thank all people who supported and accompanied me during my doctoral study.

First, I would like to express my deepest gratitude to my advisor, Prof. Dr. rer. nat. Michael Schäfer, for giving me sufficient freedom and at the same time supporting me constantly in the research. His guidance and insightful scientific feedbacks helped me completing this thesis. I would also like to thank Prof. Dr. -Ing. Johannes Janicka for being my co-advisor and offering inspiring advices. In addition, I wish to thank the Graduiertenkolleg 1344 and the Graduate School of Computational Engineering at TU Darmstadt for providing the financial support for my doctoral study.

I wish to express my appreciation to all the people in the FNB group. Many thanks to my office colleagues, Andreas Schmitt and Stefanie Meburger, for providing a friendly environment in the office and proofreading my dissertation as well as my applications, to Artem Karev, Elena Kolb, Jessica Mariño Salguero, José Alfredo Ramírez Monares for sharing numerous scientific or funny talks during the lunch time. Special thanks go to Monika Müller, Michael Fladerer, Dr. Markus Lazanowski, Dr. -Ing Melanie Gattermayer, Carina Schuster, Birgit Seibert, Steffi Vass, Christian Schmitt for helping me solving one after another administrative and linux-related problems in the work.

I would especially like to thank my parents, Xiuling Song and Jianqi Huang, for unconditionally supporting me and being there for me all the time. My wife, Di Jin, deserves special thanks for being extremely supportive and encouraging throughout my entire PhD study. My lovely daughter, Serena Huang, gave me endless happiness outside the work. Without the support from all of you, I cannot be in this place today.

Calculations for this research were conducted on the Lichtenberg high performance computer of the TU Darmstadt.

CONTENTS

CHAPTER 1

INTRODUCTION

1.1 Motivation

Aerodynamic noise is produced in air through internal interaction of turbulent flows or external interaction with solid structures [40]. Examples are the noise generated by aircrafts or automobiles on the highway. The increase of the traffic volume makes it a non-negligible factor detrimental to the human's physical and psychological health. Consequently, the research regarding the reduction of the aerodynamic noise has gained significant importance in the last decades. In order to reduce the noise, the mechanism of the generation and the propagation process of the noise in a flow should be thoroughly studied. Solving the governing equations analytically is in most cases not possible, whereas conducting experiments in wind tunnels is less flexible considering that the aeroacoustic optimization requires numerous shape modifications of the structures. The computational aero-acoustics (CAA), a young discipline arising based on computational fluid dynamics (CFD), investigates the aeroacoustic phenomena using computational techniques and has shown great promise in recent years. Since its origin in the 1980's, CAA has become a research topic at many universities and institutes and has been applied in aerospace and in automobile industries. In comparison to experimentation, the simulation-based methods are in general less expensive and can achieve much more detailed information. As the computer power increases, it can be foreseen that CAA will play a more important role in the future. However, there are still many challenges remaining in this field. Acoustic phenomena are inherently unsteady and have a wide range of frequencies. The energy of the sound only accounts for a small fraction of that of the flow. The region of interest in aeroacoustic problems is usually in the far-field. All these adversities contribute to an increase in the computational expense or a decrease in the accuracy of the simulation results. Furthermore,

the generation of the aerodynamic noise often occur in turbulent flows, requiring special treatments and more computational efforts. The Reynolds averaged Navier-Stokes equations (RANS) method, the standard method dealing with turbulent CFD problems in industry, is not suitable for CAA problems, while the computationally expensive large-eddy simulation (LES) method is still far from being applicable for engineering problems. Hence, more efficient strategies capable of solving CAA problems in turbulent flows need to be developed. The use of hybrid LES/RANS models is quite promising, since the hybrid modeling techniques combines the advantages of higher accuracy of LES and lower computational cost of RANS. Therefore, the study of hybrid modeling techniques for aeroacoustic simulations is of special importance.

1.2 State of the Art

1.2.1 Turbulence Modeling

Thanks to the growing power of the computing technology, CFD has been increasingly used to solve complex flow problems. Nevertheless, turbulence still constitutes a challenging task due to its chaotic, irregular and multi-scale characteristics.

The most common methods dealing with turbulent problems are the direct numerical simulation (DNS) method, LES models and RANS models. The DNS method solves the Navier-Stokes equations without using any additional modeling techniques. Therefore, the DNS method is accurate but extremely time-consuming. For academic research, DNS is an impressive tool capable of providing reliable results. However, for engineering problems, the range of scales to be resolved is too wide. Studies indicate that DNS is not applicable for engineering problems until the later part of this century [89].

The LES technique, proposed by Smagorinsky [74], resolves the most energy containing motions, while modeling the small motions using sub-grid scale (SGS) models. In comparison with DNS, the LES technique reduces the computational cost to some extent and has been regarded as a viable alternative to the DNS method in the research area. The original Smagorinsky SGS model [74] is still widely used since it yields very successful results. The Smagorinsky constant in this SGS model needs to be calibrated for different flows. An improvement was made by Germano et al. [26] so that the Smagorinsky constant can be adapted dynamically during the simulation.

The RANS models are extremely popular in the industry due to the fact that it is less computationally demanding. Instead of the original Navier-Stokes equations, the Reynolds averaged Navier-Stokes equations are solved, which are derived by decomposing the flow into a mean part and a fluctuating part [62]. Therefore, the RANS models deliver statistically mean flows, which are in most cases sufficient for engineering problems.

The hybrid LES/RANS models are created in the hope of combining the advantages of the LES model and the RANS model. As one of the most successful hybrid turbulence models, the detached eddy simulation (DES) model has been proposed by Spalart et al. [79] in 1997. This approach adjusts the dissipation term in the equation for the turbulence kinetic energy k with the help of a length scale. By doing so, the DES model can switch between a RANS model an a LES model depending upon the local grid resolution. This approach has been then modified by Spalart et al. [78] to the delayed detached eddy simulation (DDES), allowing it to operate in a RANS mode in the boundary layer no matter how fine the grid here is. The Very Large Eddy Simulation (VLES), proposed by Speziele [80], damps the Reynolds stress tensor in the Reynolds Averaged Navier-Stokes equations and therefore can switch between DNS and a RANS model. As a variant of the VLES, the Limited Numerical Scales (LNS) model has been proposed by Batten et al. [3, 4]. The LNS model has been studied for various flow problems [68] and acoustic problems [5] with very promising results.

1.2.2 Computational Aero-Acoustics

Acoustics, as the science of sound, dates back to the time of ancient Greece, when Aristotle understood that the propagation of sound relies on the existence of a medium [66]. In the modern history of acoustics, John William Strutt, 3rd Baron Rayleigh, stands out with his epochal work, the theory of sound [59]. He investigated aerial vibrations and the waves in fluids using mathematical methodologies [66].

Aero-acoustics branched off from the acoustics with the pioneering work of Sir James Lighthill, on sound generated aerodynamically I/II [45, 46]. His investigations of the aerodynamic sound generated by turbulent flows are of great importance in the field of nonlinear acoustics. The mathematical model bearing his name, the Lighthill's analogy, is still one of the most important models solving aeroacoustic problems. The Lighthill's analogy is extended to the Curle's analogy and the Ffowcs Williams-Hawking's analogy by considering the existence of rigid surfaces in the governing equations. The difference between these two analogies is that the Curle's analogy considers fixed walls while the Ffowcs Williams-Hawkings (FW-H) analogy studies moving walls [64].

With the rapid development of CFD, the application of numerical techniques in the calculation of aero-acoustics gained more and more interest, leading to the emergence of the CAA [82]. In general, there exist two approaches dealing with aeroacoustic problems: the direct noise computation (DNC) and the hybrid approach [40]. The DNC approach solves the compressible Navier-Stokes equations to determine the fluid field and the acoustic field at the same time [12]. This approach is able to deliver more detailed information in the acoustic field, and hence can be used to study the mechanisms of the generation and propagation processes of noise. However, due to the significant difference at both length and time scales of the flow and acoustic field,

the DNC method is considered inefficient especially for low Mach number flows. The hybrid approach separates the simulation of the flow and the acoustics and couples them through acoustic sources. The acoustic analogies, including the Lighthill's ananogy, the Curle's analogy and the FW-H analogy, belong to the hybrid approach. The advantage of this approach is that it is less computationally expensive compared to the DNC approach and therefore has more potential to be widely applied in the industry.

A relatively new hybrid approach, called expansion about incompressible flow (EIF), is developed by Hardin and Pope [29]. In this approach, the compressible flow field is split into an incompressible flow field and perturbation quantities. Based on the EIF technique, Shen and Sørensen derived the equations governing the aeroacoustic quantities, also denoted as the Linearized Euler Equations (LEE) [72, 73].

For aeroacoustic simulations, the DNS cannot be applied in most cases due to its unaffordable computational time. In order to reduce the computational cost, a turbulence model is usually adopted to characterize the unresolved turbulence scales. Baily and Juvé combined the LEE method with the $k - \epsilon$ RANS turbulence model for the flow field [13]. However, due to the loss of turbulence information, the RANS turbulence model is generally not suitable to solve the aeroacoustic problems. The LES model has also been used to calculate the aeroacoustic sources. Kornhaas and Schäfer studied the numerical efficiency of the LEE scheme coupled with the LES model for the flow simulation [41]. Flemming, Sadiki and Janicka investigated the LES/CAA approach for the simulation of the aerodynamic noise generated by reactive flows [23]. However, the high computational cost of the LES model hinders its wide application in the CAA for engineering problems. More recent studies have been focusing on hybrid LES/RANS turbulence models. Langtry et al. studied the Detached Eddy Simulation (DES) model in the simulation of flap edge noise [42]. Wang et al. applied the IDDES model to simulate the landing-gear noise [91]. Bonneau et al. investigated the turbofan noise using a zonal detached eddy simulation model [8].

1.3 Objectives of this Work

A reliable solution of the broad band aeroacoustic problems requires accurate solution of the underlying flow problems, which cannot be achieved by the RANS models. The DNS method and the LES model are not applicable for engineering problems in short time. Some of the hybrid LES/RANS models, e.g. the DES model and the IDDES model, have been applied in the aeroacoustic simulations. However, a guideline of the usage of the hybrid LES/RANS models in the aeroacoustic problems is still missing. The objective of this work is to enhance the understanding of the application of hybrid LES/RANS turbulence modeling strategies in the aeroacoustic simulations. For this purpose, a new hybrid LES/RANS turbulence model, the limited numerical scales (LNS) model, is first implemented and validated using a benchmark test case, which is

then thoroughly studied for aeroacoustic simulations and compared with RANS models, the LES model and an existing hybrid LES/RANS model, the very large eddy simulation (VLES) model. In order to compensate the loss of acoustic components of high frequency caused by using turbulence models, a synthetic method is implemented and investigated in combination with the hybrid LES/RANS model.

1.4 Structure of this Work

The structure of the present work is as follows:

Chapter 1 addresses the motivation and the goals of the present work. In addition, an overview of the previous studies and the state of the art is also given.

Chapter 2 introduces the fundamentals relevant for the present study, including the governing equations for the flows and for the acoustics.

Chapter 3 presents the numerical methods used to solve the governing equations introduced in the Chapter 2.

Chapter 4 describes the turbulence models used in this work, including the existing hybrid LES/RANS models in FASTEST and the underlying RANS models.

Chapter 5 introduces the implementation and the validation of the LNS turbulence model.

Chapter 6 demonstrates the coupling strategy of the flow solver and the acoustic solver, and verifies the new implemented coupling part using two test cases.

Chapter 7 investigates the synthetic method for the reconstruction of the high frequency turbulence. The implementation is also validated using a benchmark test case.

Chapter 8 shows the comparison of hybrid LES/RANS models in the aeroacoustic problems in two test cases.

Chapter 9 summarizes the findings and gives an outlook for the future work.

CHAPTER 2

FUNDAMENTALS

In this chapter, the fundamental equations governing the fluid dynamics and aero-acoustics are introduced. Concerning the computational fluid dynamics (CFD), the conservation equations of mass and momentum as well as the material law and the assumptions necessary to close the equation system are presented. Afterwards, the governing equations for the computational aero-acoustics (CAA) are presented. All differential equations in this chapter are written using Einstein's notation.

2.1 Fundamentals of Fluid Mechanics

The law of mass conservation, demonstrating that the mass cannot be created nor disappear, can be given as [81]

$$\frac{\mathrm{D}}{\mathrm{D}t} \iiint_V \rho \, \mathrm{d}V = 0, \tag{2.1}$$

with density ρ and volume V. Its differential form

$$\frac{\partial \rho}{\partial t} + \frac{\partial \left(\rho u_i\right)}{\partial x_i} = 0 \tag{2.2}$$

is also called the continuity equation, where t is time, x_i are the spatial coordinates and u_i are the velocity components in the i-directions.

The momentum conservation indicates the relation of the forces acting on the fluid

and the corresponding change of momentum, which is formulated as

$$\underbrace{\frac{\mathrm{D}}{\mathrm{D}t}\iiint_V \rho u_i \,\mathrm{d}V}_{\text{change of momentum}} = \underbrace{\iint_S T_{ij} n_j \,\mathrm{d}S}_{\text{surface forces}} + \underbrace{\iiint_V \rho f_i \,\mathrm{d}V}_{\text{volume forces}}, \tag{2.3}$$

where T_{ij} is the Cauchy stress tensor, f_i is the volume force per mass unit. The differential form of the momentum conservation equation reads

$$\frac{\partial\left(\rho u_i\right)}{\partial t} + \frac{\partial\left(\rho u_i u_j\right)}{\partial x_j} = \frac{\partial T_{ij}}{\partial x_j} + \rho f_i. \tag{2.4}$$

The fluids discussed in the present work are regarded as incompressible, i.e. the Mach number fulfills the condition

$$\mathrm{Ma} = \frac{\bar{u}}{c} < 0.3,$$

with the characteristic flow velocity $\bar{u}$ and the speed of sound c.

For incompressible fluids, the mass conservation equation can be simplified to

$$\frac{\partial u_i^{\mathrm{inc}}}{\partial x_i} = 0, \tag{2.5}$$

where u_i^{inc} denotes the velocity components in the incompressible fluid.

Moreover, the investigation in this work is restricted to Newtonian fluids, for which the Cauchy stress tensor fulfills the relation

$$T_{ij} = \mu\left(\frac{\partial u_i}{\partial x_j} + \frac{\partial u_j}{\partial x_i}\right) - p\delta_{ij}, \tag{2.6}$$

with pressure p and the dynamic viscosity μ.

Considering the incompressibility and the material property, the momentum conservation equation can be rewritten as

$$\frac{\partial\left(\rho^{\mathrm{inc}} u_i^{\mathrm{inc}}\right)}{\partial t} + \frac{\partial\left(\rho^{\mathrm{inc}} u_i^{\mathrm{inc}} u_j^{\mathrm{inc}}\right)}{\partial x_j} = \frac{\partial}{\partial x_j}\left[\mu\left(\frac{\partial u_i^{\mathrm{inc}}}{\partial x_j} + \frac{\partial u_j^{\mathrm{inc}}}{\partial x_i}\right)\right] - \frac{\partial p^{\mathrm{inc}}}{\partial x_i} + \rho^{\mathrm{inc}} f_i. \tag{2.7}$$

A detailed description about the topics in this chapter can be found in e.g [81], [20], [56] and [2].

2.2 Fundamentals of Aero-acoustics

Aero-acoustics mainly studies the generation and propagation of sound produced in unsteady flows. In this section, the relevant fundamentals concerning aero-acoustics are described.

The acoustic field can be described by the acoustic pressure p^{ac}, the acoustic density ρ^{ac} and the acoustic velocity u_i^{ac}, which are the perturbations of the pressure, the density and the velocity caused by sound waves, respectively.

In practice the acoustic pressure is rarely used, because the humans' sensation of sound is proportional to the logarithm of the acoustic pressure. Instead, a sound pressure level (SPL) L_p with unit decibel (dB) is more commonly applied, which is defined by [40]

$$L_p = 10 \cdot \lg \frac{\left(p_{\mathit{eff}}^{\mathrm{ac}}\right)^2}{\left(p_{\mathit{ref}}^{\mathrm{ac}}\right)^2} = 20 \cdot \lg \frac{p_{\mathit{eff}}^{\mathrm{ac}}}{p_{\mathit{ref}}^{\mathrm{ac}}}, \tag{2.8}$$

where $p_{\mathit{ref}}^{\mathrm{ac}}$ is a reference acoustic pressure, which is usually set to 2×10^{-5} Pa in air and $p_{\mathit{eff}}^{\mathrm{ac}}$ is the effective acoustic pressure defined by [40]

$$p_{\mathit{eff}}^{\mathrm{ac}} = \sqrt{\frac{1}{T} \int_{t=0}^{T} (p^{\mathrm{ac}}(t))^2 \, \mathrm{d}t}. \tag{2.9}$$

In order to acquire the acoustic quantities, many different approaches have been developed. In the subsequent sections, the most common methods are introduced.

2.2.1 Direct Noise Computation

The direct noise computation (DNC) method solves the compressible Navier-Stokes equations directly to calculate the acoustic variables. This method is extremely computationally expensive, since the requirements on the space and time resolutions are both very high, caused by the multi-scale problem illustrated in Fig. 2.1. The propagation speed of the acoustic variables is usually much greater than that of the flow, while the acoustic energy is negligibly small compared to that of the flow. Therefore, this method is less attractive for aeroacoustic simulations [40].

2.2.2 Hybrid Methods

In hybrid methods, the acoustic variables are calculated in two steps: First, the flow motions are obtained by solving the Navier-Stokes equations, which are used to calculate the acoustic source term. Second, the acoustic variables are calculated by solving the governing equations of the acoustics.

Compared to the DNC method, the hybrid methods are more computationally effective, because the flow domain can be solved using much coarser spatial and temporal discretizations [40].

The governing equations for the acoustic variables are derived starting from the expansion about the incompressible flow (EIF). The idea is to divide the compressible

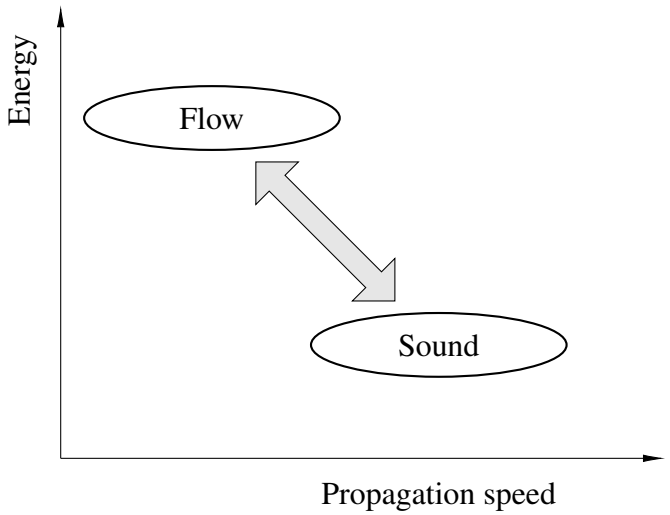

Figure 2.1: Description of the multi-scale problem based on [40].

flow field into an incompressible flow field and an acoustic field [29, 72]

$$u_i = u_i^{\mathrm{inc}} + u_i^{\mathrm{ac}}, \tag{2.10}$$
$$p_i = p_i^{\mathrm{inc}} + p_i^{\mathrm{ac}}, \tag{2.11}$$
$$\rho_i = \rho_i^{\mathrm{inc}} + \rho_i^{\mathrm{ac}}. \tag{2.12}$$

Linearized Euler Equation Subtracting the incompressible Navier-Stokes equations from the compressible Navier-Stokes equations and neglecting the high order terms leads to

$$\frac{\partial \rho^{\mathrm{ac}}}{\partial t} + \rho^{\mathrm{inc}} \frac{\partial u_i^{\mathrm{ac}}}{\partial x_i} + u_i^{\mathrm{inc}} \frac{\partial \rho^{\mathrm{ac}}}{\partial x_i} = 0, \tag{2.13}$$
$$\rho^{\mathrm{inc}} \frac{\partial u_i^{\mathrm{ac}}}{\partial t} + \rho^{\mathrm{inc}} u_j^{\mathrm{inc}} \frac{\partial u_i^{\mathrm{ac}}}{\partial x_j} + \frac{\partial p^{\mathrm{ac}}}{\partial x_i} = 0, \tag{2.14}$$

which are the governing equations for the acoustic density ρ^{ac} and the acoustic velocity u_i^{ac}. In order to close the equation system, a govering equation for the acoustic pressure p^{ac} is needed, which can be derived starting from the equation of state [72]

$$p = p\left(\rho, S\right), \tag{2.15}$$

with the entropy per unit mass S.

The time derivative of the pressure is given as

$$\frac{\partial p}{\partial t} = \left(\frac{\mathrm{d}p}{\mathrm{d}\rho}\right)_S \frac{\partial \rho}{\partial t} + \left(\frac{\mathrm{d}p}{\mathrm{d}S}\right)_\rho \frac{\partial S}{\partial t}, \tag{2.16}$$

which represents the pressure change due to the density change and the entropy change. It can be assumed that the pressure disturbation is an isentropic process, indicating that the second term in Eq. (2.16) is 0. Considering the speed of sound

$$c = \sqrt{\left(\frac{\partial p}{\partial \rho}\right)_S}, \tag{2.17}$$

(2.16) is transformed to

$$\frac{\partial p}{\partial t} = c^2 \frac{\partial \rho}{\partial t}. \tag{2.18}$$

The compressible density ρ and the compressible pressure p can be substituted by incompressible and acoustic variables, leading to

$$\frac{\partial p^{\mathrm{ac}}}{\partial t} + c^2 \rho^{\mathrm{inc}} \frac{\partial u_i^{\mathrm{ac}}}{\partial x_i} + c^2 u_i^{\mathrm{inc}} \frac{\partial \rho^{\mathrm{ac}}}{\partial x_i} = -\frac{\partial p^{\mathrm{inc}}}{\partial t}. \tag{2.19}$$

Finally, the linearized Euler equations are summarized as

$$\frac{\partial \rho^{\mathrm{ac}}}{\partial t} + \rho^{\mathrm{inc}} \frac{\partial u_i^{\mathrm{ac}}}{\partial x_i} + u_i^{\mathrm{inc}} \frac{\partial \rho^{\mathrm{ac}}}{\partial x_i} = 0, \tag{2.20}$$

$$\rho^{\mathrm{inc}} \frac{\partial u_i^{\mathrm{ac}}}{\partial t} + \rho^{\mathrm{inc}} u_j^{\mathrm{inc}} \frac{\partial u_i^{\mathrm{ac}}}{\partial x_j} + \frac{\partial p^{\mathrm{ac}}}{\partial x_i} = 0, \tag{2.21}$$

$$\frac{\partial p^{\mathrm{ac}}}{\partial t} + c^2 \rho^{\mathrm{inc}} \frac{\partial u_i^{\mathrm{ac}}}{\partial x_i} + c^2 u_i^{\mathrm{inc}} \frac{\partial \rho^{\mathrm{ac}}}{\partial x_i} = -\frac{\partial p^{\mathrm{inc}}}{\partial t}. \tag{2.22}$$

CHAPTER 3

NUMERICAL METHODS

The partial differential equations (PDE) governing the flow motion and the acoustic propagation cannot be solved analytically. Consequently, various numerical methods have been established to find approximate solutions. The finite difference method (FDM) [75], the finite element method (FEM) [96, 97, 98] and the finite volume method (FVM) [21, 70, 88] are the most successful numerical methods. The FVM ensures that the conservation laws are also fulfilled in the discrete equations. Therefore, the FVM is the most popular numerical method in the CFD field.

In this chapter, the numerical methods necessary to solve the governing equations for flow and acoustic problems addressed in the previous chapter are described. The FVM for flow problems is first discussed. Subsequently, the numerical methods used to solve the linearized Euler equations (LEE) are outlined.

3.1 Finite Volume Method

In the following, the FVM approach is illustrated based on the general transport equation

$$\frac{\partial}{\partial t}\left(\rho\phi\right) + \frac{\partial}{\partial x_j}\left(\rho u_j \phi\right) = \frac{\partial}{\partial x_j}\left(\Gamma_\phi \frac{\partial \phi}{\partial x_j}\right) + S_\phi, \tag{3.1}$$

with the scalar ϕ and the diffusion coefficient Γ_ϕ.

Generally, the FVM approach has five steps: First, the computational domain is discretized by control volumes (CV). Second, an integral equation based on the given PDE is formulated. Third, the integrals are approximated using numerical integrations. Fourth, the convective flux and diffusive flux are approximated. Finally, a discrete algebraic system is assembled and solved [70].

3.1.1 Spatial Discretization

The computational domain can be discretized using structured or unstructured grids. Structured grids provide higher computational efficiency and are therefore applied for the research in this thesis.

The transport equation (3.1) is integrated over a CV to form an integral equation

$$\int_V \frac{\partial}{\partial t}(\rho\phi)\ \mathrm{d}V + \sum_c \int_{S_c} \rho u_j \phi n_j\ \mathrm{d}S = \sum_c \int_{S_c} \Gamma_\phi \frac{\partial \phi}{\partial x_j} n_j\ \mathrm{d}S + \int_V S_\phi\ \mathrm{d}V, \quad (3.2)$$

where c represents the 6 surfaces of the current CV. Figure 3.1 shows the notations of CVs and surfaces for a Cartesian grid. In perspective of the cell P, the neighboring CVs are named as E, W, N, S, T and B, while the surfaces adjacent to the neighboring CVs are denoted using small letters e, w, n, s, t and b.

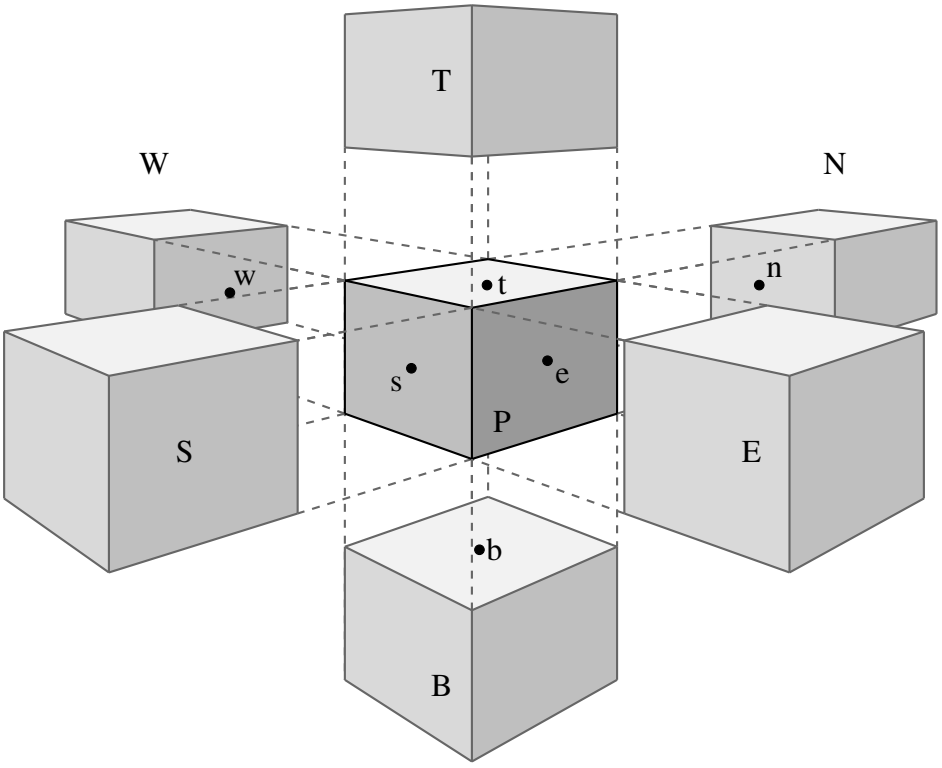

Figure 3.1: Description of the positions and notations of the adjacent CVs of the central CV.

3.1.2 Approximation of the Convective Flux

Applying the midpoint rule on the convective flux, we obtain

$$\sum_c \int_{S_c} \rho u_j \phi n_j \, \mathrm{d}S \approx \sum_c (\rho u_j \phi n_j)_c \delta S_c = \sum_c \dot{m}_c \phi_c. \tag{3.3}$$

The scalar value on the surface center ϕ_c needs to be formulated using values at the CV center. There are three methods to calculate the surface values: the central differencing scheme (CDS), the upwind differencing scheme (UDS) and the flux-blending method.

In the CDS scheme, the surface values are approximated by linear interpolation of values of the neighboring CVs

$$\phi_\mathrm{e} \approx \gamma_\mathrm{e} \phi_\mathrm{E} + (1 - \gamma_\mathrm{e}) \phi_\mathrm{P}, \tag{3.4}$$

where γ_e is the interpolation factor defined by

$$\gamma_\mathrm{e} = \frac{x_\mathrm{e} - x_\mathrm{P}}{x_\mathrm{E} - x_\mathrm{P}}, \tag{3.5}$$

In the UDS approach, ϕ_e is determined depending on the flow direction

$$\phi_\mathrm{e} = \begin{cases} \phi_\mathrm{P}, & \text{if} \quad \dot{m}_\mathrm{e} > 0 \\ \phi_\mathrm{E}, & \text{if} \quad \dot{m}_\mathrm{e} < 0 \end{cases} . \tag{3.6}$$

On Cartesian grids, the CDS scheme has a second order accuracy, whereas the UDS scheme is only first order accurate. However, the CDS scheme presents unphysical oscillations, while the UDS scheme has better robustness and boundedness. In order to stay bounded, the Pèclet number

$$Pe = \frac{\rho \phi \Delta x}{\Gamma_\phi}, \tag{3.7}$$

needs to satisfy the condition $Pe < 2$, where Δx is the grid spacing. However, this condition can only be satisfied in some extreme cases. The flux blending method combines the CDS scheme and the UDS scheme, given as

$$\phi_\mathrm{e} \approx \beta \phi_\mathrm{e}^\mathrm{CDS} + (1 - \beta) \phi_\mathrm{e}^\mathrm{UDS}, \tag{3.8}$$

where β is a coefficient chosen between 0 and 1. Due to the higher order accuracy of the CDS scheme, the preferred value of the β is 1. Only when the results present unphysical oscillations and a refinement of the grid is not possible, a value of $\beta < 1$ can be selected [70].

3.1.3 Approximation of the Diffusive Flux

The diffusive flux needs to be formulated using the values of the center of the CVs as well. Again, the diffusive flux on the east surface is taken as an example. One of the simplest methods to approximate the diffusive flux is the central differencing formula

$$\left(\frac{\partial \phi}{\partial x}\right)_{\mathrm{e}} \approx \frac{\phi_{\mathrm{E}} - \phi_{\mathrm{P}}}{x_{\mathrm{E}} - x_{\mathrm{P}}}, \tag{3.9}$$

which is based on the assumption that ϕ is linear between x_{E} and x_{P}. For equidistant grid, this scheme presents an error of second order, while for non-equidistant grids, the error increases to first order [70].

3.1.4 Approximation of Integrals

Due to the simplicity, the midpoint rule is used to approximate the volume integrals

$$\int_V S_\phi \, \mathrm{d}V = (S_\phi)_{\mathrm{P}} \delta V, \tag{3.10}$$

with the volume of the CV in question δV. The midpoint rule is second order accurate. Other common methods are the second order accurate trapezoidal rule and the fourth order accurate Simpson rule, which are, however, not applied in this work due to the complexity.

3.1.5 Time Discretization

For unsteady problems, the time derivative term in Eq. (3.1) must be approximated numerically, which can be realized using implicit methods or explicit methods. The following description is based on the general equation for time-dependent problems

$$\frac{\partial \phi(t)}{\partial t} = R(\phi), \tag{3.11}$$

where $R(\phi)$ represents the sum of the convective term, the diffusive term and the source term.

In the explicit methods, the time derivative is approximated using a forward difference formula, and the solution at t_{n+1} is therefore dependent only on solutions of previous time steps

$$\phi(t_{n+1}) = f(\phi(t_n), \phi(t_{n-1}), \cdots). \tag{3.12}$$

The advantages of the explicit methods are the faster update of each time step and the less required memory to save data.

On the contrary, the implicit methods utilize a backward difference formula. Consequently, the solution can be described by

$$\phi(t_{n+1}) = f(\phi(t_{n+1}), \phi(t_n), \cdots). \tag{3.13}$$

It is evident that the solution at t_{n+1} is dependent upon the solution of the current time step. As a result, the equation must be solved for each time step. The advantage of the implicit methods is the possibility to use larger time steps.

3.1.6 Assembly and Solution of the Equations

All terms in Eq. (3.1) can be formulated by the cell center values using the methods described in previous sections. At this point, the equation can be rewritten into

$$a_{\mathrm{P}}^{i}\phi_{\mathrm{P}}^{i} - \sum_{c} a_{\mathrm{c}}^{i}\phi_{\mathrm{c}}^{i} = b_{\mathrm{P}}^{i} \quad \text{for all} \quad i = 1, \ldots, N, \tag{3.14}$$

where N is the number of all CVs. Assembling the algebraic equations for each CVs together, one obtains a matrix equation

$$\boldsymbol{A}\boldsymbol{\phi} = \boldsymbol{b}, \tag{3.15}$$

with the unknown vector $\boldsymbol{\phi}$, the coefficient matrix $\boldsymbol{A}$ and the vector $\boldsymbol{b}$. The matrix equation can be solved using various methods. In this work, the strongly implicit procedure (SIP) method is applied, which is one of the incomplete LU decomposition methods.

For the incompressible Navier-Stokes equations, the assembled matrix equation can be represented as follows

$$\begin{bmatrix} \boldsymbol{A_{11}} & \boldsymbol{A_{12}} & \boldsymbol{A_{13}} \\ \boldsymbol{A_{21}} & \boldsymbol{A_{22}} & \boldsymbol{A_{31}} \\ \boldsymbol{A_{31}} & \boldsymbol{A_{32}} & 0 \end{bmatrix} \begin{bmatrix} \boldsymbol{u} \\ \boldsymbol{v} \\ \boldsymbol{p} \end{bmatrix} = \begin{bmatrix} \boldsymbol{b_1} \\ \boldsymbol{b_2} \\ 0 \end{bmatrix}, \tag{3.16}$$

where $\boldsymbol{A_{11}}, \ldots, \boldsymbol{A_{11}}$, $\boldsymbol{b_1}$ and $\boldsymbol{b_2}$ are the operators defined according to Eq. (3.14). As can been seen from Eq. (3.16), the pressure does not appear in the continuity equation, meaning that the pressure cannot be solved directly from the continuity equation. This issue causes one of the major problems of solving the incompressible Navier-Stokes equations, requiring special treatment to circumvent. In FASTEST, the pressure-correction method named Semi-Implicit Method for Pressure-Linked Equations (SIMPLE) is used. In general, the idea of the pressure-correction methods is that the velocities are first calculated by solving the momentum equations, then the velocities and the pressure are iteratively corrected such that the continuity equation and the momentum equations are both fulfilled. More detailed description about the FVM method for fluid dynamics can be found in e.g. [21, 70, 88].

3.2 FVM for the Linearized Euler Equations

In the following, the FVM used to solve the LEE is introduced. More details about this section can be found in [40]. The FVM for hyperbolic equations generally is given in [44] and [85].

The LEE can be formulated in flux form as follows

$$\frac{\partial \boldsymbol{U}}{\partial t} + \frac{\partial \boldsymbol{F}}{\partial x} + \frac{\partial \boldsymbol{G}}{\partial y} + \frac{\partial \boldsymbol{H}}{\partial z} = \boldsymbol{S}, \tag{3.17}$$

with the acoustic quantities

$$\boldsymbol{U} = (\rho^{\mathrm{ac}}, u^{\mathrm{ac}}, v^{\mathrm{ac}}, w^{\mathrm{ac}}, p^{\mathrm{ac}})^{\mathsf{T}}, \tag{3.18}$$

the fluxes

$$\boldsymbol{F} = \left(\rho^{\mathrm{inc}} u^{\mathrm{ac}},\ \frac{p^{\mathrm{ac}}}{\rho^{\mathrm{inc}}},\ 0,\ 0,\ \rho^{\mathrm{inc}} c^2 u^{\mathrm{ac}}\right)^{\mathsf{T}}, \tag{3.19}$$

$$\boldsymbol{G} = \left(\rho^{\mathrm{inc}} v^{\mathrm{ac}},\ 0,\ \frac{p^{\mathrm{ac}}}{\rho^{\mathrm{inc}}},\ 0,\ \rho^{\mathrm{inc}} \mathrm{c}^2 v^{\mathrm{ac}}\right)^{\mathsf{T}}, \tag{3.20}$$

$$\boldsymbol{H} = \left(\rho^{\mathrm{inc}} w^{\mathrm{ac}},\ 0,\ 0,\ \frac{p^{\mathrm{ac}}}{\rho^{\mathrm{inc}}},\ \rho^{\mathrm{inc}} \mathrm{c}^2 w^{\mathrm{ac}}\right)^{\mathsf{T}}, \tag{3.21}$$

and the source term

$$\boldsymbol{S} = \left(0,\ 0,\ 0,\ 0,\ -\frac{\partial p^{\mathrm{inc}}}{\partial t}\right)^{\mathsf{T}}. \tag{3.22}$$

3.2.1 One Dimensional Equations of the LEE

By using splitting techniques, the three dimensional LEE can be reduced to one dimensional problems

$$\frac{\partial \boldsymbol{u}}{\partial t} + \boldsymbol{A}\frac{\partial \boldsymbol{u}}{\partial x} = \boldsymbol{0}, \tag{3.23}$$

with the variable vector

$$\boldsymbol{u} = (u^{\mathrm{ac}},\ p^{\mathrm{ac}})^{\mathsf{T}}, \tag{3.24}$$

and the Jacobian matrix

$$\boldsymbol{A} = \begin{pmatrix} 0 & \dfrac{1}{\rho^{\mathrm{inc}}} \\ c^2 \rho^{\mathrm{inc}} & 0 \end{pmatrix}. \tag{3.25}$$

Figure 3.2 shows the discretization of the equation system in x and t directions.

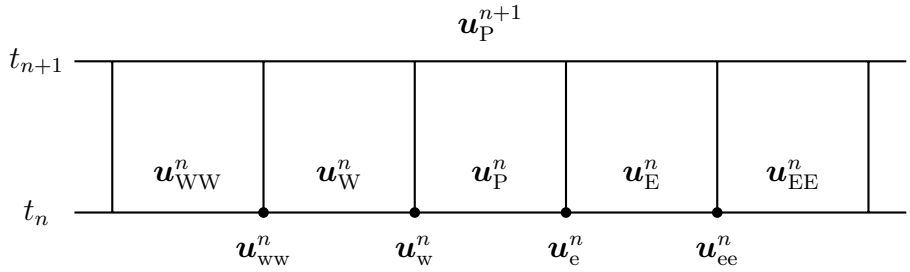

Figure 3.2: Discretization in the x and t directions for the FVM of the LEE.

The variable $\boldsymbol{u}$ can be updated by [44]

$$\boldsymbol{u}_{\mathrm{P}}^{n+1} = \boldsymbol{u}_{\mathrm{P}}^{n} - \frac{\Delta t}{\Delta x}\left(\boldsymbol{\mathcal{F}}_{\mathrm{e}}^{n} - \boldsymbol{\mathcal{F}}_{\mathrm{w}}^{n}\right), \tag{3.26}$$

with $\boldsymbol{\mathcal{F}}_{\mathrm{e}}^{n}$ and $\boldsymbol{\mathcal{F}}_{\mathrm{w}}^{n}$ being the numerical fluxes at the edge e and w, which are calculated by

$$\boldsymbol{\mathcal{F}}_{\mathrm{e}}^{n} = \frac{\boldsymbol{A}}{\Delta t}\int_{t_n}^{t_{n+1}} \boldsymbol{u}_{\mathrm{e}}\,\mathrm{d}t. \tag{3.27}$$

The numerical fluxes can be approximated using different numerical methods. In the upwind method, the numerical flux is obtained by

$$\boldsymbol{\mathcal{F}}_{\mathrm{e}}^{n} = \boldsymbol{A}^{+}\boldsymbol{u}_{\mathrm{P}} + \boldsymbol{A}^{-}\boldsymbol{u}_{\mathrm{E}}, \tag{3.28}$$

with

$$\begin{aligned}
&\boldsymbol{A}^{+} = \boldsymbol{K}\boldsymbol{\Lambda}^{+}\boldsymbol{K}^{-1}, \quad \boldsymbol{A}^{-} = \boldsymbol{K}\boldsymbol{\Lambda}^{-}\boldsymbol{K}^{-1},\\
&\boldsymbol{\Lambda}^{+} = \begin{pmatrix}\lambda_1^{+} & 0\\ 0 & \lambda_2^{+}\end{pmatrix}, \quad \boldsymbol{\Lambda}^{-} = \begin{pmatrix}\lambda_1^{-} & 0\\ 0 & \lambda_2^{-}\end{pmatrix},\\
&\lambda_1^{+} = \max\left(\lambda_1, 0\right), \quad \lambda_2^{+} = \max(\lambda_2, 0),\\
&\lambda_1^{-} = \min\left(\lambda_1, 0\right), \quad \lambda_2^{-} = \min(\lambda_2, 0),
\end{aligned} \tag{3.29}$$

where λ_1 and λ_2 are the eigenvalues of the matrix $\boldsymbol{A}$, $\boldsymbol{K}$ is a matrix composed of the two eigenvectors of the matrix $\boldsymbol{A}$

$$\boldsymbol{K} = [\boldsymbol{K}^{(1)}, \boldsymbol{K}^{(2)}]. \tag{3.30}$$

The variable vectors can be updated by

$$\boldsymbol{u}_{\mathrm{P}}^{n+1} = \boldsymbol{u}_{\mathrm{P}}^{n} - \frac{\Delta t}{\Delta x}\boldsymbol{A}^{+}\left(\boldsymbol{u}_{\mathrm{P}}^{n} - \boldsymbol{u}_{\mathrm{W}}^{n}\right) - \frac{\Delta t}{\Delta x}\boldsymbol{A}^{-}\left(\boldsymbol{u}_{\mathrm{E}}^{n} - \boldsymbol{u}_{\mathrm{P}}^{n}\right). \tag{3.31}$$

3.2.2 The Lax-Wendroff Method

The variable $\boldsymbol{u}^{n+1}$ can be approximated using Taylor series

$$\boldsymbol{u}^{n+1} \approx \boldsymbol{u}^n + \Delta t \frac{\partial \boldsymbol{u}^n}{\partial t} + \frac{1}{2}(\Delta t)^2 \frac{\partial^2 \boldsymbol{u}^n}{\partial t^2}. \tag{3.32}$$

The first and second time derivatives of the variable $\boldsymbol{u}^n$ fulfil the following relation

$$\frac{\partial \boldsymbol{u}^n}{\partial t} = -\boldsymbol{A}\frac{\partial \boldsymbol{u}^n}{\partial x} \tag{3.33}$$

$$\frac{\partial^2 \boldsymbol{u}^n}{\partial t^2} = -\boldsymbol{A}\frac{\partial^2 \boldsymbol{u}^n}{\partial t \partial x} = \boldsymbol{A}^2 \frac{\partial^2 \boldsymbol{u}^n}{\partial x^2}. \tag{3.34}$$

Inserting (3.33) and (3.34) into (3.32) yields

$$\boldsymbol{u}^{n+1} = \boldsymbol{u}^n - \Delta t \boldsymbol{A}\frac{\partial \boldsymbol{u}^n}{\partial x} + \frac{1}{2}(\Delta t)^2 \boldsymbol{A}^2 \frac{\partial^2 \boldsymbol{u}^n}{\partial x^2}. \tag{3.35}$$

Approximating the spatial derivatives using the central finite differences leads to the updating scheme of the Lax-Wendroff method [44]

$$\boldsymbol{u}_{\mathrm{P}}^{n+1} = \boldsymbol{u}_{\mathrm{P}}^n - \frac{\Delta t}{2\Delta x}\boldsymbol{A}\left(\boldsymbol{u}_{\mathrm{E}}^n - \boldsymbol{u}_{\mathrm{W}}^n\right) + \frac{1}{2}\left(\frac{\Delta t}{\Delta x}\right)^2 \boldsymbol{A}^2\left(\boldsymbol{u}_{\mathrm{W}}^n - 2\boldsymbol{u}_{\mathrm{P}}^n + \boldsymbol{u}_{\mathrm{E}}^n\right). \tag{3.36}$$

Consequently, the numerical flux of the Lax-Wendroff method is formulated by [44]

$$\boldsymbol{\mathcal{F}}_{\mathrm{e}}^n = \boldsymbol{A}^+ \boldsymbol{u}_{\mathrm{P}}^n + \boldsymbol{A}^- \boldsymbol{u}_{\mathrm{E}}^n + \frac{1}{2}|\boldsymbol{A}|\left(\boldsymbol{I} - \frac{\Delta t}{\Delta x}|\boldsymbol{A}|\right)\sum_{i=1}^{2}\delta_i \boldsymbol{K}^{(i)}, \tag{3.37}$$

with δ_i being the difference of the eigenvalues between two adjacent cells.

3.2.3 High-Resolution Methods

Compared to the first order accurate upwind method, the second order accurate Lax-Wendroff method delivers mostly more satisfactory results. However, the Lax-Wendroff method presents numerical oscillations near discontinuities. The idea of high-resolution methods is to combine the Lax-Wendroff method and the upwind method, and thereby obtain smooth solutions with high-order accuracy [44].

Observing Eq. (3.27) and Eq. (3.37), one determines that the numerical flux of the Lax-Wendroff method has one additional term compared to the upwind method. The high-resolution method limits this additional term appropriately, to switch between the upwind method and the Lax-Wendroff method.

The numerical flux of the high-resolution method is given by [44]

$$\boldsymbol{\mathcal{F}}_{\mathrm{e}}^{n}=\boldsymbol{A}^{+}\boldsymbol{u}_{\mathrm{P}}^{n}+\boldsymbol{A}^{-}\boldsymbol{u}_{\mathrm{E}}^{n}+\frac{1}{2}|\boldsymbol{A}|\left(\boldsymbol{I}-\frac{\Delta t}{\Delta x}|\boldsymbol{A}|\right)\sum_{i=1}^{2}\phi\left(\theta_{\mathrm{e},i}^{n}\right)\delta_{i}\boldsymbol{K}^{(i)}\quad, \tag{3.38}$$

with the flux-limiter ϕ, which is dependent on the smoothness indicator [44]

$$\theta_{e,i}^{n}=\begin{cases}\dfrac{(\delta_i)_{\mathrm{w}}}{(\delta_i)_{\mathrm{e}}} & \text{if } \lambda_i>0\\[2ex] \dfrac{(\delta_i)_{\mathrm{ee}}}{(\delta_i)_{\mathrm{e}}} & \text{if } \lambda_i<0\end{cases}. \tag{3.39}$$

When the flux limiter is set to $\phi_{\mathrm{e}}^{n}\left(\theta_{\mathrm{e},i}^{n}\right)=1$, the Lax-Wendroff method is applied. On the contrary, the upwind method is applied for $\phi_{\mathrm{e}}^{n}\left(\theta_{\mathrm{e},i}^{n}\right)=0$.

In the high-resolution method, the flux limiter is close to 1 when $\phi_{\mathrm{e}}^{n}\left(\theta_{\mathrm{e},i}^{n}\right)\approx 1$. When the smoothness indicator decreases, the flux limiter also decreases accordingly. The most common flux limiters are [44]

$$\text{MC:}\quad \phi(\theta)=\max(0,\min((1+\theta)/2,2,2\theta)), \tag{3.40}$$

$$\text{superbee:}\quad \phi(\theta)=\max(0,\min(1,2\theta),\min(2,\theta)), \tag{3.41}$$

$$\text{van Leer:}\quad \phi(\theta)=\frac{\theta+|\theta|}{1+|\theta|}. \tag{3.42}$$

3.2.4 FVM for the Source Term

The operations illustrated previously considers only the propagation process. In order to deal with the generation process of the acoustics, the source term must be solved appropriately. The general equation with a source term $\boldsymbol{S}$ is given as

$$\frac{\partial \boldsymbol{U}}{\partial t}=\boldsymbol{S}. \tag{3.43}$$

The variable $\boldsymbol{S}$ can be updated using an explicit method. It should be noted here that the time step $\Delta t_n^{\mathrm{CAA}}$ is usually much smaller than that of the CFD

$$\Delta t_n^{\mathrm{CFD}}=m\Delta t_n^{\mathrm{CAA}}. \tag{3.44}$$

The acoustic variable at time t_{n+1} can be updated by

$$\boldsymbol{U}^{n+1}=\boldsymbol{U}^{(n+1)*}+\Delta t_n^{\mathrm{CAA}}\boldsymbol{S}, \tag{3.45}$$

where $\boldsymbol{U}^{(n+1)*}$ is the variable at time t_{n+1} without considering the source term.

CHAPTER 4

TURBULENCE AND TURBULENCE MODELING

The aerodynamic noise generated in turbulent flows constitutes the main subject of research in this thesis. Hence, a deep understanding of the turbulence is a prerequisite for the subsequent investigations. In this chapter, a general description of turbulence is first presented. Then the well-established turbulence modeling approaches are outlined.

4.1 Turbulent Flow

Turbulent flow, which is characterized as three dimensional, transient, random and irregular in space and time, is ubiquitous in engineering applications. The behaviour of turbulent flow is dependent on the Reynolds number [61]

$$Re = \frac{UL}{\nu}, \tag{4.1}$$

with the characteristic velocity U, the characteristic length L and the kinematic viscosity of the fluid ν. The Reynolds number represents the ratio of inertial forces to viscous forces. When the Reynolds number exceeds a certain limit, such that the inertial forces has more influence than the viscous forces, the laminar flow becomes turbulent. In the following, the fundamental theory about turbulence is introduced. For a more detailed theory about turbulence, the reader is referred to [57], [47], [94] and [84].

Energy Cascade A turbulent flow consists of eddies with different sizes. The large eddies contain most of the kinetic energy, whereas the small eddies are responsible for the dissipation [63]. This phenomenon can be shown in Fig. 4.1, where the energy

spectrum function is plotted against the wave number of the eddies. Most of the turbulent kinetic energy is produced in the energy-containing range by the large eddies, which have approximately the size of the largest structure in the flow. In the inertial subrange, the kinetic energy is transfered from the large scales to the small scales. In the dissipation range, the kinetic energy in the small scale eddies are dissipated to heat.

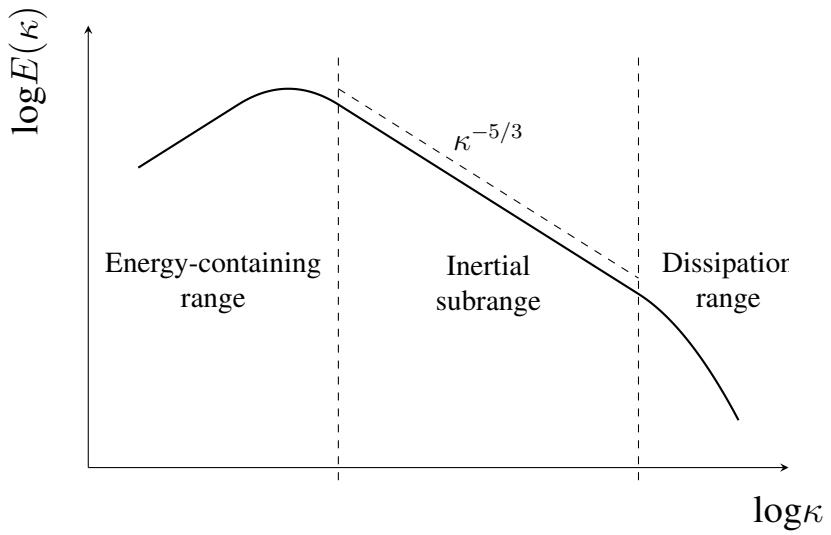

Figure 4.1: Schematic representation of turbulent energy cascade

More information about the energy cascade was revealed by the Kolmogorov hypotheses [37, 38]. According to the Kolmogorov hypotheses, the small scale turbulent motions are statistically isotropic. The smallest turbulent scales are denoted as Kolmogorov scales, including the length scale η, the velocity scale u_η and the time scale τ_η, given as

$$\eta = \left(\frac{\nu^3}{\varepsilon}\right)^{1/4}, \tag{4.2}$$

$$u_\eta = (\varepsilon\nu)^{1/4}, \tag{4.3}$$

$$\tau_\eta = \left(\frac{\nu}{\varepsilon}\right)^{1/2}, \tag{4.4}$$

with the viscosity ν and the energy dissipation rate ε. The relationships of the Kol-

mogorov scales to the largest scales are dependent on the Reynolds number

$$\frac{\eta}{l_0} \propto Re^{-3/4}, \tag{4.5}$$

$$\frac{u_\eta}{u_0} \propto Re^{-1/4}, \tag{4.6}$$

$$\frac{\tau_\eta}{\tau_0} \propto Re^{-1/2}. \tag{4.7}$$

In the inertial subrange, the relation between the the kinetic energy and the wave number can be determined as

$$E(\kappa) \propto \kappa^{-5/3}, \tag{4.8}$$

which is denoted as the Kolmogorov's 5/3 law. The concept of the energy cascade and the quantitative details are essential for the understanding and developing turbulence modeling techniques. More information about the energy cascade can be found in [57] and [53].

Law of the Wall Turbulent flows with the presence of solid structures is prevalent in engineering applications. The theory of the energy cascade discussed above does not consider the interaction with solid surfaces. Therefore, for a complete understanding of the turbulence, the flow near the wall needs to be studied additionally.

The fluid contacting with the solid wall fulfils the no-slip condition

$$u_\mathrm{w} = v_\mathrm{w} = w_\mathrm{w} = 0, \tag{4.9}$$

with u_w, v_w and w_w being the velocities at the wall. In the boundary layer, the turbulent flow is predominantly anisotropic. As the distance to the wall increases, the influence of the wall decreases and the turbulence becomes gradually isotropic. In order to describe the general characteristics of the boundary layer, non-dimensional distances and velocities are commonly used, which are given as

$$y^+ = \frac{y u_\tau}{\nu}, \quad u^+ = \frac{u}{u_\tau}, \tag{4.10}$$

with the friction velocity

$$u_\tau = \sqrt{\frac{\tau_\mathrm{w}}{\rho}} \quad \text{with} \quad \tau_\mathrm{w} = \mu \left(\frac{\partial u}{\partial y} \right)_\mathrm{w}, \tag{4.11}$$

where the subscript w indicates that the corresponding variable is at the wall, u is a velocity in tangential direction and y is the wall normal direction.

As shown in Fig. 4.2, the mean velocity profile in the boundary layer can be described using two functions depending on the distance to the wall. In the viscous sublayer

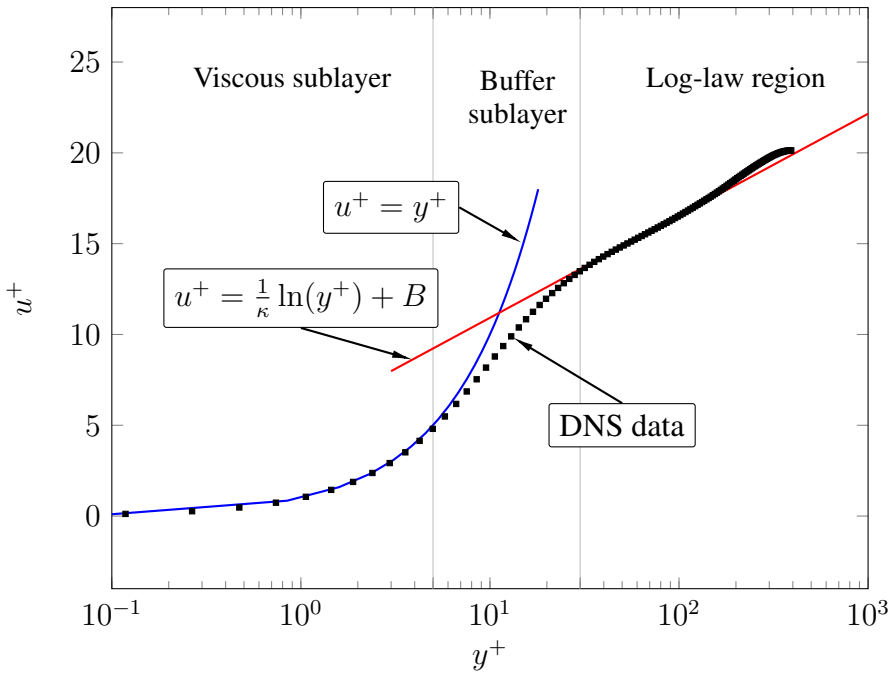

Figure 4.2: Illustration of the law of the wall based on the channel flow with $Re_\tau = 395$. The DNS data are extracted from [55].

($0 < y^+ < 5$), the non-dimensional velocity increases proportionally with the distance to the wall, which can be expressed as

$$u^+ = y^+. \tag{4.12}$$

In the sublayer $y^+ > 30$, the mean velocity fulfils the log law [36]

$$u^+ = \frac{1}{\kappa}\ln y^+ + B, \tag{4.13}$$

with a constant $B = 5.2$ and the von Kármán constant $\kappa = 0.41$.

In the buffer sublayer ($5 < y^+ < 30$), a transition between the linear relation and the log law can be observed.

More details about the boundary layer theory can be found in [71].

4.2 Direct Numerical Simulation

In the direct numerical simulation (DNS) approach, the Navier-Stokes equations are solved without any modelings. All the length scales, from the largest scale down to the Kolmogorov length scale, are resolved. Consequently, the grid size must be

so small that the Kolmogorov length scale can be resolved. In a foreseeable future, the DNS approach cannot be used for engineering problems. Nevertheless, the DNS approach is an important tool to gain insight in the turbulence physics and presents strong advantages compared to the experimental methods [54].

4.3 Reynolds-Averaged Navier-Stokes Modeling

The Reynolds-averaged Navier-Stokes (RANS) modeling delivers the averaged information of the flow field, which is usually sufficient for engineering applications, since in many cases we exclusively concern about the statistical behaviour of the flow. In order to obtain the averaged information, the field variables of the turbulent flow is first divided using the Reynolds decomposition

$$\phi(x_i,t) = \overline{\phi(x_i,t)} + \phi'(x_i,t), \tag{4.14}$$

where $\overline{\phi(x_i,t)}$ is the ensemble or time averaged part and $\phi'(x_i,t)$ is the fluctuation component. In this work, the decomposition of the incompressible velocity is expressed by

$$u_i^{\mathrm{inc}} = \overline{u_i^{\mathrm{inc}}} + u_i', \tag{4.15}$$

Applying the Reynolds decomposition to the Navier-Stokes equations leads to the Reynolds Averaged Navier-Stokes equations

$$\frac{\partial \overline{u_i^{\mathrm{inc}}}}{\partial x_i} = 0, \tag{4.16}$$

$$\frac{\partial \rho^{\mathrm{inc}} \overline{u_i^{\mathrm{inc}}}}{\partial t} + \rho^{\mathrm{inc}} \frac{\partial \overline{u_i^{\mathrm{inc}}}\,\overline{u_j^{\mathrm{inc}}}}{\partial x_j} = \frac{\partial}{\partial x_j}\left[\mu\left(\frac{\partial \overline{u_i^{\mathrm{inc}}}}{\partial x_j} + \frac{\partial \overline{u_j^{\mathrm{inc}}}}{\partial x_i}\right)\right] - \frac{\partial(\rho^{\mathrm{inc}}\overline{u_i'u_j'})}{\partial x_j} - \frac{\partial \overline{p^{\mathrm{inc}}}}{\partial x_i}. \tag{4.17}$$

The RANS equations, however, cannot be solved without further information, since an additional unknown term $-\rho^{\mathrm{inc}}\overline{u_i'u_j'}$, often called Reynolds stress tensor and denoted as τ_{ij}, arises from the non-linear convective term, making the equation system underdetermined. The Reynolds stress tensor, describing the influence of the fluctuation term on the averaged part, can be obtained using two different approaches. The first one, called Reynolds stress equation model (RSM), computes the Reynolds stress tensor by directly solving six additional equations. The RSM approach offers satisfactory results when dealing with flows with anisotropy, separation or recirculation. However, solving the additional equations increases the computational cost significantly, which hinders it from broader application. The other approach is referred to as eddy viscosity models, where the Reynolds stress tensor is obtained using Boussinesq approximation [9]

$$\tau_{ij} = -\rho^{\mathrm{inc}}\overline{u_i'u_j'} = \mu_{\mathrm{t}}\left(2S_{ij} - \frac{2}{3}\frac{\partial u_k^{\mathrm{inc}}}{\partial x_k}\delta_{ij}\right) - \frac{2}{3}\rho^{\mathrm{inc}}k\delta_{ij}, \tag{4.18}$$

with the dynamic turbulent viscosity μ_t, the turbulent kinetic energy k and the strain rate tensor S_{ij}

$$k = \frac{1}{2}\overline{u_i' u_i'}, \tag{4.19}$$

$$S_{ij} = \frac{1}{2}\left(\frac{\partial \overline{u_i^{\mathrm{inc}}}}{\partial x_j} + \frac{\partial \overline{u_j^{\mathrm{inc}}}}{\partial x_i}\right). \tag{4.20}$$

The dynamic turbulent viscosity μ_t is a scalar, indicating that the turbulence is assumed isotropic, which could cause inaccurate results in anisotropic turbulent flows. Nevertheless, due to the lower computational cost and acceptable accuracy of results, the eddy viscosity models are still widely applied for engineering problems. In order to determine the dynamic turbulent viscosity μ_t, many different turbulence models have been developed. The most simple models are the mixing length model proposed by Prandtl [58] and the Spalart-Allmaras model [77]. The two-equation models utilize two additional equations to reproduce the turbulent viscosity, yielding mostly very successful results. In the following, the two-equation models relevant for this work are introduced.

4.3.1 $k-\varepsilon$ model

One of the most widely applied RANS models is the $k-\varepsilon$ model, which is simple and provides mostly satisfactory results. The governing equations are given as [34]

$$\frac{\partial \rho^{\mathrm{inc}} k}{\partial t} + \rho^{\mathrm{inc}} \overline{u_j^{\mathrm{inc}}} \frac{\partial k}{\partial x_j} = P_k + \frac{\partial}{\partial x_j}\left[\left(\mu + \frac{\mu_\mathrm{t}}{\sigma_k}\right)\frac{\partial k}{\partial x_j}\right] - \rho^{\mathrm{inc}}\varepsilon, \tag{4.21}$$

$$\frac{\partial \rho^{\mathrm{inc}} \varepsilon}{\partial t} + \rho^{\mathrm{inc}} \overline{u_j^{\mathrm{inc}}} \frac{\partial \varepsilon}{\partial x_j} = C_{\varepsilon 1}\frac{\varepsilon}{k}P_k - C_{\varepsilon 2}\rho^{\mathrm{inc}}\frac{\varepsilon^2}{k} + \frac{\partial}{\partial x_j}\left[\left(\mu + \frac{\mu_\mathrm{t}}{\sigma_\varepsilon}\right)\frac{\partial \varepsilon}{\partial x_j}\right], \tag{4.22}$$

where

$$P_k = \tau_{ij}\frac{\partial u_i^{\mathrm{inc}}}{\partial x_j}. \tag{4.23}$$

The dynamic turbulent viscosity is then calculated from

$$\mu_\mathrm{t} = C_\mu \rho^{\mathrm{inc}} \frac{k^2}{\varepsilon}. \tag{4.24}$$

The constants and coefficients used for this model are given as

$$\sigma_k = 1.0, \quad \sigma_\varepsilon = 1.3, \quad C_\mu = 0.09, \quad C_{\varepsilon 1} = 1.44, \quad C_{\varepsilon 2} = 1.92. \tag{4.25}$$

4.3.2 $k-\omega$ model

Another popular two-equation model is the $k-\omega$ model [93]

$$\rho^{\mathrm{inc}}\frac{\partial k}{\partial t}+\rho^{\mathrm{inc}}\overline{u_j^{\mathrm{inc}}}\frac{\partial k}{\partial x_j}=P_k-\rho^{\mathrm{inc}}\beta^* k\omega+\frac{\partial}{\partial x_j}\left[\left(\mu+\sigma_k\mu_{\mathrm{t}}\right)\frac{\partial k}{\partial x_j}\right], \tag{4.26}$$

$$\rho^{\mathrm{inc}}\frac{\partial \omega}{\partial t}+\rho^{\mathrm{inc}}\overline{u_j^{\mathrm{inc}}}\frac{\partial \omega}{\partial x_j}=\frac{\gamma}{\nu_{\mathrm{t}}}P_k-\rho^{\mathrm{inc}}\beta\omega^2+\frac{\partial}{\partial x_j}\left[\left(\mu+\sigma_\omega\mu_{\mathrm{t}}\right)\frac{\partial \omega}{\partial x_j}\right], \tag{4.27}$$

which uses a constructed variable ω to build the second equation. The relation between the variables ω and ε is given as

$$\varepsilon=\beta^*\omega k. \tag{4.28}$$

The dynamic turbulent viscosity is calculated using

$$\mu_{\mathrm{t}}=\rho^{\mathrm{inc}}\frac{k}{\omega}. \tag{4.29}$$

The model constants are given as

$$\sigma_k=\sigma_\omega=0.5,\quad \beta^*=0.09,\quad \beta=0.075,\quad \gamma=5/9. \tag{4.30}$$

4.3.3 SST $k-\omega$ model

The SST $k-\omega$ model, proposed by Menter [48, 49], combines the $k-\varepsilon$ model and the $k-\omega$ model. In the boundary layer, the $k-\omega$ is used, allowing the model to be applied down to the wall without additional damping functions. The use of the $k-\varepsilon$ model in the region far from the wall avoids the pressure gradient problems for the $k-\omega$ model.

The governing equations of the SST $k-\omega$ model are given as

$$\rho^{\mathrm{inc}}\frac{\partial k}{\partial t}+\rho^{\mathrm{inc}}\overline{u_j^{\mathrm{inc}}}\frac{\partial k}{\partial x_j}=P_k-\rho^{\mathrm{inc}}\beta^* k\omega+\frac{\partial}{\partial x_j}\left[\left(\mu+\sigma_k\mu_{\mathrm{t}}\right)\frac{\partial k}{\partial x_j}\right], \tag{4.31}$$

$$\begin{aligned}\rho^{\mathrm{inc}}\frac{\partial \omega}{\partial t}+\rho^{\mathrm{inc}}\overline{u_j^{\mathrm{inc}}}\frac{\partial \omega}{\partial x_j}&=\frac{\gamma}{\nu_{\mathrm{t}}}P_k-\rho^{\mathrm{inc}}\beta\omega^2+\frac{\partial}{\partial x_j}\left[\left(\mu+\sigma_\omega\mu_{\mathrm{t}}\right)\frac{\partial \omega}{\partial x_j}\right]\\&\quad+2(1-F_1)\rho^{\mathrm{inc}}\frac{\sigma_{\omega 2}}{\omega}\frac{\partial k}{\partial x_j}\frac{\partial \omega}{\partial x_j}.\end{aligned} \tag{4.32}$$

The dynamic turbulent viscosity is computed by

$$\mu_{\mathrm{t}}=\frac{a_1 k\rho^{\mathrm{inc}}}{\max(a_1\omega,\Omega F_2)}, \tag{4.33}$$

where $a_1=0.31$ and Ω is the vorticity magnitude

$$\Omega=\sqrt{2\Omega_{ij}\Omega_{ij}},\quad \text{with}\quad \Omega_{ij}=\frac{1}{2}\left(\frac{\partial u_i^{\mathrm{inc}}}{\partial x_j}-\frac{\partial u_j^{\mathrm{inc}}}{\partial x_i}\right). \tag{4.34}$$

F_1 and F_2 are blending functions with a value of 1 at the wall and a value of 0 for the positions far enough from the wall.

Table 4.1: Model constants for the SST $k-\omega$ model.

ϕ	ϕ_1	ϕ_2
σ_k	σ_{k1}=0.85	σ_{k2}=1.0
σ_ω	$\sigma_{\omega1}$=0.5	$\sigma_{\omega2}$=0.856
β	β_1=0.075	β_2=0.0828
γ	$\gamma_1 = \frac{\beta_1}{\beta^*} - \frac{\sigma_{\omega1}\kappa^2}{\sqrt{\beta^*}}$	$\gamma_2 = \frac{\beta_2}{\beta^*} - \frac{\sigma_{\omega2}\kappa^2}{\sqrt{\beta^*}}$

The model constants in Eq. (4.31) and Eq. (4.32) are calculated with the help of the blending function F_1

$$\phi = F_1\phi_1 + (1 - F_1)\phi_2, \tag{4.35}$$

where ϕ, ϕ_1 and ϕ_2 represent the model constants in the SST $k-\omega$ model and the corresponding constants in the $k-\varepsilon$ model and the $k-\omega$ model, which are listed in Table 4.1.

By combining the $k-\varepsilon$ and the $k-\omega$ models, the SST $k-\omega$ model is able to deliver accurate simulation results for various kinds of flows including flows with pressure-induced separation [51]. Consequently, the SST $k-\omega$ model has become a standard RANS model in many CFD softwares.

4.4 Large-Eddy Simulation

The basic idea of the large-eddy simulation (LES) is illustrated in Fig. 4.3. The large scale turbulent structures, containing most turbulent energy and are usually anisotropic, are resolved, while the small scale structures, which can be assumed isotropic, are modeled. By observing the energy cascade, it is clear that most turbulent energy is resolved while the sub-grid scales accounts for only a small fraction of the energy. This section gives a brief introduction of the LES model. More details can be found in [67] and [57].

The general filtering operation, first introduced by Leonard [43], is given as

$$\widetilde{\phi}(x_i, t) = \int_V G(r_i, x_i)\phi(x_i - r_i, t)\mathrm{d}r, \tag{4.36}$$

with $G(r_i, x_i)$ being a filter function, which satisfies the normalization condition

$$\int_V G(r_i, x_i)\mathrm{d}r = 1. \tag{4.37}$$

Similar to the Reynolds decomposition, an arbitrary quantity can be divided into a resolved part and a modeled part

$$\phi(x_i, t) = \widetilde{\phi}(x_i, t) + \phi'(x_i, t). \tag{4.38}$$

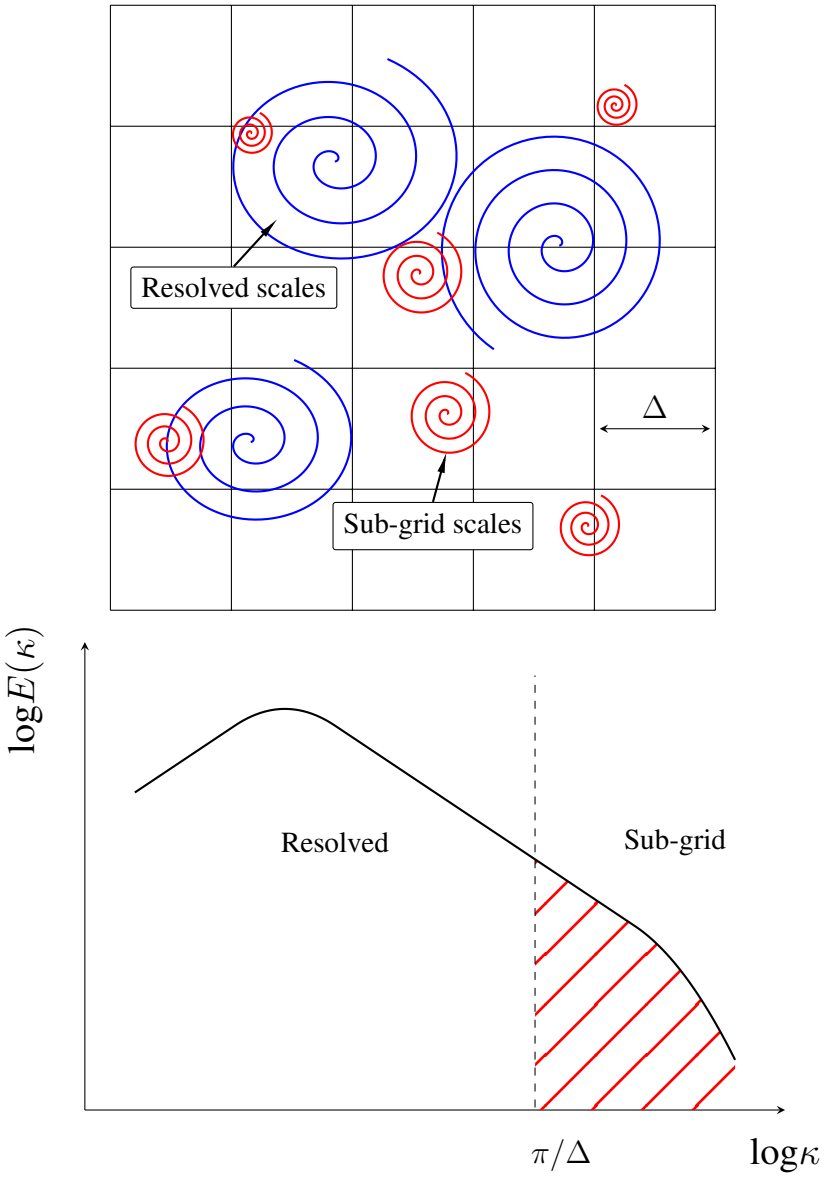

Figure 4.3: Filter operation based on [67]

Filtering the Navier-Stokes equations leads to the filtered Navier-Stokes equations

$$\frac{\partial \widetilde{u_i^{\mathrm{inc}}}}{\partial x_i} = 0, \tag{4.39}$$

$$\frac{\partial \widetilde{u_i^{\mathrm{inc}}}}{\partial t} + \frac{\partial \widetilde{u_i^{\mathrm{inc}}}\,\widetilde{u_j^{\mathrm{inc}}}}{\partial x_j} = \frac{\partial}{\partial x_j}\left[\nu\left(\frac{\partial \widetilde{u_i^{\mathrm{inc}}}}{\partial x_j} + \frac{\partial \widetilde{u_j^{\mathrm{inc}}}}{\partial x_i}\right)\right] - \frac{\partial \tau_{ij}^{\mathrm{sgs}}}{\partial x_j} - \frac{1}{\rho^{\mathrm{inc}}}\frac{\partial \widetilde{p^{\mathrm{inc}}}}{\partial x_i}, \tag{4.40}$$

with the sub-grid scale stress(SGS) τ_{ij}^{sgs}, defined by

$$\tau_{ij}^{\mathrm{sgs}} = \widetilde{u_i^{\mathrm{inc}} u_j^{\mathrm{inc}}} - \widetilde{u_i^{\mathrm{inc}}}\,\widetilde{u_j^{\mathrm{inc}}}. \tag{4.41}$$

The sub-grid term τ_{ij}^{sgs} can be decomposed into an anisotropic residual-stress tensor τ_{ij}^{r} and an isotropic residual stress

$$\tau_{ij}^{\mathrm{sgs}} = \tau_{ij}^{\mathrm{r}} + \frac{2}{3}k_{\mathrm{r}}\delta_{ij}, \tag{4.42}$$

with

$$k_{\mathrm{r}} = \frac{1}{2}\tau_{kk}^{\mathrm{sgs}}. \tag{4.43}$$

The isotropic residual stress can be added to the pressure term in Eq. (4.40).

$$\widetilde{P^{\mathrm{inc}}} = \widetilde{p^{\mathrm{inc}}} + \frac{2}{3}k_{\mathrm{r}}. \tag{4.44}$$

The sub-grid term τ_{ij}^{r} is unknown, causing a closure problem similar to the scenario of the RANS models. In this work, the sub-grid term is approximated based on the Smagorinsky model [74], where the sub-grid term is given as

$$\tau_{ij}^{\mathrm{r}} = -2\nu_{\mathrm{t}}\widetilde{S_{ij}} \quad \text{with} \quad \widetilde{S_{ij}} = \frac{1}{2}\left(\frac{\partial \widetilde{u_i^{\mathrm{inc}}}}{\partial x_j} + \frac{\partial \widetilde{u_j^{\mathrm{inc}}}}{\partial x_i}\right), \tag{4.45}$$

where ν_{t} is the turbulent viscosity, modeled by

$$\nu_{\mathrm{t}} = (C_{\mathrm{s}}\Delta)^2|\widetilde{S}|, \tag{4.46}$$

with the Smagorinsky constant $C_{\mathrm{s}} = 0.1$, the magnitude of the strain rate tensor $|\widetilde{S}|$

$$|\widetilde{S}| = \sqrt{2\widetilde{S_{ij}}\widetilde{S_{ij}}}. \tag{4.47}$$

The filter width Δ is obtained by [17]

$$\Delta = \sqrt[3]{\Delta_x \Delta_y \Delta_z}, \tag{4.48}$$

where Δ_x, Δ_y and Δ_z are the spacing sizes in x-, y- and z-direction.

4.5 Hybrid LES/RANS Methods

The RANS models are computationally advantageous, however, they are not able to capture the transient small scale structures, which contribute a considerable part to the noise generation. The LES model improves the computational results significantly by resolving the large scale motions and modeling the small scale structures. However, the LES model is almost only used in academic research due to the high computational cost. Consequently, hybrid LES/RANS models combining the advantages of the LES model and the RANS model have gained increasingly more interest. The hybrid LES/RANS methods can be classified into zonal and non-zonal models. The zonal models define the LES region and the RANS region a priori, while the non-zonal models uses one global turbulence model to switch between an LES region and a RANS region. The non-zonal models provide smooth velocities and eddy viscosities between the RANS and LES regions [52]. In the following, two existing non-zonal hybrid LES/RANS models in the in-house solver FASTEST are introduced, which are the detached-eddy simulation (DES) model and the very large eddy simulation (VLES) model, respectively. Other popular hybrid LES/RANS models include the limited numerical scales (LNS) model [3], the scale-adaptive simulation (SAS) model [50] and the partially averaged Navier-Stokes equation (PANS) model [27]. A detailed review about hybrid LES/RANS method is given by Fröhlich [25].

4.5.1 Detached Eddy Simulation

Due to the simple expression and the extensibility to a wide range of existing RANS models, the DES model proposed by Spalart in 1997 [76, 79] has become one of the most popular hybrid LES/RANS models. The DES model modifies RANS models to achieve an LES content, enabling the DES model to switch between RANS and LES according to the numerical resolution. This model is designed to function as a RANS model in boundary layers and free shear layers and as an LES model in the remaining regions. The idea behind such a distribution is that the RANS models are robust and less expensive in the near wall regions, while the LES model can provide accurate prediction in other areas. The switching between these two modes is realized by means of a length scale

$$l_{\mathrm{DES}} = \min(l_{\mathrm{RANS}}, C_{\mathrm{DES}}\Delta\psi), \tag{4.49}$$

where l_{RANS} is a integral turbulence length scale, Δ is the filter width, C_{DES} is a model constant, which is calibrated to 0.2 in [60] and [87] based on $k-\varepsilon-\zeta-f$ model, and ψ is a correction function.

For $k-\varepsilon$ based models, the integral turbulence length scale is given as

$$l_{\mathrm{RANS}} = \frac{k^{3/2}}{\varepsilon}. \tag{4.50}$$

The k equation is then rewritten as

$$\rho^{\mathrm{inc}}\frac{\partial k}{\partial t}+\rho^{\mathrm{inc}}\overline{u_j^{\mathrm{inc}}}\frac{\partial k}{\partial x_j}=P_k+\frac{\partial}{\partial x_j}\left[\left(\mu+\frac{\mu_{\mathrm{t}}}{\sigma_k}\right)\frac{\partial k}{\partial x_j}\right]-\rho^{\mathrm{inc}}\frac{k^{3/2}}{l_{\mathrm{DES}}}. \tag{4.51}$$

The original DES model delivers incorrect results when the grid spacing in the boundary layer is fine enough for the DES model to switch to LES mode, leading to a reduced turbulent viscosity. This problem is overcome by the delayed detached eddy simulation (DDES) model, in which the length scale is defined as [78]

$$l_{\mathrm{DDES}}=l_{\mathrm{RANS}}-f_{\mathrm{d}}\max(0,l_{\mathrm{RANS}}-C_{\mathrm{DES}}\Delta\psi), \tag{4.52}$$

where

$$f_{\mathrm{d}}=1-\tanh\left((8r_{\mathrm{d}})^3\right), \tag{4.53}$$

with

$$r_{\mathrm{d}}=\frac{\nu_{\mathrm{t}}+\nu}{\kappa^2 d_{\mathrm{w}}^2\max\left(10^{-10},\sqrt{\frac{\partial u_i^{\mathrm{inc}}}{\partial x_j}\frac{\partial u_i^{\mathrm{inc}}}{\partial x_j}}\right)}. \tag{4.54}$$

4.5.2 Very Large Eddy Model

Very large eddy simulation (VLES), also called flow simulation methodology in some literatures, was first proposed by Speziale [80]. The original idea was to damp the Reynolds stress tensor $\overline{u_i'u_j'}^{(\mathrm{RANS})}$ in Eq. (4.17) obtained from conventional RANS models via

$$\overline{u_i'u_j'}=\alpha\overline{u_i'u_j'}^{(\mathrm{RANS})}, \tag{4.55}$$

with α being a coefficient, defined as

$$\alpha=[1-\exp(-\beta L^{\Delta}/L^k)]^n, \tag{4.56}$$

where L^{Δ} denotes the filter width correlated with the computational mesh size and L^k is the Kolmogorov length scale. As L^{Δ}/L^k approaches 0 the Reynolds stress tensor vanishes, leading to a direct numerical simulation for the turbulent flow. On the contrary, if L^{Δ}/L^k approaches ∞ we have a regular RANS model. However, the original model has some shortcomings. First of all, the parameters β and n in Eq. (4.56) were not quantitatively defined. Furthermore, it is not necessary to set the Kolmogorov length scale as the limit to ensure an LES behaviour between the limits [90]. In addition, the original VLES model tends to over-damp the Reynolds stress tensor in the near wall region [39]. Therefore, different formulations of the damping coefficient have been proposed. In this paper, we apply the modification proposed by Chang et al. [14], where α is derived based on the concept

$$\alpha\propto\int_{\kappa_{\mathrm{C}}(\mathrm{LES})}^{\kappa_{\mathrm{K}}}E(\kappa)\,\mathrm{d}\kappa\Big/\int_{\kappa_{\mathrm{C}}(\mathrm{VLES})}^{\kappa_{\mathrm{K}}}E(\kappa)\,\mathrm{d}\kappa \tag{4.57}$$

where κ_{K} is the wave number of the Kolmogorov scale, and $\kappa_{\mathrm{C}}(\mathrm{LES})$ and $\kappa_{\mathrm{C}}(\mathrm{VLES})$ are the cut-off wave numbers of the VLES model and the LES model, respectively. Based on this assumption, α is formulated as

$$\alpha = \min\left[\left(\frac{L^{\Delta}}{k^{3/2}/\varepsilon}\right)^{\frac{4}{3}}, 1\right]. \tag{4.58}$$

CHAPTER 5

EXTENSION OF HYBRID TURBULENCE MODELING APPROACHES

In the frame of this work, the turbulence modeling approaches in the in-house solver FASTEST have been extended by a new hybrid LES/RANS model, the limited numerical scales (LNS) model. The governing equations of the LNS model based on the Chien $k-\varepsilon$ model and the $\zeta-f$ model are first given. Afterwards, the new implemented LNS model is validated using a benchmark test case.

5.1 Limited Numerical Scales

The LNS model, proposed by Batten et al. [3], is based on the same idea as the very large eddy simulation (VLES) model. The function α, named as latency factor by Batten, has the following form [25]

$$\alpha = \frac{\min(\nu_{\mathrm{t}}^{\mathrm{LES}}, \nu_{\mathrm{t}}^{\mathrm{RANS}})}{\nu_{\mathrm{t}}^{\mathrm{RANS}}}, \tag{5.1}$$

where $\nu_{\mathrm{t}}^{\mathrm{RANS}}$ is the turbulent viscosity obtained by an underlying RANS model, and $\nu_{\mathrm{t}}^{\mathrm{LES}}$ is the turbulent viscosity of an LES model. In the present work, we select the Smagorinsky model as the LES model

$$\nu_{\mathrm{t}}^{\mathrm{LES}} = (C_{\mathrm{s}}\Delta)^2|\widetilde{S}|. \tag{5.2}$$

When the grid is sufficiently fine, the LES branch $\nu_{\mathrm{t}}^{\mathrm{LES}}$ is chosen and the turbulent viscosity is scaled down to LES-like values. On the contrary, when the grid is coarse,

the RANS branch $\nu_{\mathrm{t}}^{\mathrm{RANS}}$ is applied and the turbulent viscosity is modeled using the underlying RANS model. In the following, the governing equations for the LNS models used in this work are presented.

Chien $k-\varepsilon$ based LNS Model The original $k-\varepsilon$ model demonstrates inadequate simulation results in the vicinity of the wall. Chien improved this model by considering the wall effect in the equation, making this model applicable for the low-Re areas. The Chien $k-\varepsilon$ equations are given as [15]

$$\rho^{\mathrm{inc}}\frac{\partial k}{\partial t}+\rho^{\mathrm{inc}}\overline{u_j^{\mathrm{inc}}}\frac{\partial k}{\partial x_j}=P_k+\frac{\partial}{\partial x_j}\left[\left(\mu+\frac{\mu_{\mathrm{t}}}{\sigma_k}\right)\frac{\partial k}{\partial x_j}\right]-\rho^{\mathrm{inc}}\varepsilon+\rho^{\mathrm{inc}}L_k, \tag{5.3}$$

$$\rho^{\mathrm{inc}}\frac{\partial \varepsilon}{\partial t}+\rho^{\mathrm{inc}}\overline{u_j^{\mathrm{inc}}}\frac{\partial \varepsilon}{\partial x_j}=C_{\varepsilon 1}f_1P_k-C_{\varepsilon 2}f_2\frac{\rho^{\mathrm{inc}}\varepsilon^2}{k}+\frac{\partial}{\partial x_j}\left[\left(\mu+\frac{\mu_{\mathrm{t}}}{\sigma_\varepsilon}\right)\frac{\partial \varepsilon}{\partial x_j}\right]+\rho^{\mathrm{inc}}L_\varepsilon. \tag{5.4}$$

The constants and coefficients used for this model are given as

$$\sigma_k=1.0,\quad \sigma_\varepsilon=1.3,\quad C_\mu=0.09,\quad C_{\varepsilon 1}=1.35,\quad C_{\varepsilon 2}=1.80, \tag{5.5}$$

$$f_1=1,\quad f_2=1-\frac{0.4}{1.8}e^{-Re_T^2/36},\quad Re_T=\frac{\rho k^2}{\mu\varepsilon},\quad f_\mu=1-e^{-0.0115d^+}, \tag{5.6}$$

where d^+ is a non-local function dependent on the minimum distance to the wall

$$d^+=d\rho u_\tau/\mu. \tag{5.7}$$

The two unknown terms L_k and L_ε in Eq. (5.3) and Eq. (5.4) are given as

$$L_k=-2\frac{\mu k}{\rho^{\mathrm{inc}}d^2}, \tag{5.8}$$

$$L_\varepsilon=-2\frac{\mu\varepsilon}{\rho^{\mathrm{inc}}d^2}e^{-d^+/2}. \tag{5.9}$$

For the LNS model, the dynamic turbulent viscosity is then calculated from

$$\mu_{\mathrm{t}}=\alpha\rho^{\mathrm{inc}}C_\mu f_\mu\frac{k^2}{\varepsilon}, \tag{5.10}$$

where α is defined as

$$\alpha=\min\left\{\frac{(C_{\mathrm{s}}\Delta)^2\sqrt{S_{ij}S_{ij}/2}}{C_\mu k^2/\varepsilon},1\right\}. \tag{5.11}$$

$\zeta - f$ based LNS model The $\zeta - f$ model, developed by Hanjalić et al. [28], is a four-equations model, given as

$$\rho^{\mathrm{inc}}\frac{\partial k}{\partial t} + \rho^{\mathrm{inc}}\overline{u_j^{\mathrm{inc}}}\frac{\partial k}{\partial x_j} = P_k + \frac{\partial}{\partial x_j}\left[\left(\mu + \frac{\mu_{\mathrm{t}}}{\sigma_k}\right)\frac{\partial k}{\partial x_j}\right] - \rho^{\mathrm{inc}}\varepsilon, \tag{5.12}$$

$$\rho^{\mathrm{inc}}\frac{\partial \varepsilon}{\partial t} + \rho^{\mathrm{inc}}\overline{u_j^{\mathrm{inc}}}\frac{\partial \varepsilon}{\partial x_j} = \frac{C_{\varepsilon 1}P_k - C_{\varepsilon 2}\rho^{\mathrm{inc}}\varepsilon}{\tau} + \frac{\partial}{\partial x_j}\left[\left(\mu + \frac{\mu_{\mathrm{t}}}{\sigma_k}\right)\frac{\partial \varepsilon}{\partial x_j}\right], \tag{5.13}$$

$$\frac{\partial \rho^{\mathrm{inc}}\zeta}{\partial t} + \rho^{\mathrm{inc}}\overline{u_j^{\mathrm{inc}}}\frac{\partial \zeta}{\partial x_j} = \rho^{\mathrm{inc}} f - \frac{\zeta}{k}P_k + \frac{\partial}{\partial x_j}\left[\left(\mu + \frac{\mu_{\mathrm{t}}}{\sigma_k}\right)\frac{\partial \zeta}{\partial x_j}\right], \tag{5.14}$$

$$L^2\nabla f - f = \frac{1}{\tau}\left(C_1 + C_2'\frac{P_k}{\varepsilon}\right)\left(\zeta - \frac{2}{3}\right), \tag{5.15}$$

where ε is the dissipation, f is the elliptic relaxation term, L and τ are the length scale and the time scale of turbulence limited by the Kolmogorov scales and the Durbin's realizability constraints as lower and upper bound, respectively, given as [18]

$$\tau = \max\left[\min\left(\frac{k}{\varepsilon}, \frac{a}{\sqrt{6}C_\mu|S|\zeta}\right), C_\tau\left(\frac{\nu^3}{\varepsilon}\right)^{1/2}\right], \tag{5.16}$$

$$L = C_L\max\left[\min\left(\frac{k^{3/2}}{\varepsilon}, \frac{k^{1/2}}{\sqrt{6}C_\mu|S|\zeta}\right), C_\eta\left(\frac{\nu^3}{\varepsilon}\right)^{1/4}\right]. \tag{5.17}$$

The model coefficients are set to

$$C_\mu = 0.22, \quad C_{\varepsilon 1} = 1.4(1 + 0.012/\zeta), \quad C_{\varepsilon 2} = 1.9, \quad C_1 = 0.4, \tag{5.18}$$

$$C_2' = 0.65, \quad \sigma_k = 1, \quad \sigma_\varepsilon = 1.3, \quad \sigma_\zeta = 1.2, \tag{5.19}$$

$$C_\tau = 6.0, \quad C_L = 0.36, \quad C_\eta = 85, \quad a = 0.6. \tag{5.20}$$

In comparison to the standard $k - \varepsilon$ model, the $\zeta - f$ model solves two additional equations, namely the equation for the wall normal velocity scale ratio ζ and the equation for the elliptic relaxation term f. The velocity scale ratio is defined as

$$\zeta = \frac{v^2}{k}, \tag{5.21}$$

where v is the wall normal velocity fluctuation. Due to the introduction of the velocity scale ratio ζ, which contains anisotropic information in the near wall region, the simulation results for the flow with near wall anisotropic turbulence, such as the wall bounded flows, are improved.

The dynamic turbulent viscosity is then calculated using

$$\mu_{\mathrm{t}} = \alpha\rho^{\mathrm{inc}}C_\mu\zeta k\tau, \tag{5.22}$$

with α being calculated by

$$\alpha = \min\left\{\frac{(C_{\mathrm{s}}\Delta)^2\sqrt{S_{ij}S_{ij}/2}}{C_\mu\zeta k\tau}, 1\right\}. \tag{5.23}$$

5.2 Validation

In order to validate the new implemented LNS models, a well-established 2d periodic hill test case is utilized. This test case is a benchmark case for computing separated flows and validating hybrid LES/RANS models, since the correct prediction of the separated and reattached flows are quite challenging [39, 87]. Due to the anisotropy appearing in the separation region, the conventional RANS models based on the isotropic assumption are usually not able to deliver correct prediction of the separation and the reattachment points, while the hybrid LES/RANS models can provide more accurate results.

The streamwise, wall-normal and spanwise length of the computational domain are $L_x = 9h$, $L_y = 3.036h$ and $L_z = 4.5h$, respectively, where h is the hill's height. The boundaries in the streamwise direction are not defined as inflow and outflow, instead, periodic boundary conditions are applied, ensuring that a fully developed turbulent flow can be achieved without any turbulence generating methods. Figure 5.1 shows the computational domain discretized with a mesh of $72 \times 80 \times 32$ grid points. The first cell near the wall lies in the viscous sublayer, with the non-dimensional wall distance being $y^+ \approx 1$. The simulation is conducted over 55 flow-through times, ensuring to obtain fully developed flow status. The flow's Reynolds number is given as

$$Re_\mathrm{b} = u_\mathrm{b} h / \nu = 10595, \tag{5.24}$$

with the bulk velocity u_b. The desired bulk velocity is achieved by tuning the pressure gradient acting on the flow.

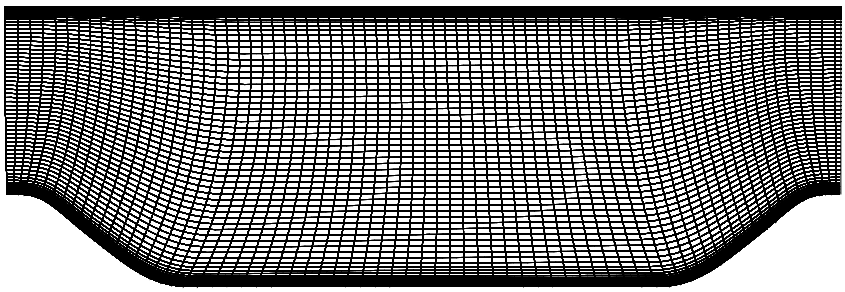

Figure 5.1: Computational grid for the 2d periodic hill (every 2 lines are shown).

The simulation results are compared with the reference LES data extracted from [24], in which a computational grid with 5 million cells is used.

A transient plot of the velocity u^inc obtained by the $\zeta - f$ based LNS model is given in Fig. 5.2. It can be seen that the LNS model is able to resolve the fine turbulent eddies, indicating qualitatively that the hybrid model can deliver LES-like results. The

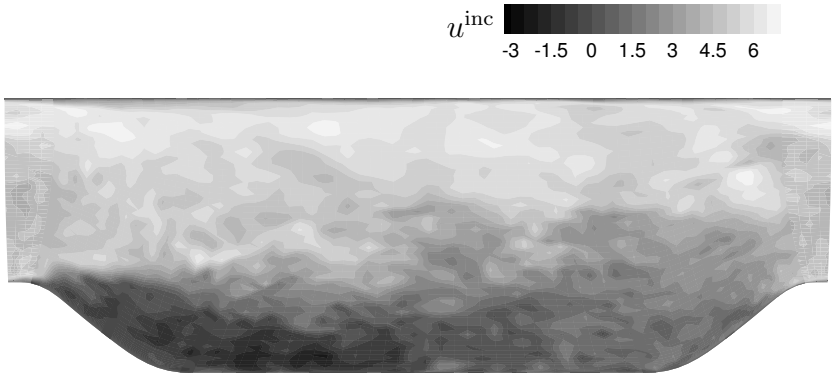

Figure 5.2: Transient velocity u^{inc}

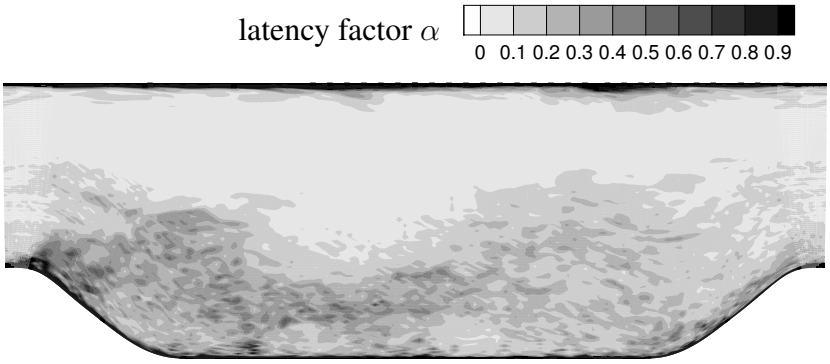

Figure 5.3: Distribution of the LES mode and the RANS mode

functionality of the hybrid model is further examined in Fig. 5.3, where the latency factor α is presented. In the near wall region, the LNS model is switched to the RANS model, while in the major interior region the LES mode is chosen. This scenario is consistent with our original intention, because the RANS model is reliable, robust and less computationally expensive in the near wall region, while the LES model delivers more accurate results in the remaining regions.

The streamlines of the mean velocities u^{inc}, shown in Fig. 5.4, illustrates that the flow has a recirculation region separated from the main stream. The separation of flow occurs almost directly after the inflow and the flow is reattached to the bottom wall approximately in the middle of the computational region, which agrees well with the

reference (4.72 m) from a qualitative point of view.

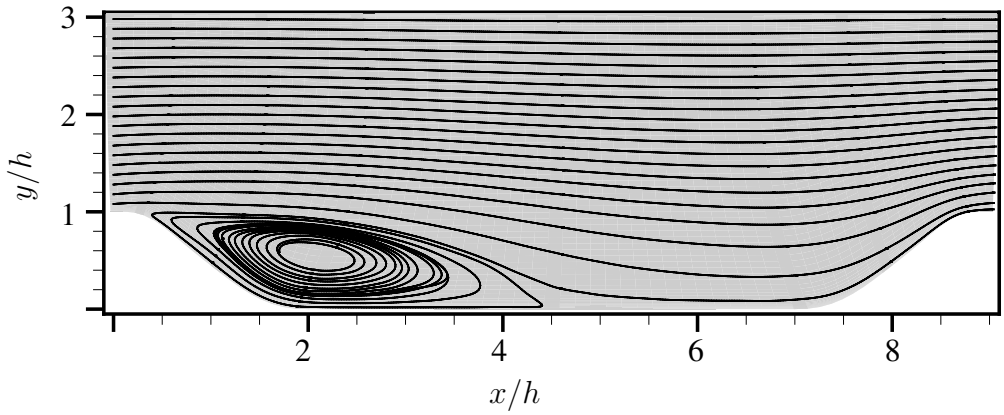

Figure 5.4: The streamlines of the flow past the periodic 2d hills obtained by the LNS model.

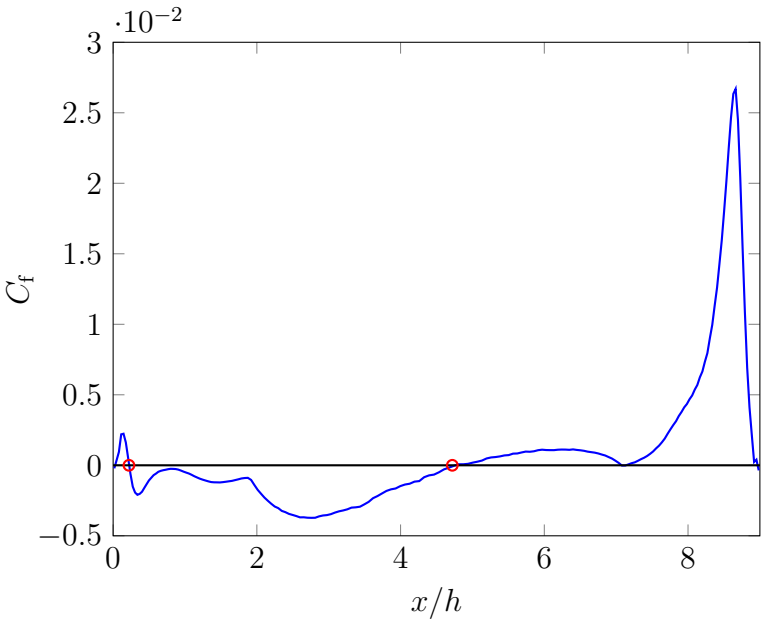

Figure 5.5: Determination of the separation and the reattachment points based on the skin friction coefficient.

In order to quantitatively compare the positions of the separation and the reattachment points with the reference data, the friction coefficient C_f is utilized. Figure 5.5 shows the friction coefficient C_f depicted over x-coordinates. When C_f drops to 0 the first

time, the flow is separated from the bottom wall. When C_f increases to 0 again, the flow is reattached to the wall. The separation and the reattachment points are marked in red in Fig. 5.5.

Table 5.1: Separation and reattachment points.

	LES [24]	$k-\epsilon$ based LNS	$\zeta-f$ based LNS
x_s/h	0.22	0.21	0.22
x_r/h	4.72	4.68	4.74

The separation and reattachment points of the LNS models are compared with those of the reference LES model in Table 5.1. It can be concluded that the results of the LNS model agree well with the reference data.

The streamwise and wall normal velocities are averaged in time and in the spanwise direction. In Fig. 5.6, the streamwise velocity profiles are compared with the reference LES data. Overall, the simulation results obtained from the LNS hybrid models based on the Chien $k-\varepsilon$ model and the $\zeta-f$ model agree well with the reference LES data. Only minor differences can be found for the position $x = 0.05h$. The wall normal velocity profiles v, shown in Fig. 5.7, also present good agreement with reference LES data.

The Reynolds stress profiles $\overline{u'u'}$ and $\overline{u'v'}$ obtained from the LNS simulations also agree with the reference LES data very well, as shown in Fig. 5.8 and Fig. 5.9. In particular, the $\zeta-f$ based LNS model delivers better results than the Chien $k-\varepsilon$ based LNS model. This is plausible, because the underlying $\zeta-f$ model introduces the mechanism to capture the anisotropic character in the flow. This advantage makes the $\zeta-f$ based LNS model behaves better when operating in the RANS mode.

In summary, the new implemented LNS model delivers satisfactory simulations results. Therefore, the LNS model is validated and can be used for further investigations. As the $\zeta-f$ based LNS model provides better results than the Chien $k-\varepsilon$ model, we will only use this model in the aeroacoustic simulations in the subsequent chapters.

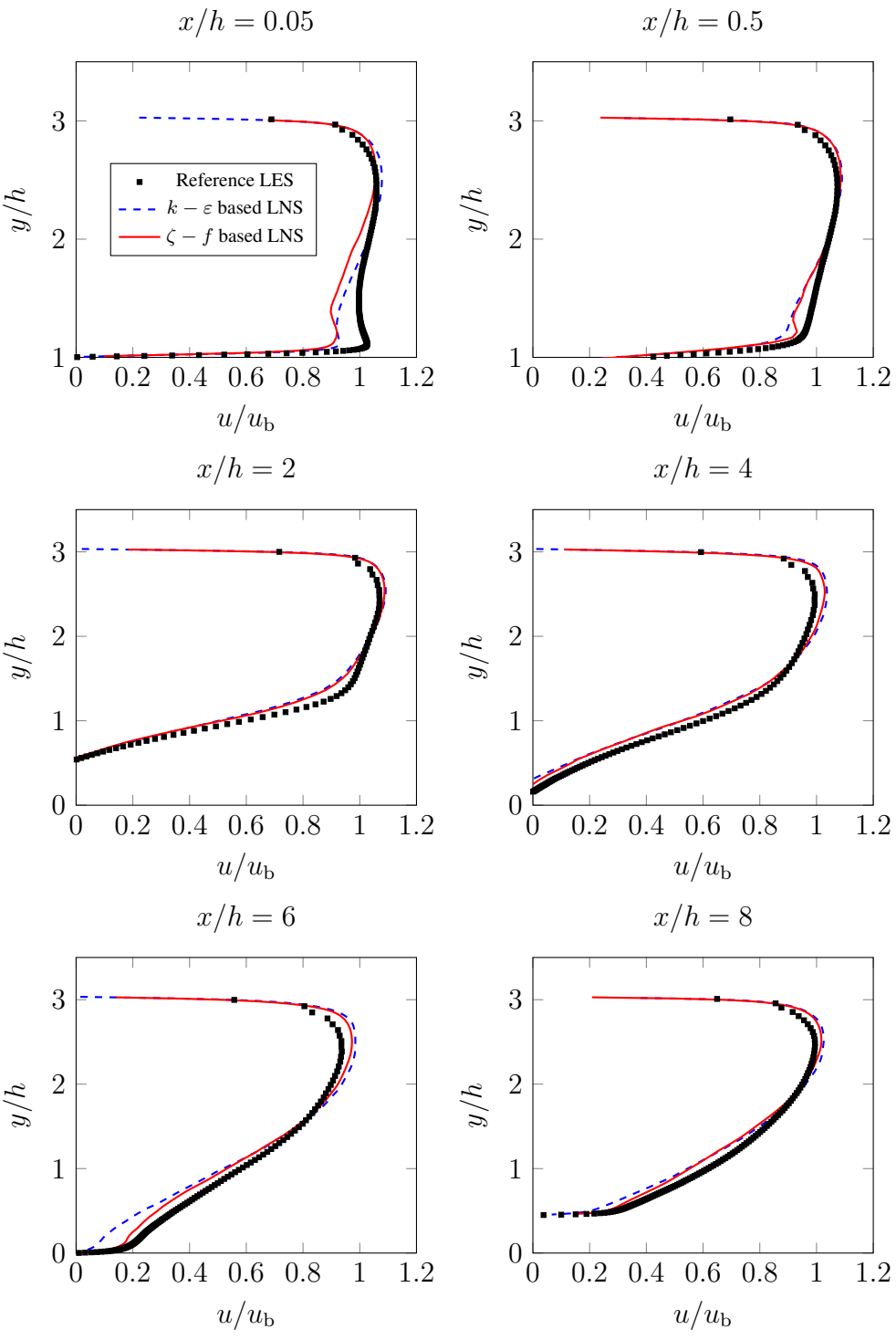

Figure 5.6: Profiles of the mean velocity in the streamwise direction.

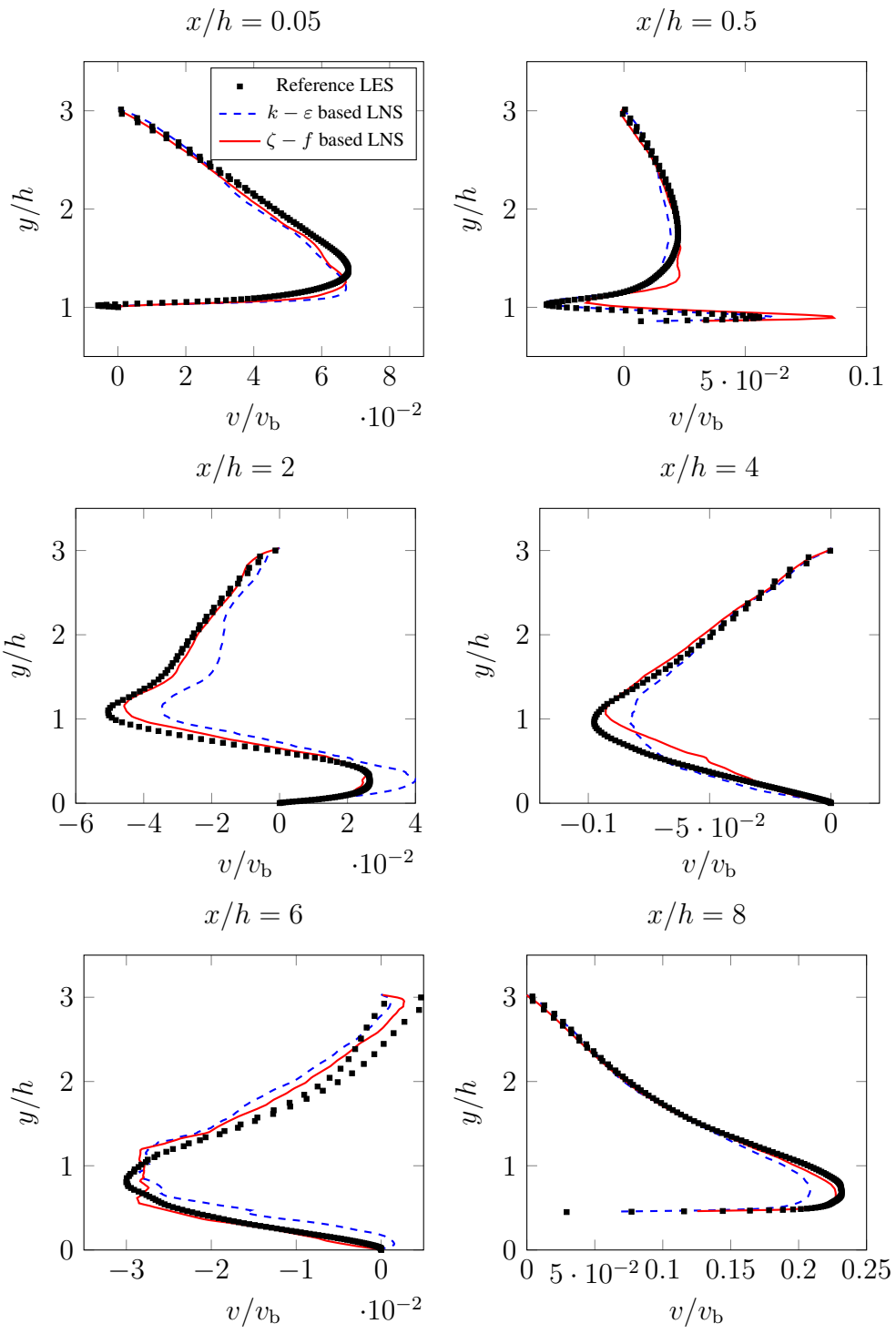

Figure 5.7: Profiles of the mean velocity in the wall normal direction.

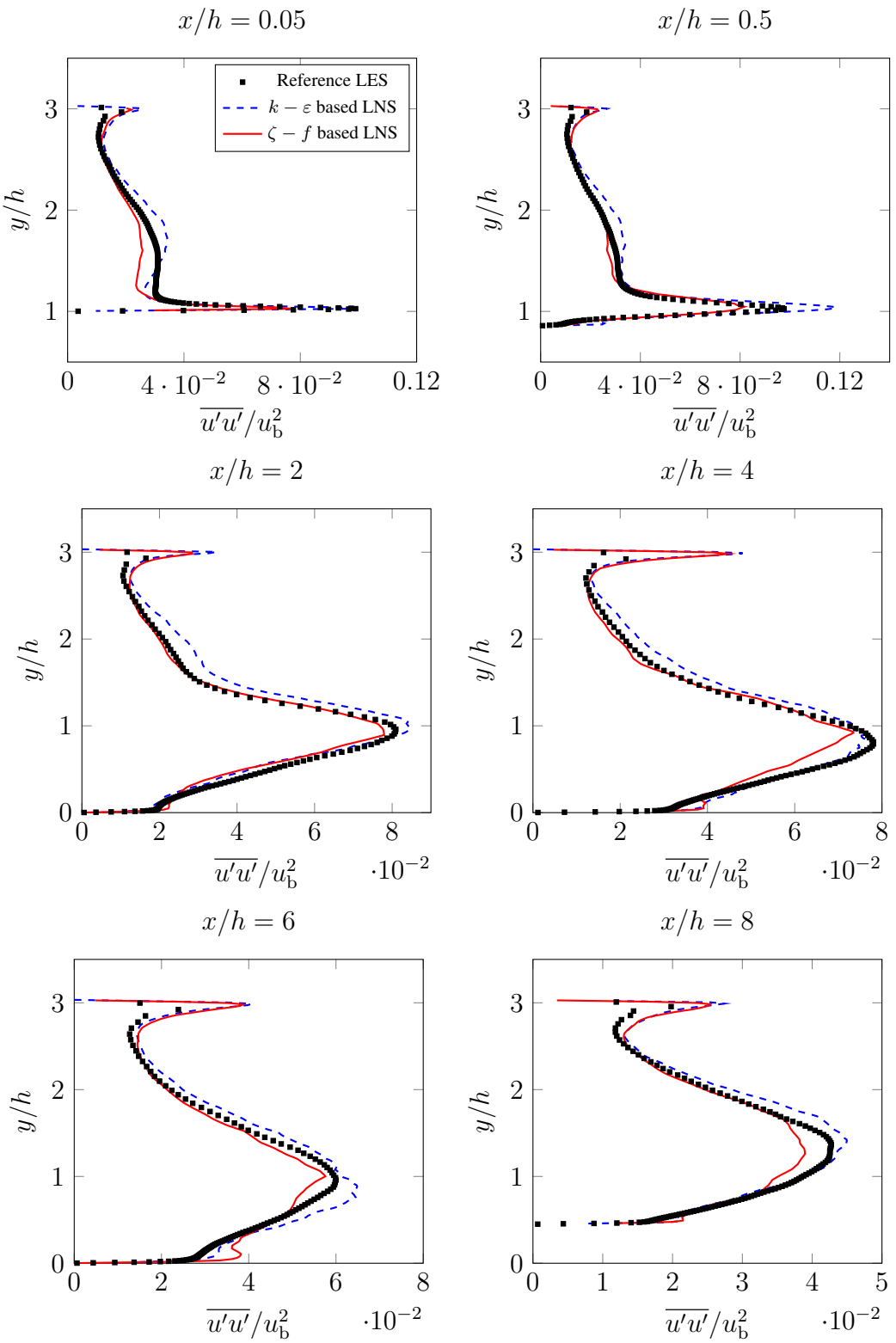

Figure 5.8: Profiles of the normalized Reynolds stress $\overline{u'u'}/u_\mathrm{b}^2$.

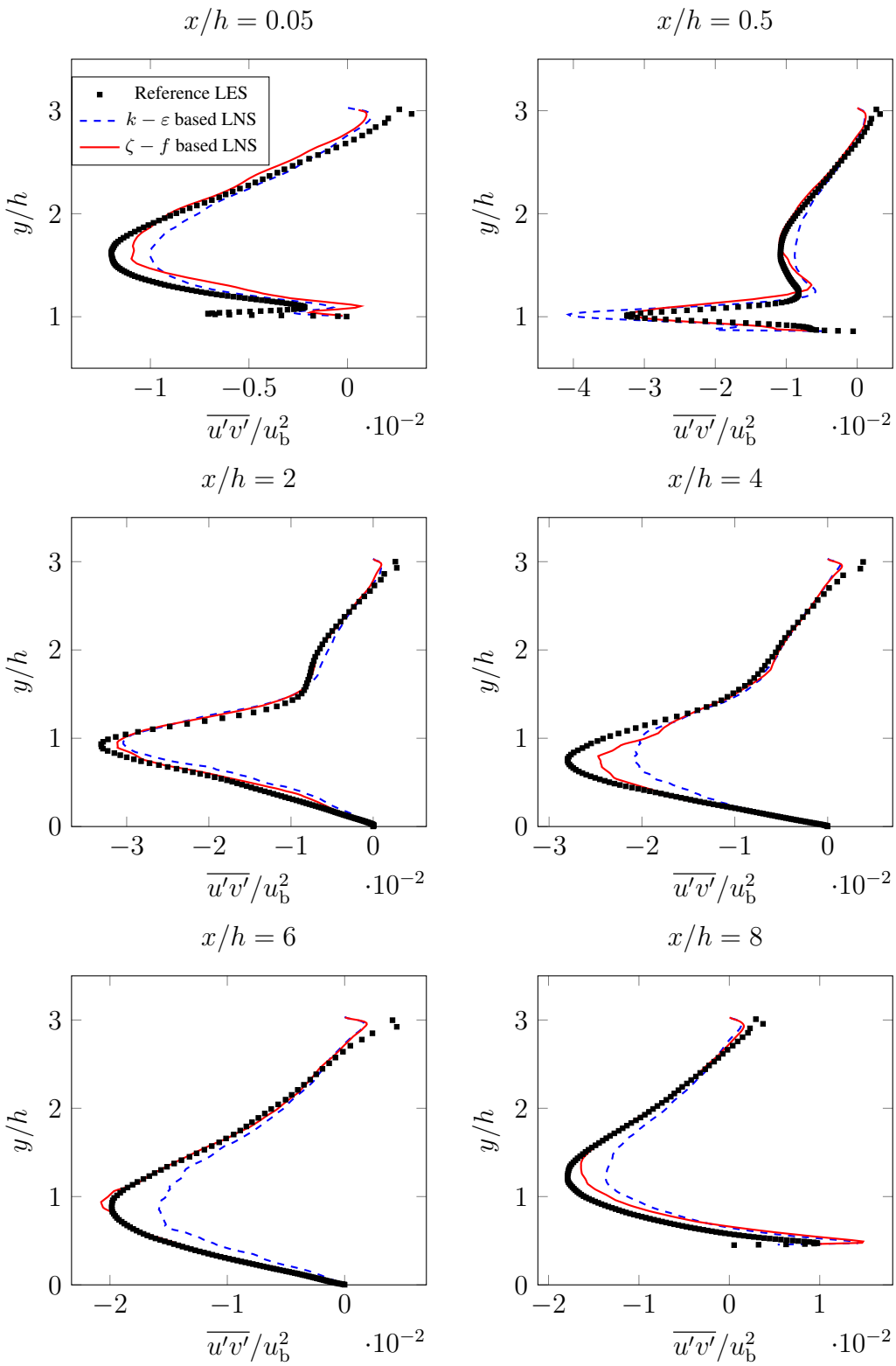

Figure 5.9: Profiles of the normalized Reynolds stress $\overline{u'v'}/u_\mathrm{b}^2$.

CHAPTER 6

COUPLING OF THE FLOW SOLVER AND THE ACOUSTIC SOLVER

In the existing in-house solver FASTEST, the flow and the acoustic computations are conducted sequentially on the same processors. Figure 6.1 schematically illustrates the structure of the existing solver.

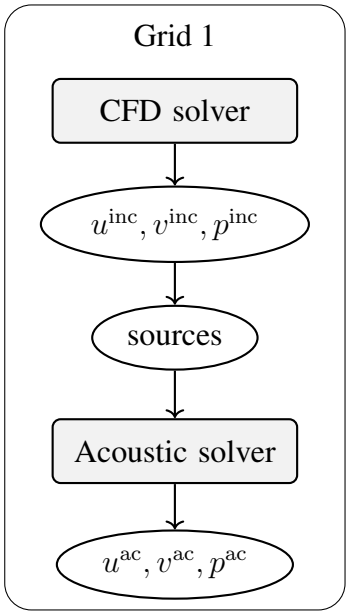

Figure 6.1: Schematic description of the structure of the existing solver.

In the existing solver, the CFD solver computes the pressure and velocities first, which are used to calculate the acoustic sources. Subsequently, the acoustic quantities are

solved on the same processors. Consequently, only the same grid can be used for the computation of the flow and the sound. However, the investigation of aeroacoustic simulation focuses mostly on the acoustic results in the far field, which expands the computational domain greatly in comparison to pure CFD problems, leading to a drastic increase of the computational expense. Especially for turbulent flows, the high requirements on the grid spacings makes it extremely time-consuming to conduct aeroacoustic simulations on a large computational domain.

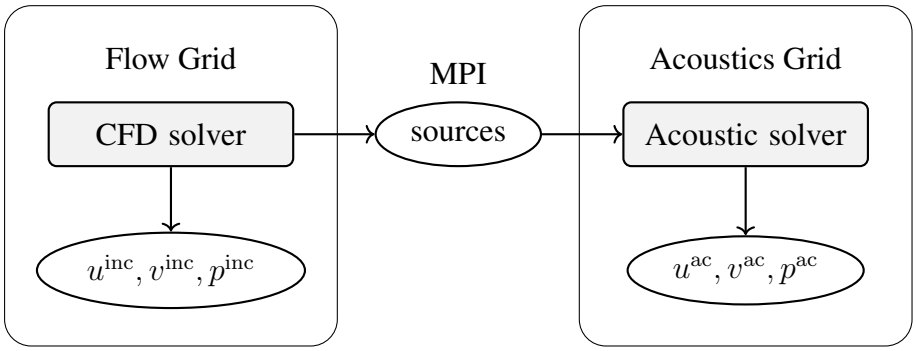

Figure 6.2: Schematic description of the structure of the modified Solver.

In this work, a new coupling between the CFD solver and the acoustic solver, shown in Fig. 6.2, is implemented, allowing the flow and the sound to be computed on different grids. In the new coupling, the acoustic sources are first calculated on the flow grid, which are then transfered to the acoustic solver and interpolated on the acoustic grid. By doing so, the computational cost is greatly reduced.

A comparison between the existing integrated solvers and the new implemented coupled solvers in terms of the computational cost is given in Fig. 6.3. It can be seen that the domain size of the coupled flow solver is greatly reduced while the space size of the coupled acoustic solver can be increased. The new coupling of the flow solver and the acoustic solver also corresponds to the characteristics of the multi-scale separation introduced in Fig. 2.1.

6.1 Implementation

The CFD simulation is conducted using the existing flow solver in FASTEST. Within the flow solver, data for different blocks of the computational domain are operated by different processors. The exchange of the data between different processors are realized using OpenMPI. In the new coupling structure, communication between the flow solver and the acoustic solver needs to be implemented. Consequently, a new global MPI communicator is defined. Between the flow solver and the acoustic solver, the addresses of processors are determined with the help of the master processors,

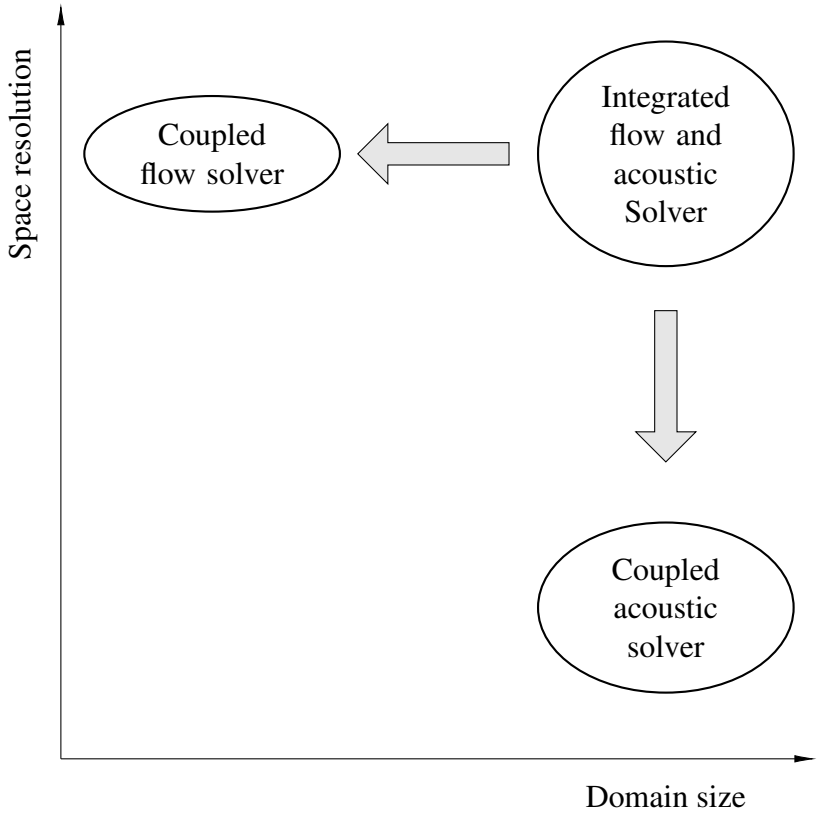

Figure 6.3: Description of the computational cost of the integrated acoustic solver and the coupled acoustic solver.

which are the first processors of the flow solver and the acoustic solver, respectively.

Figure 6.4 demonstrates the structure of the coupled flow and acoustic solvers. The coupling between the flow solver and the acoustic solver is performed in the following steps. First, the flow solver sends the coordinates data of the flow grid (x, y, z) to the acoustic solver. After receiving the coordinates data, the acoustic solver starts to find the 8 nearest CFD points circling each acoustic points, which are used to calculate the interpolation coefficient c_i. Second, the flow solver solves the Navier-Stokes equations to obtain the flow data, which are used to calculate the acoustic sources. Thereafter, the acoustic sources are transfered to the acoustic solver. Finally, the acoustic solver solves the LEE to obtain the acoustic field.

The search procedure is initialized from the first acoustic cell. In order to find the nearest CFD cells to the current acoustic cell, the first CFD cell is examined. First of all, we determine in which relative direction to the current acoustic point lies the CFD point. Here, the space is divided by the $x - y$ plane, the $x - z$ plane and the $y - z$ plane to obtain 8 different relative directions, namely from the north-east-top direction to the south-west-bottom direction. For each direction, a nearest CFD point is needed

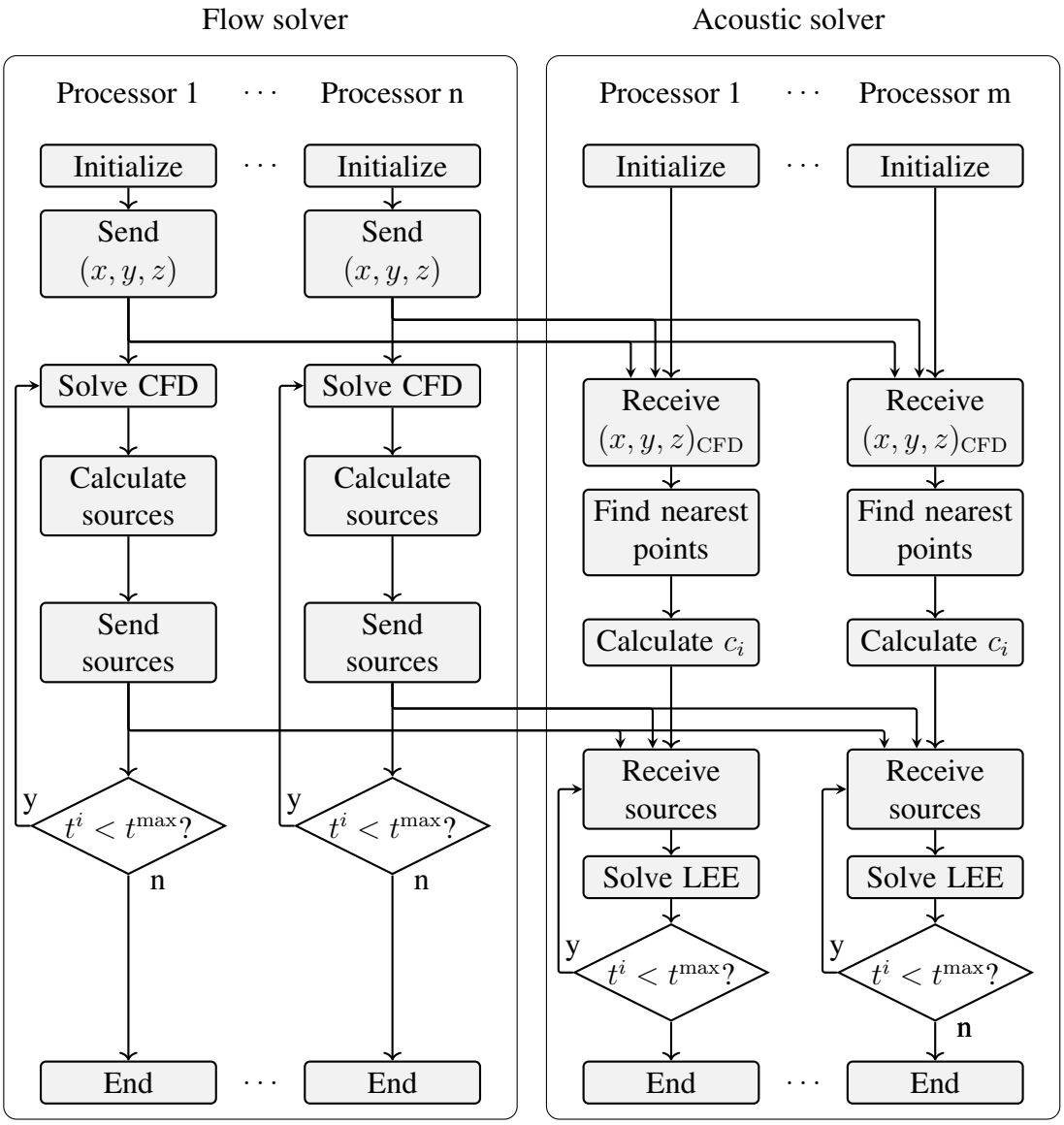

Figure 6.4: Illustration of the structure of the implementation.

to be found. In the next step, we calculate the distance D between the current acoustic point and the current CFD point. If this distance D is less than the previous minimum in this direction D_i, this distance minimum in this direction is replaced by D, the CPU index and the cell index are saved. If the distance D is larger than D_i, we move on to the next CFD cell and repeat the same procedures to determine its relative direction and distance. When all the 8 nearest cells to the current acoustic cells are found, we move to the next acoustic cell. The search procedure is finished when for all acoustic cells the corresponding nearest CFD points are found.

The search procedure requires a loop over all CFD cells in the loop over all acoustic

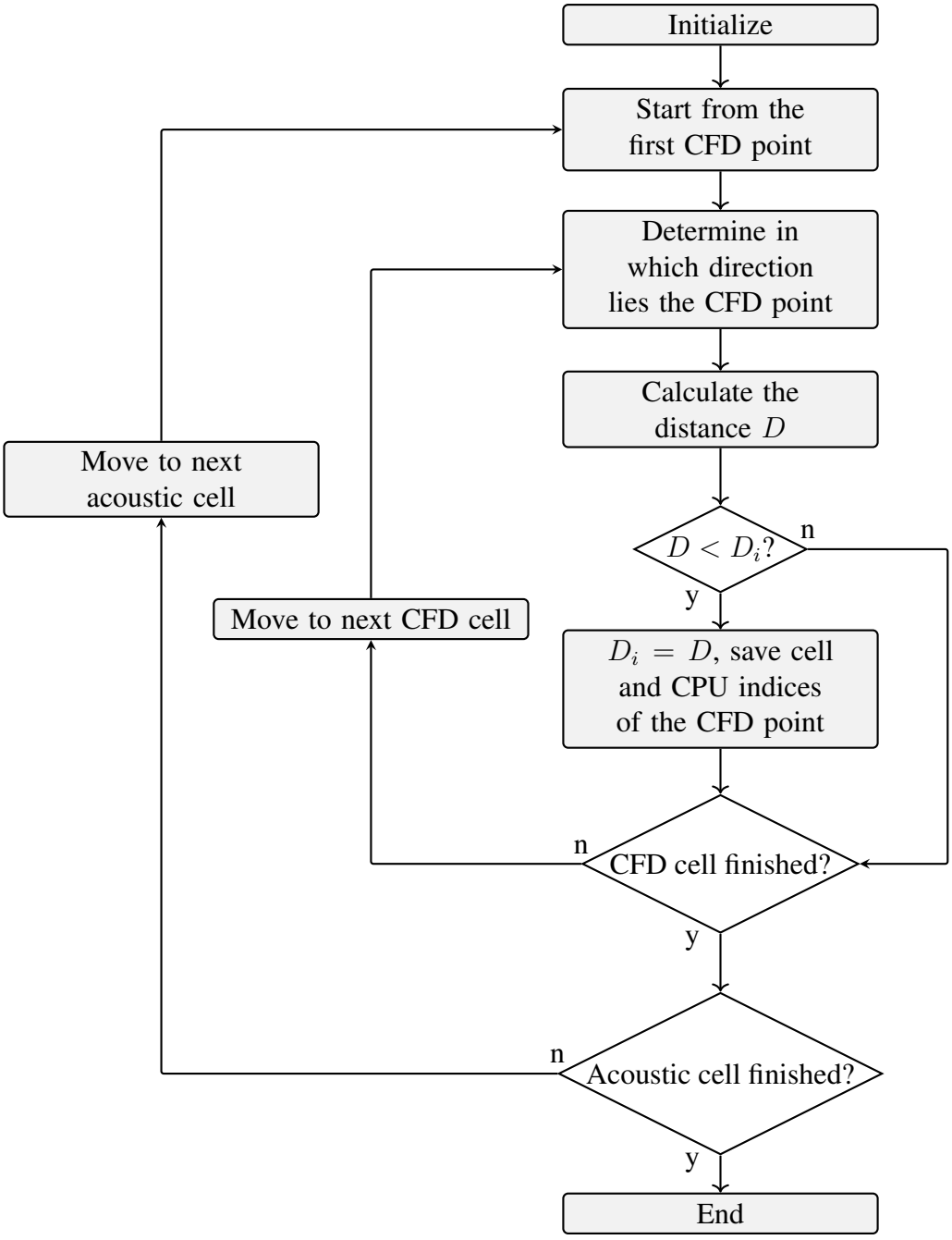

Figure 6.5: Calculation of the nearest points.

cells. Therefore, if the numbers of the CFD grid and the acoustic grid are in the order of 10^6, then the search procedure needs 10^{12} times distance calculations and comparisons, which takes 5-10 core-hours to compute. Therefore, this search procedure is conducted only once for a new combination of the flow grid and the acoustic grid, then

the required CPU and cell indices are written in files. The next time when using the same grids, the required data are read directly from the files saved previously.

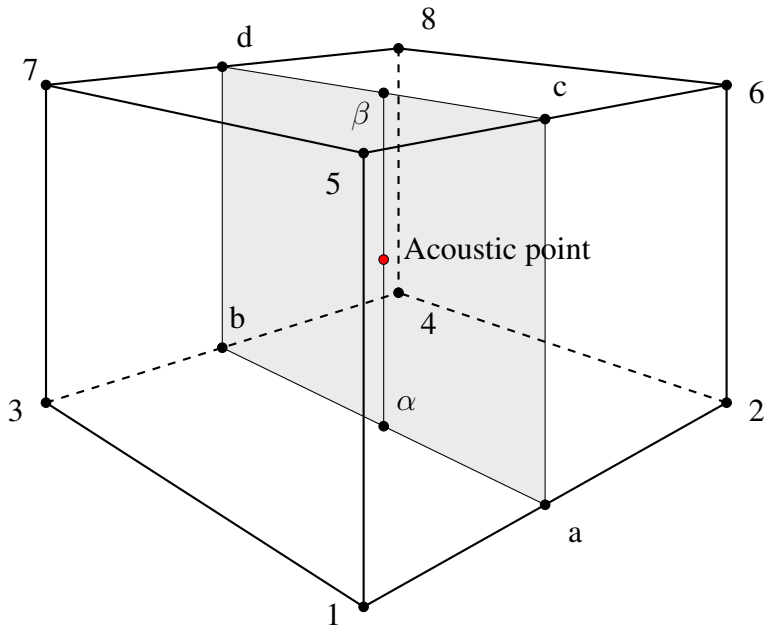

Figure 6.6: Schematic description of the 8 points and the notations used for the trilinear interpolation.

Figure 6.6 shows the 8 nearest CFD points and their notations circling the corresponding acoustic point. It is noteworthy that the interpolation formula is derived on Cartesian grids. For non-Cartesian grids, the interpolation error is expected to be larger. However, due to its complexity, the interpolation of non-Cartesian grids is not implemented in this work. The objective now is to calculate the acoustic source term on the acoustic point based on the acoustic source terms on the 8 CFD points. In order to achieve this objective, a trilinear interpolation is applied. The relation between the acoustic source terms is given as

$$\begin{aligned} s =& c_1 s_1 + c_2 s_2 + c_3 s_3 + c_4 s_4 \\ &+ c_5 s_5 + c_6 s_6 + c_7 s_7 + c_8 s_8, \end{aligned} \tag{6.1}$$

where s is the acoustic source on the acoustic cell center, $s_i,\ i = 1, \ldots, 8$ represent the acoustic sources on the 8 CFD cell centers. The coefficients are given as

$$c_1 = \frac{z_\beta - z}{z_\beta - z_\alpha} \frac{y_b - y}{y_b - y_a} \frac{x_2 - x}{x_2 - x_1}, \tag{6.2}$$

$$c_2 = \frac{z_\beta - z}{z_\beta - z_\alpha} \frac{y_b - y}{y_b - y_a} \frac{x - x_1}{x_2 - x_1}, \tag{6.3}$$

$$c_3 = \frac{z_\beta - z}{z_\beta - z_\alpha} \frac{y - y_a}{y_b - y_a} \frac{x_4 - x}{x_4 - x_3}, \tag{6.4}$$

$$c_4 = \frac{z_\beta - z}{z_\beta - z_\alpha} \frac{y - y_a}{y_b - y_a} \frac{x - x_3}{x_4 - x_3}, \tag{6.5}$$

$$c_5 = \frac{z - z_\alpha}{z_\beta - z_\alpha} \frac{y_d - y}{y_d - y_c} \frac{x_6 - x}{x_6 - x_5}, \tag{6.6}$$

$$c_6 = \frac{z - z_\alpha}{z_\beta - z_\alpha} \frac{y_d - y}{y_d - y_c} \frac{x - x_5}{x_6 - x_5}, \tag{6.7}$$

$$c_7 = \frac{z - z_\alpha}{z_\beta - z_\alpha} \frac{y - y_c}{y_d - y_c} \frac{x_8 - x}{x_8 - x_7}, \tag{6.8}$$

$$c_8 = \frac{z - z_\alpha}{z_\beta - z_\alpha} \frac{y - y_c}{y_d - y_c} \frac{x - x_7}{x_8 - x_7}. \tag{6.9}$$

6.2 Verification

In the following, the new coupling between the flow solver and the acoustic solver is verified in two test cases. In the first test case, the correctness of the interpolation is examined. For this purpose, the acoustic source is artificially given in the flow solver and sent to the acoustic solver, where the acoustic sources are interpolated. After the interpolation, the acoustic sources are compared with the analytical solution to verify the interpolation process. In the second test case, the acoustic results obtained from the coupled acoustic solver are compared with that from the integrated acoustic solver. The objective here is to determine if the new coupling part works correctly in the aeroacoustic simulation.

6.2.1 Test case 1: Taylor-Green function

In this test case, the acoustic source term in the flow solver is given by the Taylor-Green function

$$\frac{\mathrm{d}p^{\mathrm{inc}}}{\mathrm{d}t} = \sin(2\pi x)\cos(2\pi y), \tag{6.10}$$

which is often used in the verification of numerical methods due to its characteristics of smoothness and differentiability.

The flow domain and the acoustic domain are both cubes with a length of 1 m and 1.4 m in each direction. The computational domain of the flow is discretized using 64 CVs in each direction, while the acoustic domain uses 4 different grids, starting from

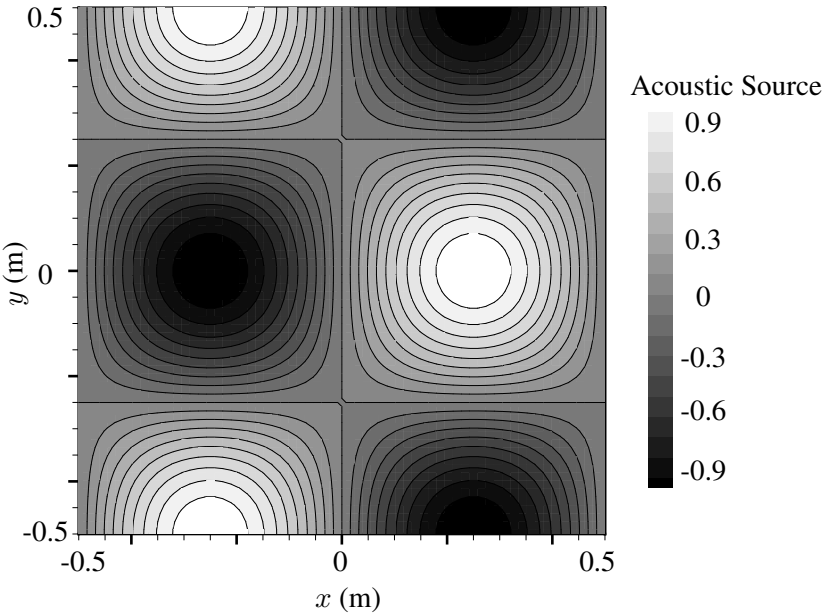

Figure 6.7: Acoustic source given in the flow solver.

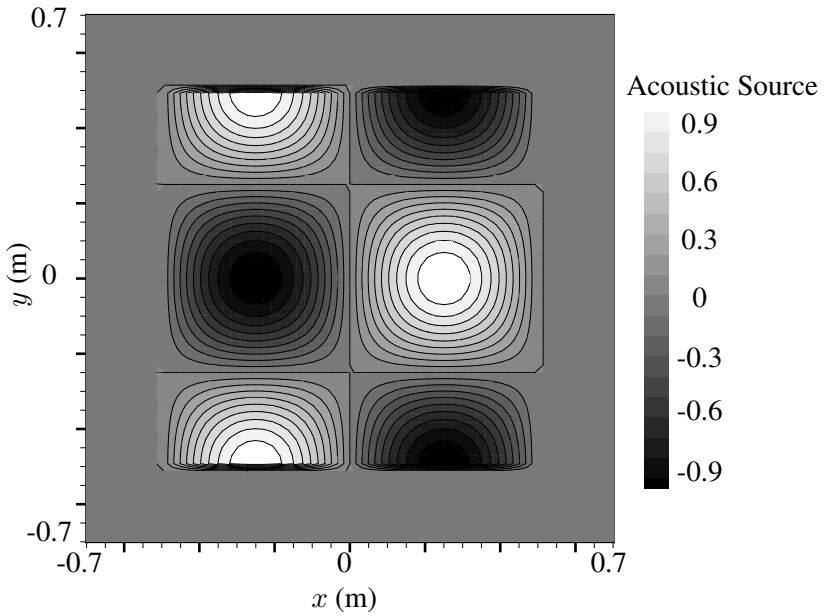

Figure 6.8: Acoustic source obtained from the acoustic solver.

8 to 64 CVs in each direction. The flow solver and the acoustic solver distribute the simulations on 8 CPUs, respectively.

Figure 6.7 shows the analytical acoustic sources at the xy-plane. The interpolated acoustic sources obtained from the acoustic solver are presented in Fig. 6.8. One can see that the acoustic sources are reconstructed with a relatively high accuracy, except for the boundaries of the flow domain, where an abrupt increase or drop is present. This mismatch at the boundaries occurs, because the interpolation process here involves points outside the flow domain. This misbehaviour could be improved by dealing with the boundaries using a different interpolation strategy. For example only the points inside the flow domain are used. Such a strategy is not implemented in the frame of this work, since the flow domains that are investigated later for aeroacoustic problems are all so big that the acoustic sources near the flow boundaries approaches 0 and therefore the errors introduced by this mismatch are negligible.

The accuracy of the interpolation is described using the L^2 Norm error

$$e = \sqrt{\sum_{i=1}^{N} e_{i,h}^2}, \tag{6.11}$$

where N is the total number of CVs and $e_{i,h}$ is the error of each CV

$$e_{i,h} = s_{\mathrm{num},h} - s_{\mathrm{ana}}, \tag{6.12}$$

with the numerical source $s_{\mathrm{num},h}$ and the analytical source s_{ana}. Table 6.1 shows the calculated errors for different grid resolutions. The errors are plotted against the width of the CV in Fig. 6.1. Here an order close to 2 is clearly recognizable, indicating a correct implementation of the interpolation part.

CVs in each direction	L^2 Norm error	Calculated order
8	0.073223	-
16	0.019030	1.92
32	0.004804	1.98
64	0.001204	1.99

Table 6.1: Error and the order of the error for different grid resolutions.

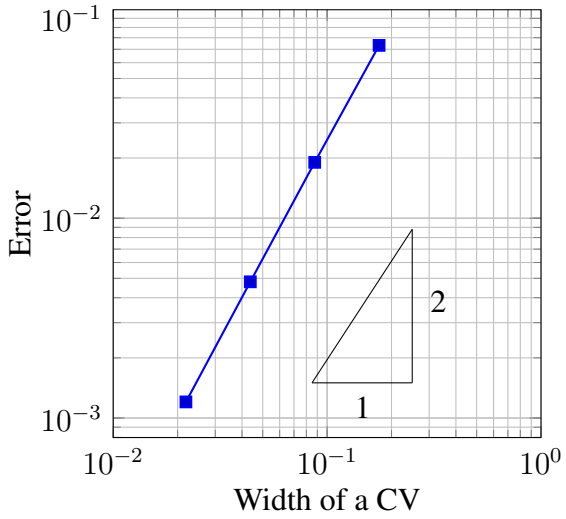

Figure 6.9: Order of the error.

6.2.2 Test case 2: Gaussian pulse

In the following, the new coupling part implemented in this work is verified with the help of a Gaussian pulse test case. Here, the acoustic waves obtained from the coupled acoustic solvers are compared with that from the integrated acoustic solver. Since the background flow is irrelevant in this test case, the velocities are set to 0. The acoustic waves are generated artificially using a Gaussian pulse

$$p^{\mathrm{inc}} = -10^4 \cdot e^{-50(x^2+y^2+z^2)} \cdot \cos(200\pi t). \tag{6.13}$$

The acoustic source generated from this given time-dependent pressure at time $t = 0\,\mathrm{s}$ is given in Fig. 6.10. A Gaussian pulse with the center at (0,0,0) can be observed. The flow domain is a cube with side lengths of 1 m in each direction, which is discretized using a grid of $128 \times 128 \times 128$ CVs. The acoustic domain of the coupled acoustic solver has a length of 1.4 m in each direction, which is discretized using 4 different grids. The simulations of the flow and the sound are conducted using 8 CPUs, respectively. The time step is set to 5×10^{-4} s for the flow solver and the acoustic solver, making the Courant number for the integrated acoustic solver 0.1 and the coupled acoustic solver 0.07. Some important material values are listed in Table 6.2.

Table 6.2: Material values for the Gaussian pulse test case.

sound speed c [m/s]	fluid density ρ [kg/m^3]	dynamic viscosity μ [kg m^{-1} s^{-1}]
340	1.225	1.81×10^{-5}

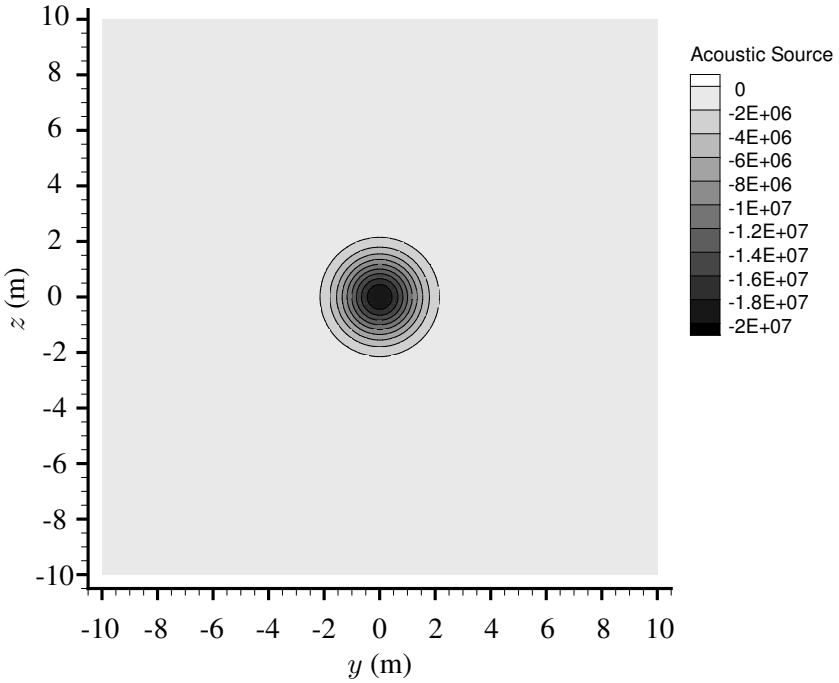

Figure 6.10: The acoustic source at time t=0 s.

Subsequently, the acoustic quantities obtained from the integrated acoustic solver and the coupled acoustic solver at 0.035 s are examined. The acoustic pressure obtained from the integrated acoustic solver is shown in Fig. 6.11a. The coupled acoustic solver delivers a result with excellent similarity, as shown in Fig. 6.11b. The coupled acoustic domain here is discretized by $128 \times 128 \times 128$ CVs. A great agreement can also be observed for the acoustic density, as shown in Fig. 6.12.

In Fig. 6.13 and Fig. 6.14 the acoustic velocities in x- and y-direction are compared. For both cases the coupled acoustic solver provides results with very high accuracy.

The acoustic data at point (0.5,0.5,0.5) is recorded for the integrated and the coupled acoustic solver. Figure 6.15 compares the acoustic pressure for the integrated acoustic solver and the coupled acoustic solver. A time period of 0.05 s is observed. As the number of CVs in each direction increases from 64 to 128, the errors decreases correspondingly. The same phenomenon can be observed for the acoustic density and acoustic velocities, as shown in Fig. 6.16, 6.17 and 6.18, respectively. Based on the correct convergence to the reference results, the new implemented coupled acoustic solver is hereby verified for Cartesian grids.

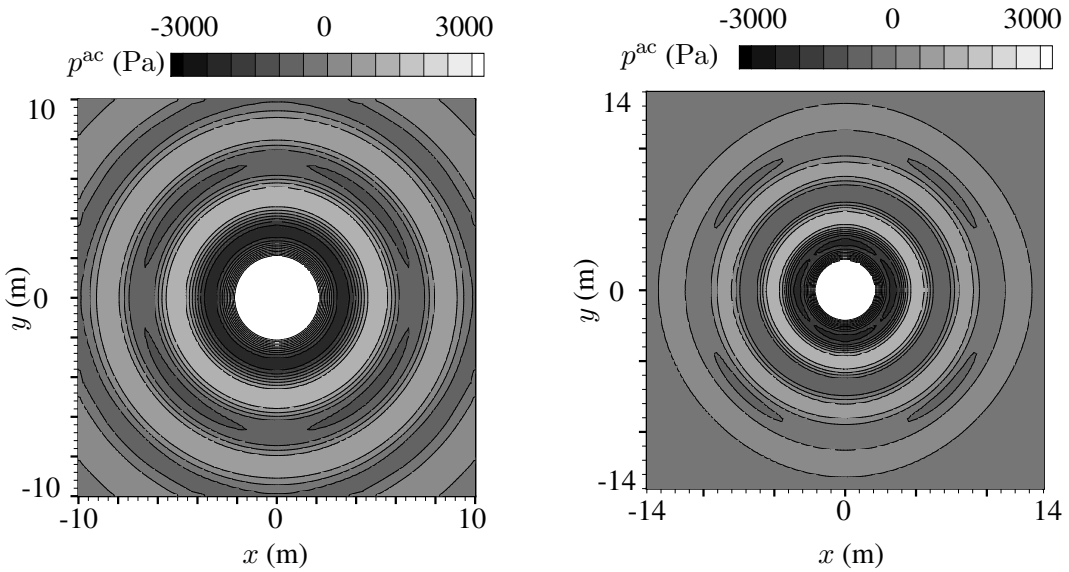

(a) Acoustic pressure obtained from the integrated acoustic solver at $t = 3.5 \times 10^{-2}$ s.

(b) Acoustic pressure obtained from the coupled acoustic solver at $t = 3.5 \times 10^{-2}$ s.

Figure 6.11: Comparison of the acoustic pressure.

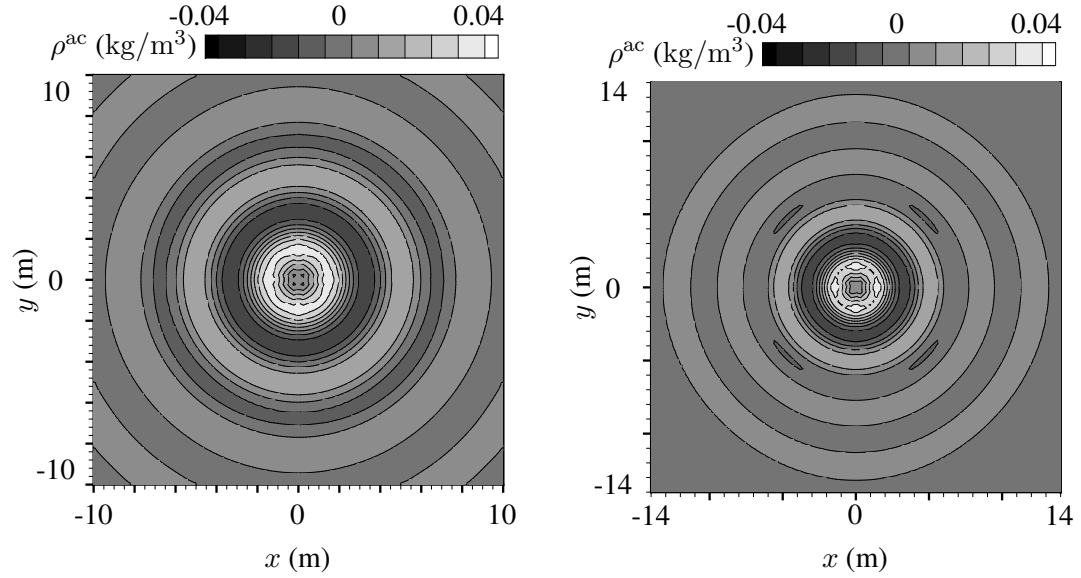

(a) Acoustic density obtained from the integrated acoustic solver at $t = 3.5 \times 10^{-2}$ s.

(b) Acoustic density obtained from the coupled acoustic solver at $t = 3.5 \times 10^{-2}$ s.

Figure 6.12: Comparison of the acoustic density.

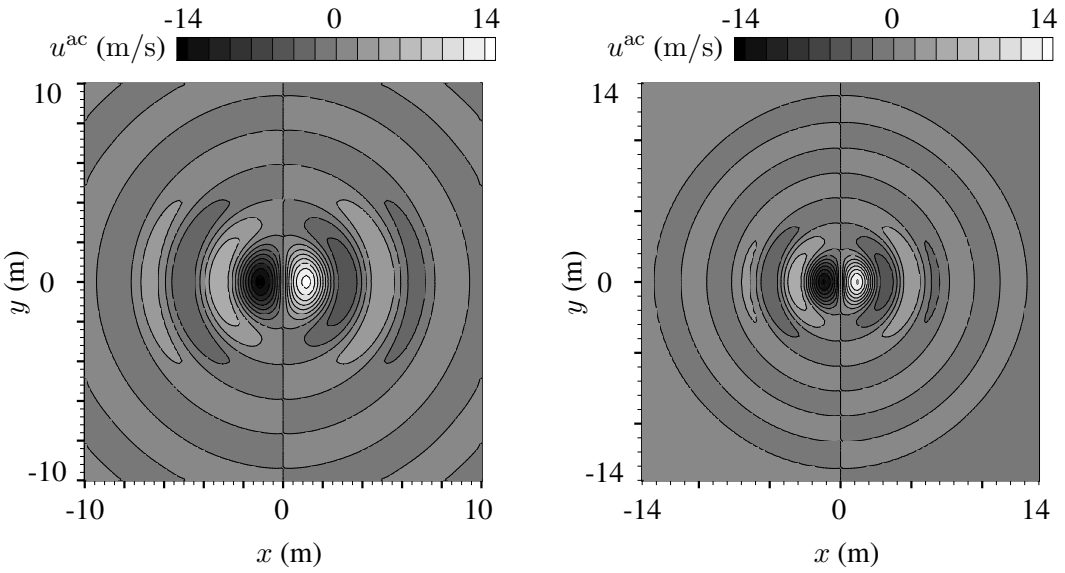

(a) Acoustic velocity in x-direction obtained from the integrated acoustic solver at $t = 3.5 \times 10^{-2}$ s.

(b) Acoustic velocity in x-direction obtained from the coupled acoustic solver at $t = 3.5 \times 10^{-2}$ s.

Figure 6.13: Comparison of the acoustic velocity in x-direction.

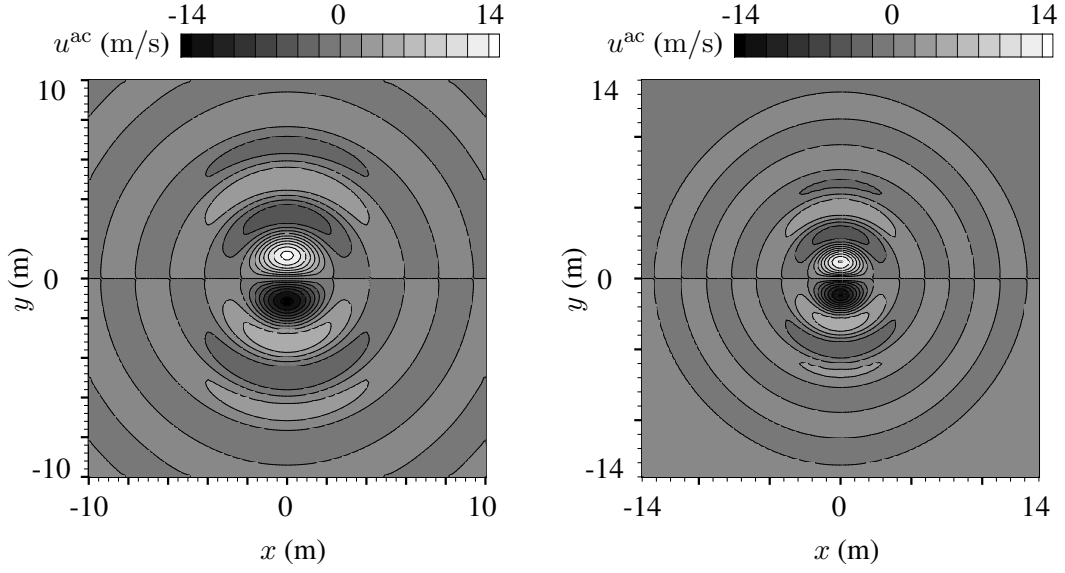

(a) Acoustic velocity in y-direction obtained from the integrated acoustic solver at $t = 3.5 \times 10^{-2}$ s.

(b) Acoustic velocity in y-direction obtained from the coupled acoustic solver at $t = 3.5 \times 10^{-2}$ s.

Figure 6.14: Comparison of the acoustic velocity in y-direction.

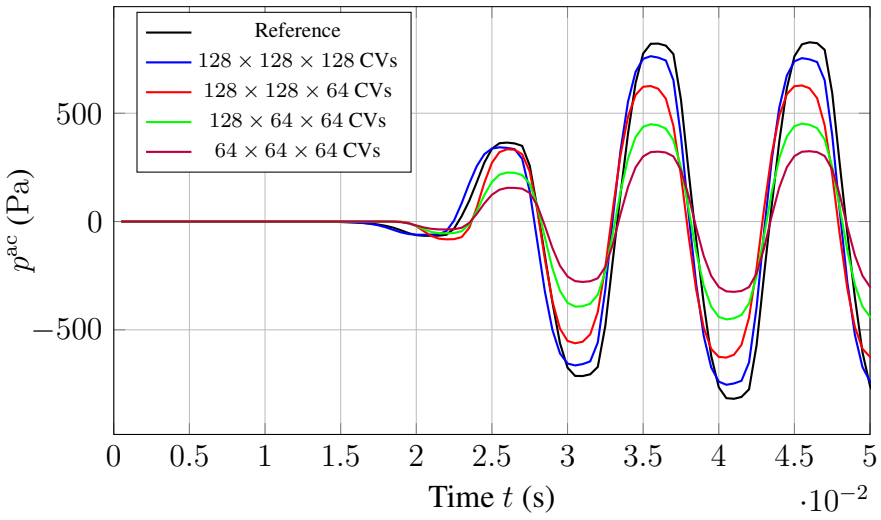

Figure 6.15: Acoustic pressure at point (5,5,5).

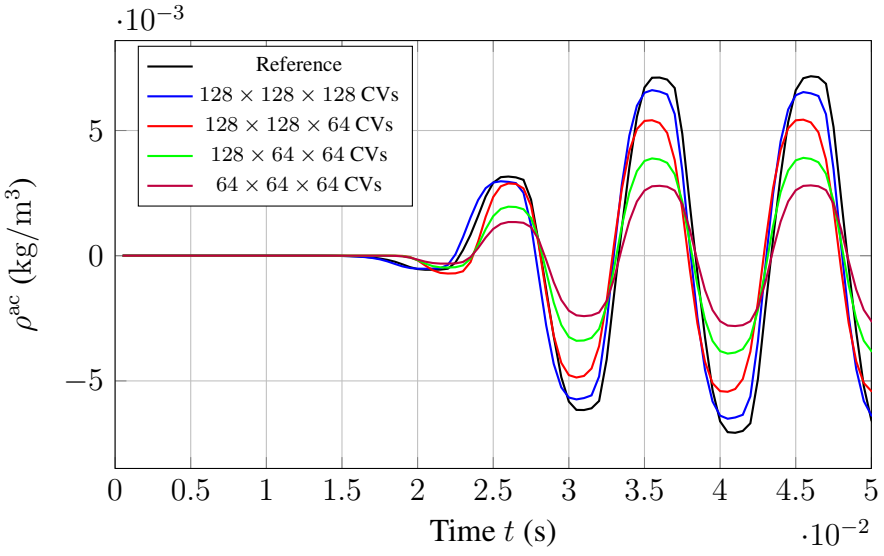

Figure 6.16: Acoustic density at point (5,5,5).

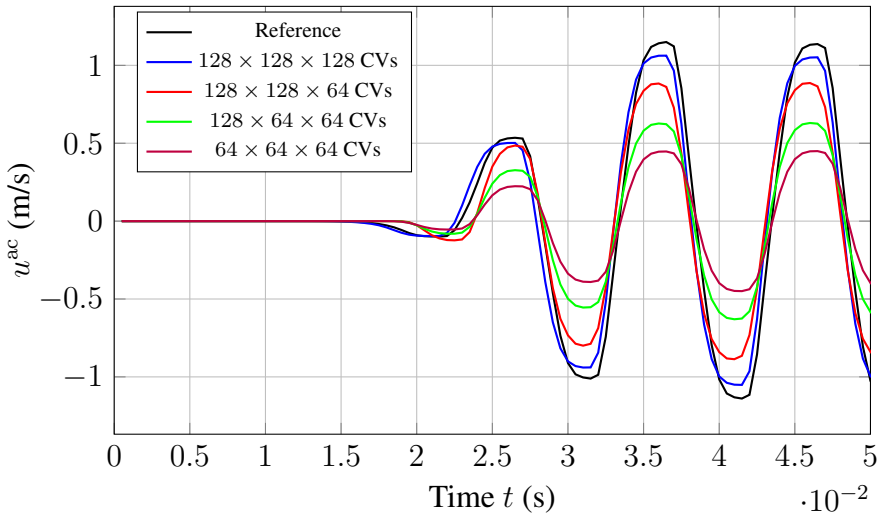

Figure 6.17: Acoustic velocity in x-direction at point (5,5,5).

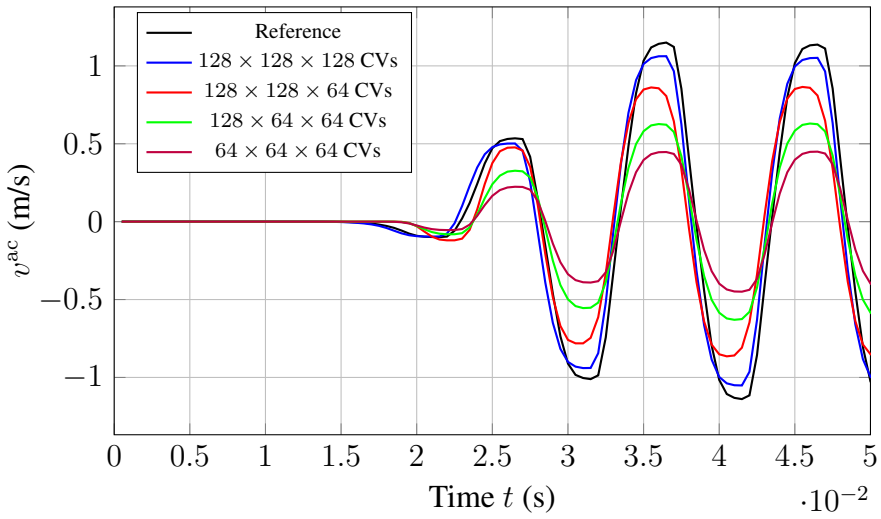

Figure 6.18: Acoustic velocity in y-direction at point (5,5,5).

CHAPTER 7

RECONSTRUCTION OF THE HIGH-FREQUENCY ACOUSTIC COMPONENTS

As stated in Chapter 4 and Chapter 5, the basic idea of the hybrid LES/RANS models is that it can switch between the LES model and the RANS model in different regions in the computational domain, so that one can significantly reduce the computational cost, while the accuracy of the results is not noticeably downgraded. Note that the LES model only solves the large scale turbulence, while the small scale turbulence is implicitly taken into account, which is in most cases sufficient. By using a hybrid LES/RANS model, the resolved scale range is further narrowed. However, for aeroacoustic simulations, neglecting the small scale turbulence which contributes largely to the high-frequency acoustic components leads to incorrect results. Consequently, it is necessary to reconstruct the small scale turbulence. In this chapter, the basic function and the relevant parameter of the synthetic method, which is used in this work to reconstruct the small scale turbulence, are first outlined. Thereafter, the implementation and the verification of the synthetic method are introduced.

7.1 Synthetic method

The synthetic method developed by Batten et al. [3] reconstructs the turbulent velocity fluctuations based on the local length scales and time scales . The velocity fluctuations are given as

$$u_i^{\mathrm{syn}}(x_j,t) = a_{ik}\sqrt{\frac{2}{N}}\sum_{n=1}^{N}\left[p_k^n\cos\left(\hat{d}_j^n\hat{x}_j^n+\omega^n\hat{t}\right)+q_k^n\sin\left(\hat{d}_j^n\hat{x}_j^n+\omega^n\hat{t}\right)\right], \quad (7.1)$$

where L and τ are local length and time scales, N is set to 100, $\hat{x}_j$,$\hat{t}$, $\hat{d}_j^n$ and V are defined as

$$\hat{x}_j = 2\pi x_j/L, \quad \hat{t} = 2\pi t/\tau, \quad \hat{d}_j^n = d_j^n \frac{V}{c^n}, \quad V = L/\tau, \tag{7.2}$$

$$c^n = \sqrt{\frac{3}{2}\overline{u_l' u_m'} d_l^n d_k^n / d_k^n d_k^n}, \tag{7.3}$$

p_i^n and q_i^n are given as

$$p_i^n = \epsilon_{ijk}\eta_j^n d_k^n, \quad q_i^n = \epsilon_{ijk}\xi_j^n d_k^n, \tag{7.4}$$

with η_i^n, ξ_i^n, ω^n and d_i^n being random numbers with given mean and variance

$$\eta_i^n, \xi_i^n = N(0,1), \quad \omega^n = N(1,1), \quad d_i^n = N(0, \frac{1}{2}). \tag{7.5}$$

a_{ij} is the Cholesky decomposition of $\overline{u_i' u_j'}$

$$a_{ij} = \begin{pmatrix} \sqrt{\overline{u_1' u_1'}} & 0 & 0 \\ \overline{u_1' u_2'}/a_{11} & \sqrt{\overline{u_2' u_2'} - a_{21}^2} & 0 \\ \overline{u_1' u_3'}/a_{11} & (\overline{u_2' u_3'} - a_{21}a_{31})/a_{22} & \sqrt{\overline{u_3' u_3'} - a_{31}^2 - a_{32}^2} \end{pmatrix} \tag{7.6}$$

The work flow of the aeroacoustic simulation after the new implementation is shown in Fig.7.1. The required input data are the local Reynolds stress tensor, the time scale and the length scale, which can be provided by the RANS model. After the velocity fluctuations are calculated, the pressure fluctuations are obtained using the SIMPLE correction scheme, the standard method in the flow solver FASTEST used to solve the incompressible Navier-Stokes equations [70].

7.2 Verification

The synthetic method is verified with the help of a fully developed turbulent channel flow. The Reynolds number based on the half channel width is 395. The computational domain has a streamwise length of $L_x = 2\pi h$ and a spanwise length of $L_z = \pi h$.The length in the wall-normal direction is $L_y = 2h$. The computational grid consisting of $64 \times 100 \times 64$ cells is shown in Fig. 7.2. The dimensionless distance to the wall of the first cell $y^+ \approx 1$. The simulation is conducted for over 30 flow-through times to achieve statistically stable results.

Figure 7.3 shows the instantaneous velocity of the channel flow in x-direction obtained from the LNS model without the application of the synthetic model. As a

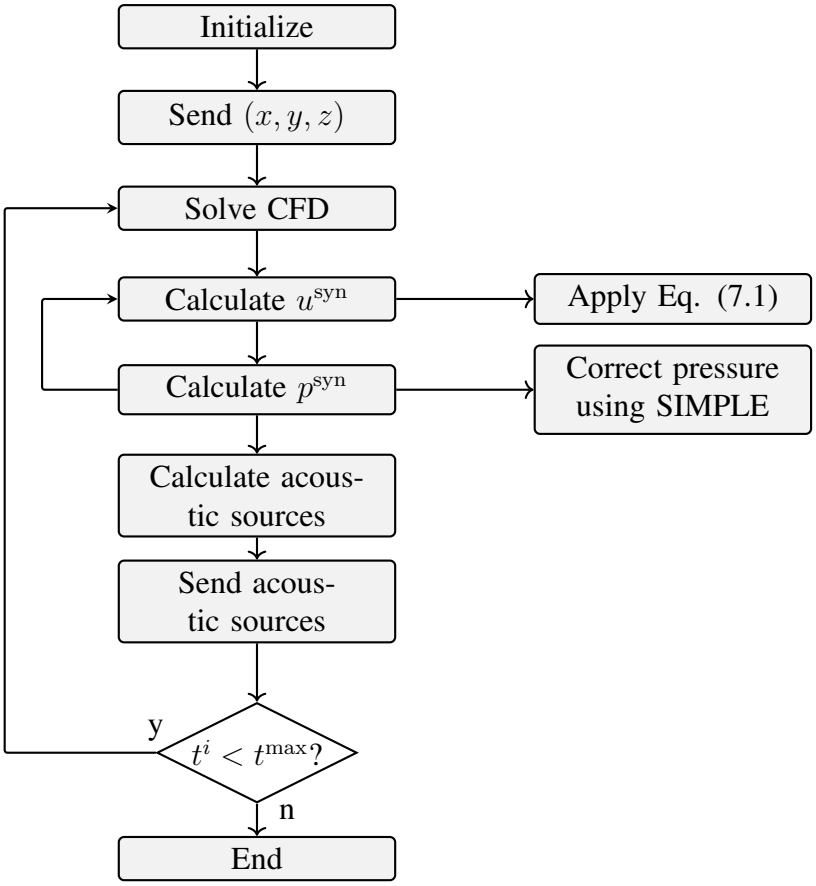

Figure 7.1: Schematic description of the calculation of the synthetic velocities and the synthetic pressure.

comparison, the synthetic velocity in x-direction is presented in Fig. 7.4. It can be observed that the additional fluctuations occur mainly in the region close to the wall, while very few synthetic fluctuations are generated near the center line of the channel. The region of the RANS model is illustrated with the help of the latency factor α of the LNS model, shown in Fig. 7.5. When α is close to 0, the DNS is used, while the RANS model is used for the region where α approaches 1, which indicates that the RANS model is used in the region close to the wall, while the DNS model is used in the remaining regions. Consequently, more synthetic fluctuations are constructed in the RANS region than in the DNS region, which is exactly as intended.

Another key factor to determine the functionality of the synthetic method is to examine the turbulence energy spectrum. For this purpose the velocities in x-direction are collected along three different lines, where y^+ is 39, 98 and 199, respectively, as shown with red dashed lines in Fig. 7.5. The turbulence energy spectrum obtained from the LNS with and without the synthetic method are compared with the DNS data, extracted from [55].

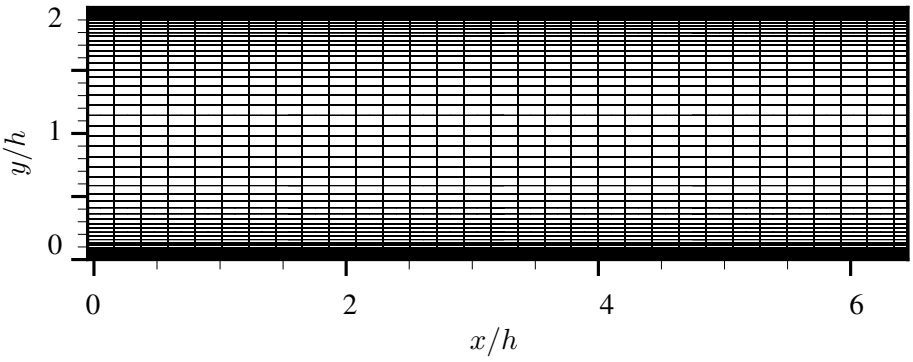

Figure 7.2: Discretization of the computational domain of the channel flow (every 2 lines are shown).

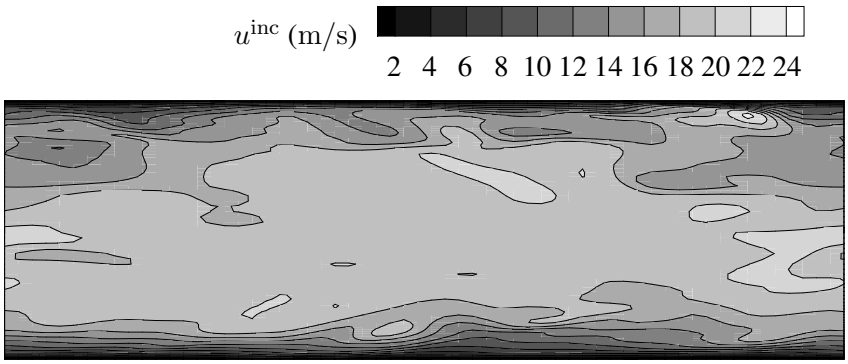

Figure 7.3: The instantaneous velocity in x-direction obtained from the LNS model without using synthetic method.

Figure 7.6 shows the turbulent energy E_{uu} at $y^+ = 39$, where the RANS model is switched on. The energy spectrum of the LNS model without the synthetic method decreases rapidly in the high frequency region compared with the DNS data, while the LNS model with the synthetic method is able to clearly improve the result. For the energy spectrum at $y^+ = 98$, shown in Fig. 7.7, a clear improvement in the large wave number region can be observed as well. At $y^+ = 199$ where an LES model is applied, the energy spectrum E_{uu} is also increased, as shown in Fig. 7.8. However, the reconstruction is so strong that the energy spectrum is for most wave numbers even larger than the DNS data. Overall, it can concluded that the new implemented synthetic method is able to reconstruct the small scale motions with satisfactory accuracy.

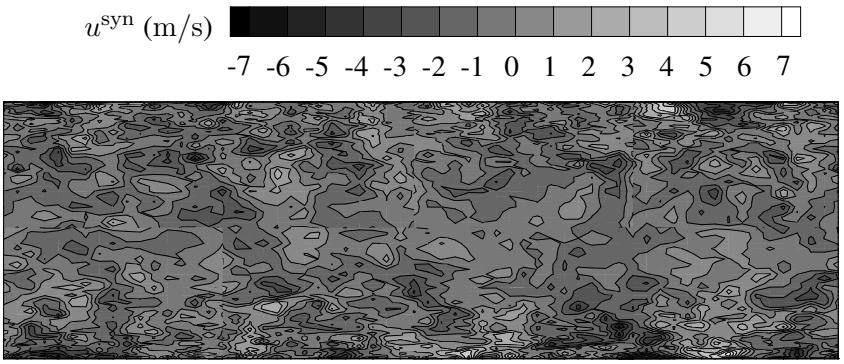

Figure 7.4: The synthetic velocity in x-direction.

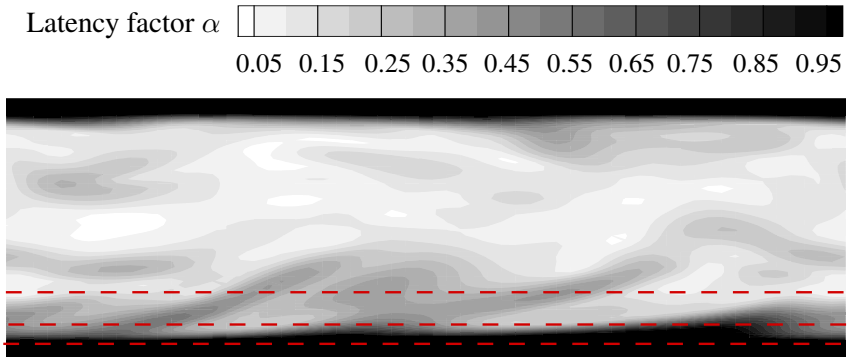

Figure 7.5: The latency factor α for the LNS model. The dashed lines are at $y^+ = 39$, $y^+ = 99$ and $y^+ = 199$, respectively. The velocities for the energy spectra analysis are collected along these three lines.

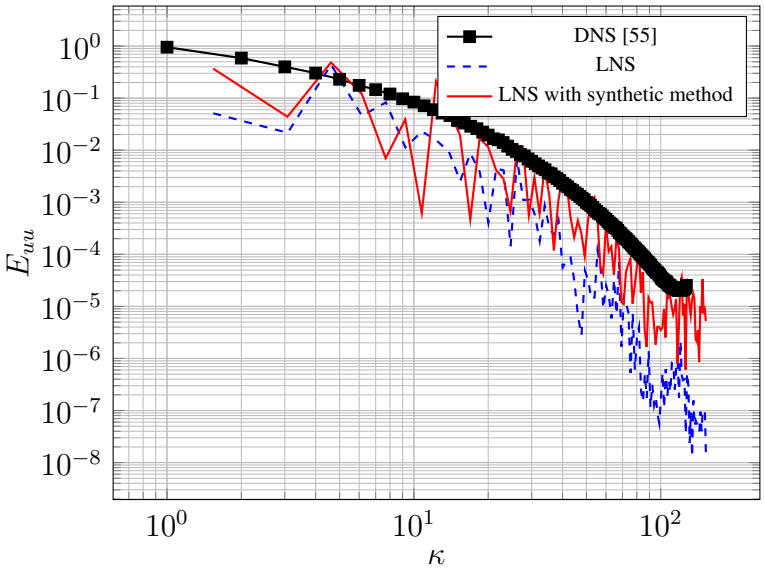

Figure 7.6: Comparison of the energy spectrum E_{uu} calculated with and without the synthetic method at $y^+ = 39$.

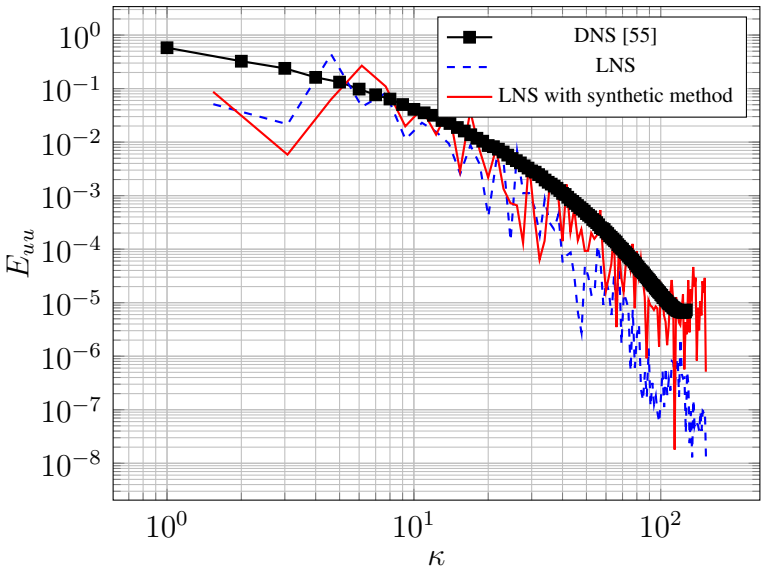

Figure 7.7: Comparison of the energy spectrum E_{uu} calculated with and without the synthetic method at $y^+ = 98$.

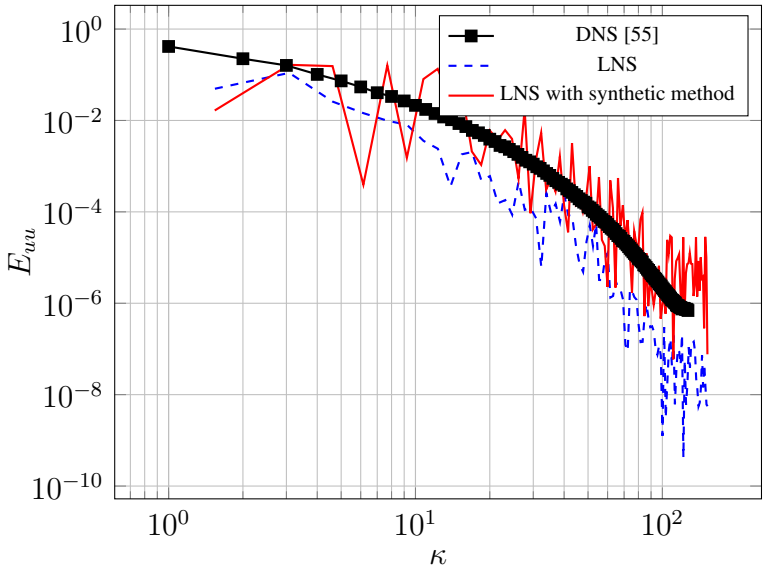

Figure 7.8: Comparison of the energy spectrum E_{uu} calculated with and without the synthetic method at $y^+ = 199$.

CHAPTER 8

AEROACOUSTIC RESULTS OF HYBRID LES/RANS MODELS

In this chapter, the performances of different hybrid LES/RANS models in aeroacoustic simulations are investigated using two test cases. The first test case is the flow past a circular cylinder, which is a classical benchmark testing separated flows. In this test case, we focus on examining the aeroacoustic results of the new implemented $\zeta - f$ based LNS model. Moreover, a comparison among the LNS model, the RANS model and the reference LES model is also conducted. The second test case is the NACA 0012 airfoil. The main task here is the comparison of the aeroacoustic behavior of different hybrid LES/RANS models. In particular, the new implemented LNS model is compared with an existing hybrid LES/RANS model, the VLES model.

8.1 Flow past a circular cylinder

The flow past a circular cylinder constitutes a well-established test case in the field of CFD. The flow pattern mainly depends on the Reynolds number

$$Re = \frac{\rho u_{\mathrm{b}} D}{\mu}, \tag{8.1}$$

with the bulk velocity u_{b}, the diameter of the cylinder D, density ρ and the dynamic viscosity of the fluid μ. A description of the flow patterns at different Reynolds numbers is given is Table 8.1.

The aeroacoustic simulations are designed oriented to the aeroacoustic experiment of Etkin et al. [19]. The bulk velocity is set to 68.6 $\mathrm{m/s}$. The Mach number based on the bulk velocity is then Ma=0.2, meaning that the incompressibility assumption

Table 8.1: Flow pattern of the flow past a circular cylinder depending on the Reynolds number [6].

Reynolds number	Flow pattern
Re < 5	Regime of unseparated flow
5 < Re < 40	A fixed pair of Föppl vortices in wake
40 < Re < 150	Vortex street is laminar
150 < Re < 300	Transition range to turbulence in vortex
300 < Re < 3×10^5	Vortex street is fully turbulent
3×10^5< Re < 3.5×10^6	Laminar boundary layer has undergone turbulent transition and wake is narrower and disorganized
Re > 3.5×10^6	Re-establishment of turbulent vortex street

still holds. The diameter of the cylinder is $D = 0.0125\mathrm{m}$. The Reynolds number is approximately 6×10^4, indicating that the flow is fully turbulent.

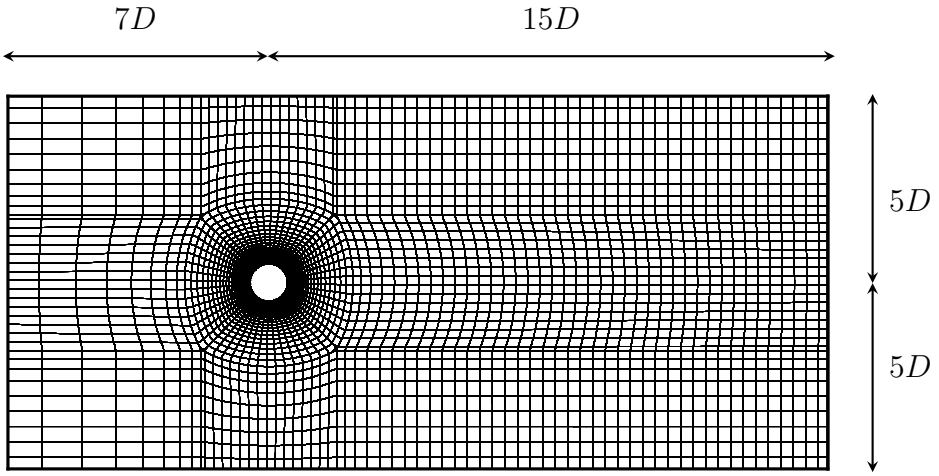

Figure 8.1: Discretization of the flow domain around the circular cylinder (every 2 lines are shown).

Figure 8.1 shows the geometry and the discretization of the computational domain for the $\zeta - f$ based LNS model. The computational domain has a length of $22D$ in x-direction and $10D$ in y-direction. In order to capture the three dimensional turbulent features, the length in z-direction is set to $4D$. The computational domain is discretized

using a block-structured grid with a dimensionless wall distance $y^+ < 1$, enabling a direct resolving down to the viscous layer.

The geometry and the discretization of the acoustic domain in given in Fig. 8.2. Due to the fact the experimental data are collected at a distance of $48D$ from the cylinder's center, the acoustic domain is designed with a length of $100D$ in x- and y-direction, while the length in z-direction is kept the same as the flow domain. It can be seen that the acoustic domain is significantly larger than the flow domain. Thus, the new coupling illustrated in Chapter 6 reduces the computational cost of the flow simulation enormously.

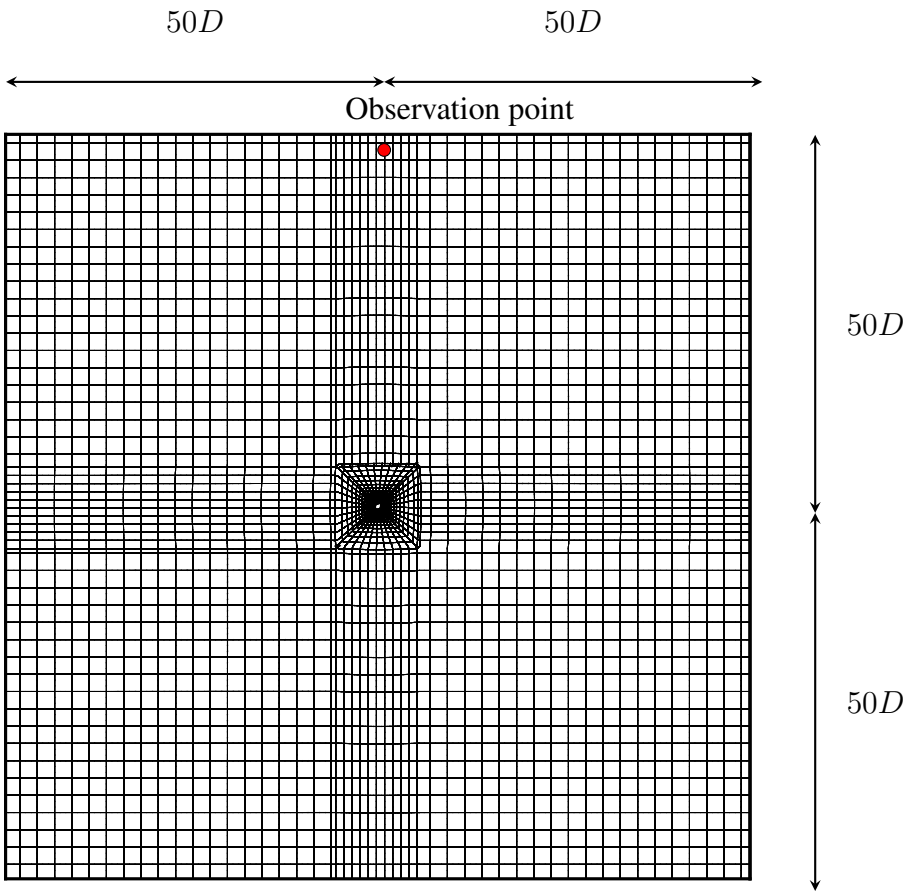

Figure 8.2: Discretization of the acoustic domain around the circular cylinder (every 3 lines are shown).

The grid resolution used for the LES model should be small enough to resolve 80% of the turbulence energy [57]. In order to fulfil this requirement, the mesh size for the LES model and the $\zeta - f$ based LNS model, listed in Table 8.2, are designed based on the suggestions in [90]. The number of CVs for the flow and acoustic domains are given in Table 8.3. The grid of the flow domain for the LES model has approximately

Table 8.2: Mesh size expressed in wall units for the LES and hybrid RANS/LES model.

	LES	Hybrid LES/RANS
Δx^+ (streamwise)	100	200
Δy^+ (wall-normal)	1	1
Δz^+ (spanwise)	20	60

5.6×10^6 CVs, while the grid for the $\zeta - f$ based LNS model is coarsened to 1.2×10^6 CVs. In order to exclude the influence of the grid resolution in the simulation results, the RANS model here uses the same grid as the hybrid LES/RANS model, which is actually more than enough for the RANS model. Regarding the time discretization, the second order fully implicit scheme is adopted, which has no stability problem when the CFL number is greater than 1 [70]. The time step for the flow solver is set to 3×10^{-6} s for all cases, resulting in a Courant number of approximately 2 for the $\zeta - f$ based LNS model. The time step for the acoustic solver is further divided 15 times, making the Courant number of the acoustics around 0.3 for the LNS model.

Table 8.3: Turbulence models and number of CVs.

Simulation	Turbulence model	CVs of flow domain	CVs of acoustic domain
No.1	LES	5.6×10^6	1.5×10^5
No.2	LNS	1.2×10^6	1.5×10^5
No.3	$k - \omega$ SST	1.2×10^6	1.5×10^5

A plot of the instantaneous acoustic pressure is given in Fig. 8.3. Periodic waves with a dipole pattern propagating through the field can be observed. In order to compare the turbulence models from a quantitative perspective, the acoustic pressure at the observation point marked in red in Fig. 8.2 are collected, which is placed at a distance of 48D from the cylinder's center perpendicular to the flow direction. The simulation results are compared with the experimental data extracted from [19].

Instead of an octave spectrum, an $1/3$ octave spectrum is used for the analysis. The comparison of the simulations and the experimental data are given in Fig.8.4. Similar results were reported by the author in [30].

Compared with the experimental data, the simulation result of the $k - \omega$ SST model presents significant deviation, while the LES model offers the best result among these three turbulence models. The LNS model provides a similar result to that of the LES model with some major differences in the range around the fundamental frequency.

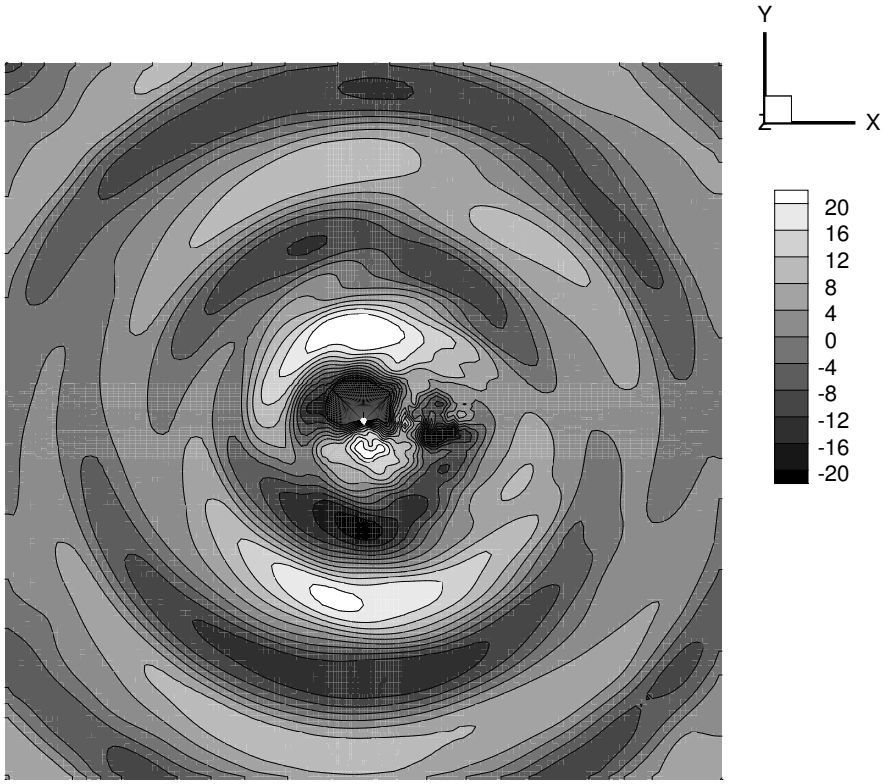

Figure 8.3: Instateous acoustic pressure (Pa) of the flow past the circular cylinder.

The fundamental frequency is the frequency where the first peak appears, which can be determined by observing the spectra directly after a Fourier transformation. Table 8.4 shows the fundamental frequencies obtained by different turbulence models. It can be seen that the relative error of the LES model is 6.1%, which confirms that the LES model is the most accurate one among the three turbulence models investigated in this work. The $k-\omega$ SST model has an error of 22%, while the LNS model improves it only slightly to 20.5%. It should be noted that the computational time required by the LNS model is only $1/4$ of that of the LES model. Therefore, it is not realistic that the LNS model delivers the same accuracy of the LES model. The objective of using hybrid LES/RANS models in the aeroacoustic simulations is to reduce the computational cost while not sacrificing too much accuracy. Therefore, it is of great importance to study how much deterioration in the accuracy is to be expected and what are the reasons leading to the deterioration.

It is particularly insightful to observe the acoustic sources obtained by different turbulence models. The acoustic sources provided by the LES model, shown in Fig.8.5,

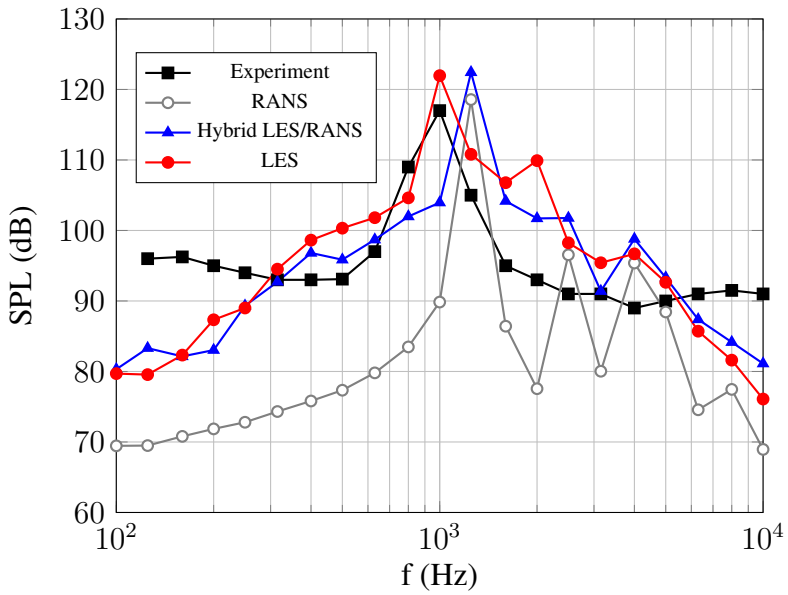

Figure 8.4: Comparison of SPL of different turbulence models with experimental data

Table 8.4: Fundamental frequency.

	Frequency (Hz)	Error
Experiment	1000	-
LES	1061	6.1%
LNS	1205	20.5%
RANS ($k-\omega$ SST)	1222	22%

demonstrates that the acoustic sources are predominantly generated by the von Kármán vortex street in the wake region and the Kelvin-Helmholtz instability in the free shear layer. The von Kárman vortex street can occur when the fluid flows around a blunt body, while the Kelvin-Helmholtz instability arises when a velocity difference is present between two fluid layers. Observing the acoustic sources obtained from the RANS model, shown in Fig. 8.6, we can discover that no acoustic sources in the free shear layer is predicted, while only a small portion of the acoustic sources in the wake region is produced. Compared with the RANS model, the LNS model behaves better in the wake region, while only a part of the acoustic sources caused by the Kelvin-Helmholtz instability is predicted, as shown in Fig. 8.7.

It is also of great interest to determine which part of the acoustic sources contribute to the fundamental frequency and why there is a mismatch for the LNS model in Fig. 8.4.

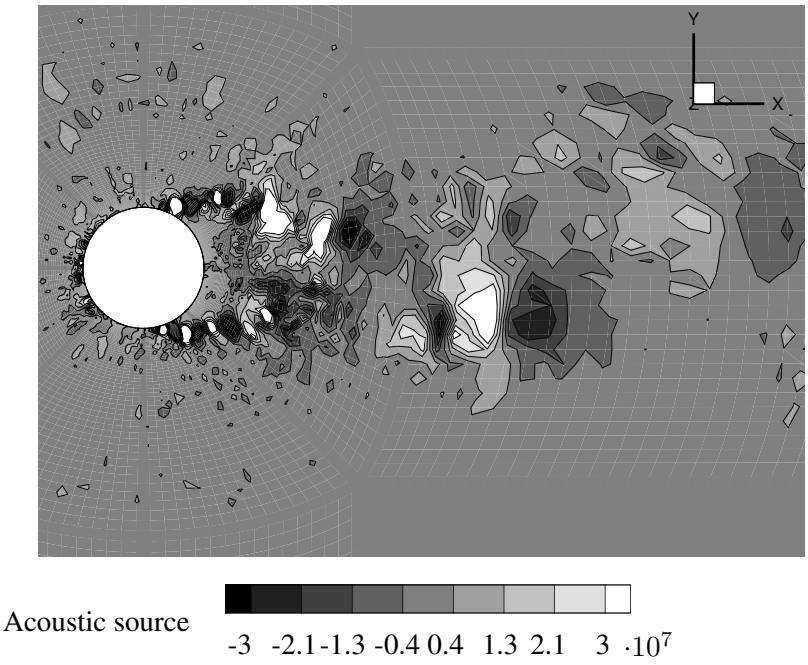

Figure 8.5: Acoustic source of the LES model in [Pa/s] for the flow past the circular cylinder.

The shedding frequency of the von Kármán vortex street is given by

$$f_{\mathrm{vK}} = \mathrm{St} \cdot \frac{u}{D}, \tag{8.2}$$

with the upstream velocity u, the diameter D and the Strouhal number St [95]. The Strouhal number is dependent on the Reynolds number and in this case (Re =6×10^4), it is around 0.186 according to [22]. Therefore, the frequency of the von Kármán vortex street can be estimated to be

$$f_{\mathrm{vK}} = 0.186 \cdot \frac{68.6}{0.0125} = 1020 \text{ Hz}. \tag{8.3}$$

The relationship of the frequency of the Kelvin-Helmholtz instability f_{S} and the frequency of the von Kármán vortex street is given as [7]

$$\frac{f_{\mathrm{S}}}{f_{\mathrm{vK}}} \propto Re^{0.5}. \tag{8.4}$$

Hence, the frequency of the Kelvin-Helmholtz instability is in this test approximately 2.5×10^5 Hz. It can be therefore concluded that the fundamental frequency is largely caused by the von Kármán vortex street, and the Kelvin-Helmholtz instability plays a very small role in the SPL spectrum, since it is far beyond the range of human's perception.

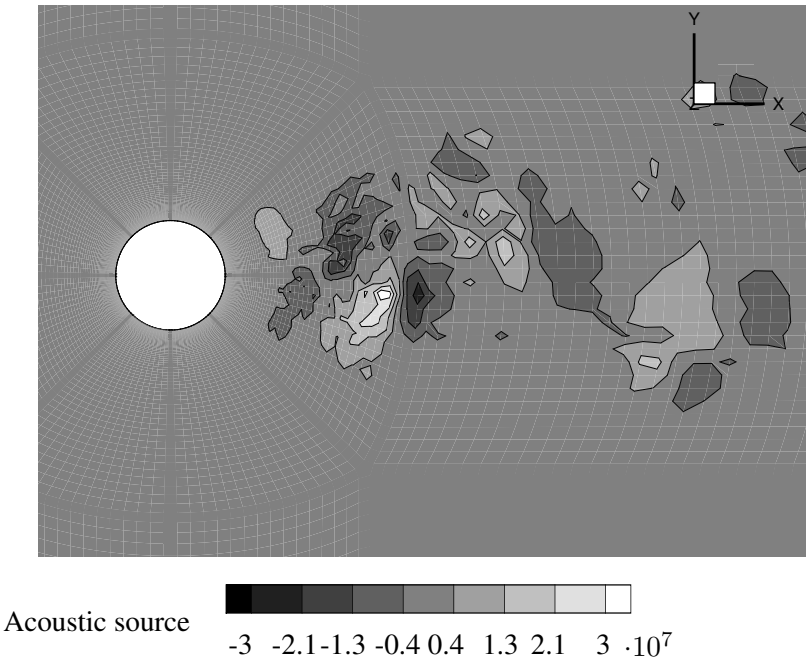

Figure 8.6: Acoustic source of the RANS model in [Pa/s] for the flow past the circular cylinder.

In order to explain the performance of the LNS model, the latency factor α, shown in Fig. 8.8 is examined. It can be seen that the whole domain is dominated by α close to 0, meaning that the majority of the computational domain is simulated by an LES model or even a quasi-DNS model. In the boundary layer, the free shear layer and part of the wake region, where α is increased up to 0.5-1, the LNS model acts in a RANS mode.

It can be inferred that the turbulence in the free shear layer is not resolved adequately, leading to the misestimation of the Kelvin-Helmholtz instability. Breuer et al. [10] also found that the DES model is not able to capture the Kelvin-Helmholtz instability at a flat plate, no matter how fine the grid is. Although the misbehaviour of the hybrid LES/RANS model in the free shear layer is irrelevant for the SPL spectrum, however, it is still important to keep in mind that this drawback of the hybrid LES/RANS models could be a reason of the misestimation in the spectrum when the frequency of the Kelvin-Helmholtz instability lies in the relevant range.

In the following, it is investigated if the synthetic method can improve the spectrum results of the acoustic simulation. Figure 8.9 shows the acoustic sources obtained from the LNS model with the synthetic method. It can be seen that more small scale sources are present, scattered randomly in the field. However, no significant improvement in the shear layer and in the wake can be determined. By comparing the SPL of the LNS model with and without the use of the synthetic method, shown in Fig. 8.10, it can be

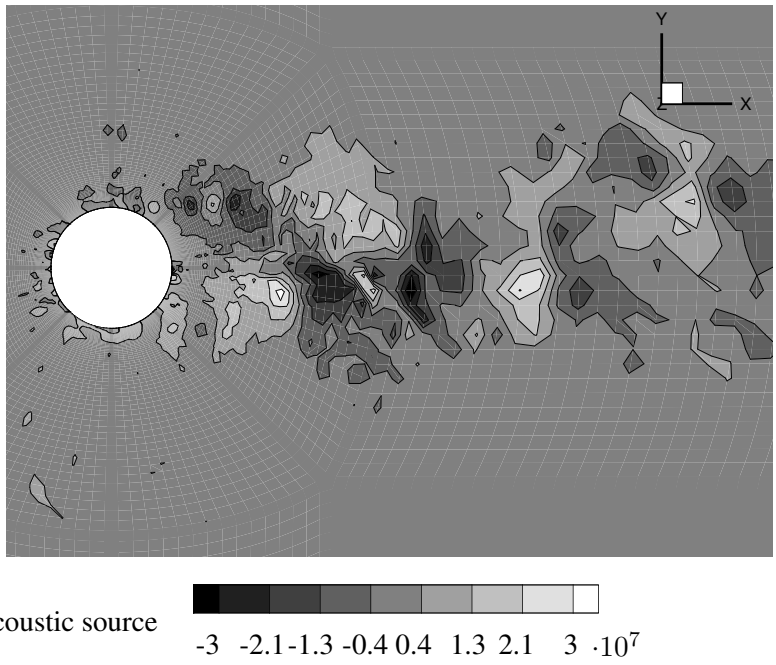

Figure 8.7: Acoustic source of the LNS model in [Pa/s] for the flow past the circular cylinder.

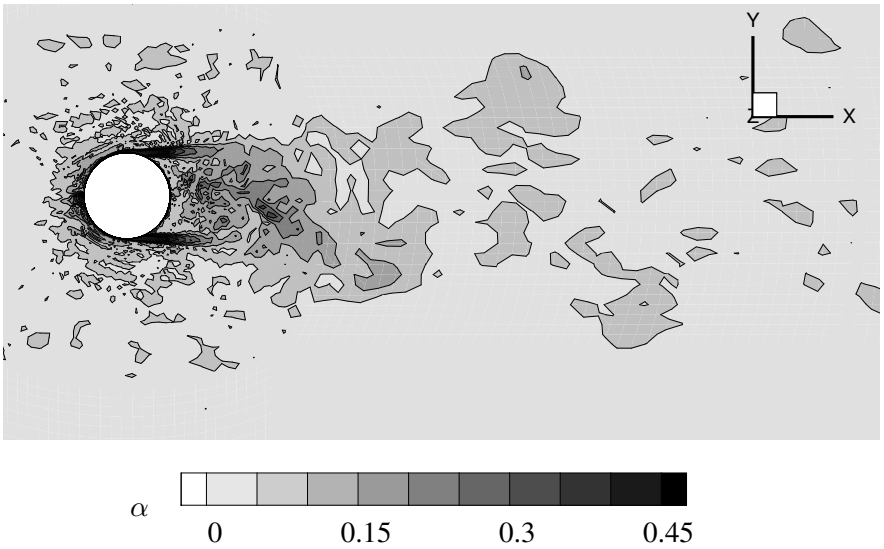

Figure 8.8: Latency factor α of the LNS turbulence model in the test case of the flow past a circular cylinder

seen that the synthetic method is able to increase the spectrum in the high frequency region. However, the SPL result when using the synthetic method is even farther from

the experimental result. Therefore, it remains questionable if the synthetic method is able to generate physically correct fluctuations. Similar results were published in [31] by the author.

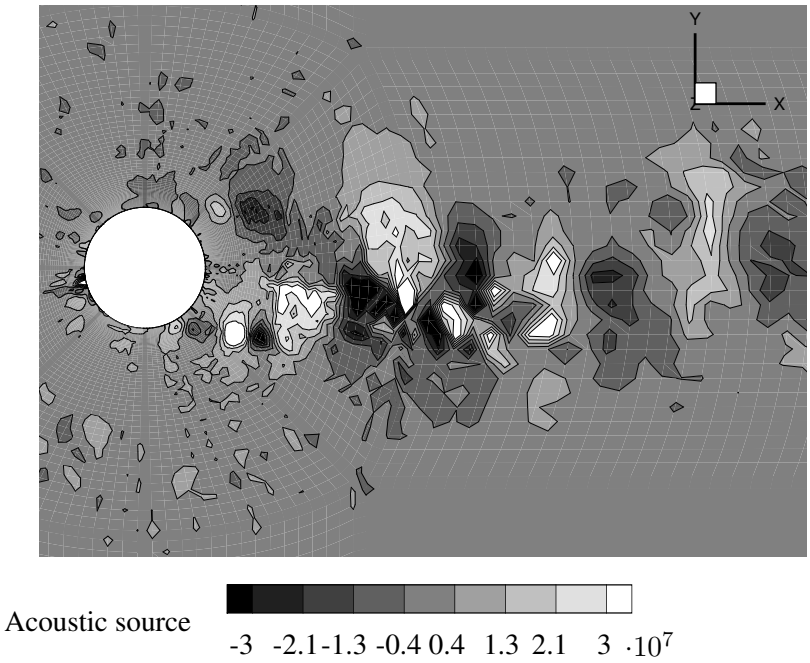

Figure 8.9: Acoustic source of LNS model with the synthetic method in [Pa/s]

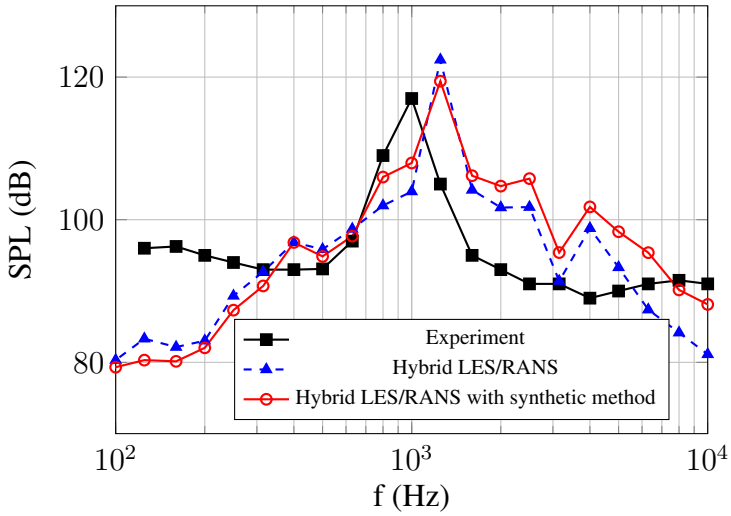

Figure 8.10: Comparison of the SPL of the hybrid LES/RANS model with and without the synthetic method.

Table 8.5: Analysis of the computational time of the LNS model and the LES model.

	CPUs	Computational time (hours)	core*hours
LNS	45	15.3	688
LES	45	55	2475

Computational efficiency of the LNS model The advantage of hybrid LES/RANS models is the lower computational cost in comparison to the LES model. In order to quantitatively illustrate the computational efficiency of the hybrid models, the computational time of the LNS model is compared with that of the LES model. As listed in Table 8.5, the simulation of the LES model is conducted using 45 CPUs, which takes 55 hours for the first 10000 time steps. The LNS model distributes the simulation also on 45 CPUs, resulting in a total computational time of 15.3 hours for the first 10000 time steps.

Figure 8.11 shows the core*hours of both models, which is the product of the number of CPUs and the number of hours. The total computational time of the LNS model is only 28% of that of the LES model, which is strongly dependent on the number of CVs of both models. The total numbers of CVs of the LNS model and the LES model are 1.2×10^6 and 5.6×10^6, respectively, indicating that the ratio of the number of CVs is 21%. The computational time decreases disproportionately with the number of CVS. The reason is that the LNS model is based on the $\zeta - f$ model, which solves two additional equations and therefore consumes extra computational time.

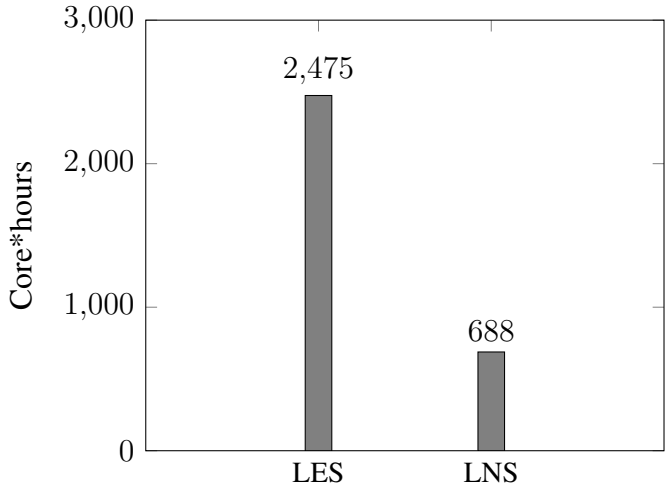

Figure 8.11: Comparison of the computational time of the LNS model and the LES model.

Table 8.6: Analysis of the computational time of the integrated solver and the coupled solver.

	CPUs	Computational time (hours)	core*hours
Integrated solver	33	30	990
Coupled solver	45	15.3	688

Computational efficiency of the new coupling strategy In the following, the computational efficiency of the new coupling strategy is investigated by comparing the computational cost of the coupled acoustic solver and the existing integrated acoustic solver. For the simulation of the integrated acoustic solver, a new grid is created, which has the same size as the acoustic grid for the coupled acoustic solver, shown in Fig. 8.2. The discretization of this grid is oriented towards the flow grid of the coupled solvers, shown in Fig. 8.1. As a result, the grid for the integrated solver has totally 2.2×10^6 CVs.

As listed in Table 8.12, the simulation on the integrated solver is conducted using 33 CPUs, which consumes totally 990 core*hours for the first 10000 time steps. The coupled solver distributes the simulation on 45 CPUs and takes 688 core*hours for the same time steps. The total core*hours of both strategies are compared in Fig. 8.12. The new coupling strategy saves approximately 30% computational time compared to the existing integrated acoustic solver.

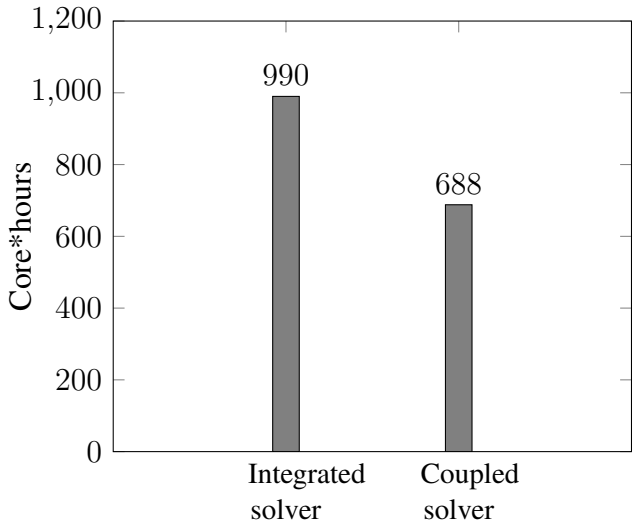

Figure 8.12: Comparison of the computational time of the integrated solver and the coupled solver.

8.2 Flow over NACA 0012 airfoil

In this test case, the airfoil NACA 0012 is simulated using different turbulence models at three different angles of attack (AoA): 0°, 10.8° and 14.4°. These AoA are chosen especially to examine the performance of the turbulence models for attached flows and separated flows. The flow velocity is set to 39.6 m/s, resulting in a Mach number of 0.12. The Reynolds number is approximately 6.8×10^4, based on the chord length 2.54 cm.

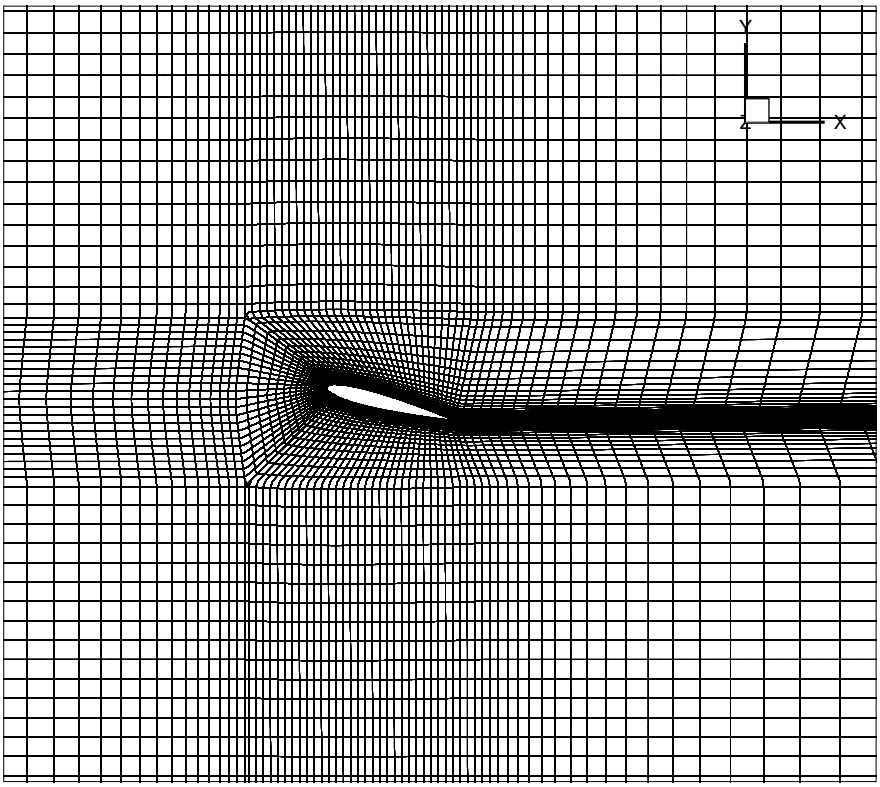

Figure 8.13: Discretization of the flow domain of the NACA 0012 airfoil (every 2 lines are shown)

Three turbulence models are investigated here: the LES mode, the VLES model and the LNS model. Two different O-type structured grids are applied for the flow simulations of the LES model and the hybrid LES/RANS models. The spacing sizes of the grid for the LES model in the streamwise, spanwise and wall normal directions fulfil the requirements $\Delta x^+ = 60$, $\Delta z^+ = 20$ and $\Delta y^+ = 1$ [35], while the grid for the hybrid LES/RANS models is coarsened to $\Delta x^+ = 200$, $\Delta z^+ = 60$ and $\Delta y^+ = 2$. Hence, the LES model uses a grid with 5×10^6 CVs, while the grid for the VLES model and the LNS model has totally 1.6×10^6 CVs. For the acoustic domain, the same discretization with 3.4×10^5 CVs is applied. The meshes used for different turbulence models are summarized in Table 8.7.

Table 8.7: Grid resolution for LES and hybrid RANS/LES models.

No.	Model	Δx^+	Δy^+	Δz^+	CVs (flow)	CVs (acoustics)
1	LES	60	1	20	5 million	0.34 million
2	VLES	200	2	60	1.6 million	0.34 million
3	LNS	200	2	60	1.6 million	0.34 million

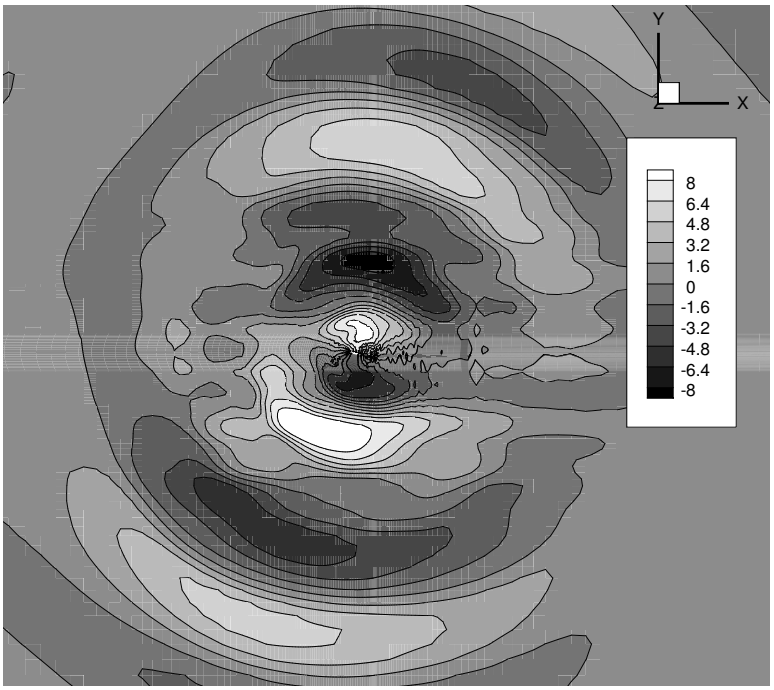

Figure 8.14: Instantaneous acoustic pressure of NACA 0012 at AoA=14.4°

The instantaneous acoustic pressure obtained by the LES model for the AoA=14.4° is shown in Fig. 8.14. A dipole pattern with a slight rotation corresponding to the AoA can be observed. The LES model is first validated against experimental data extracted from [11]. Figure 8.15 presents the comparison of the scaled simulation results conducted using the LES model with the experimental data. The simulation results are scaled down by about 30 dB so that the maximum is identical with that of the experimental data. A similar scenario was observed by Kornhaas [40]. A possible reason for this overestimation is the periodic boundary condition in the z-direction. After the scaling, the simulation results of the LES model agree quite well with the experimental data. Thus, the LES model is seen as validated in this case and can be used as a reference in the following discussion.

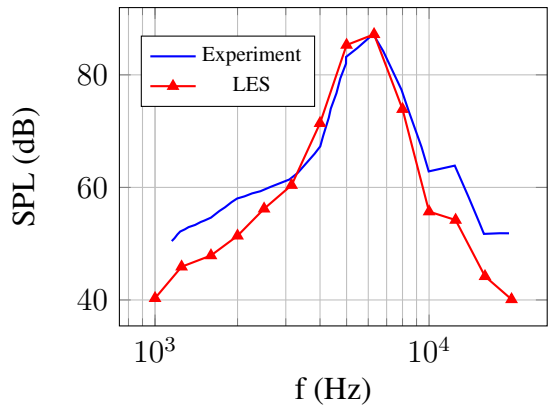

(a) AoA=0°.

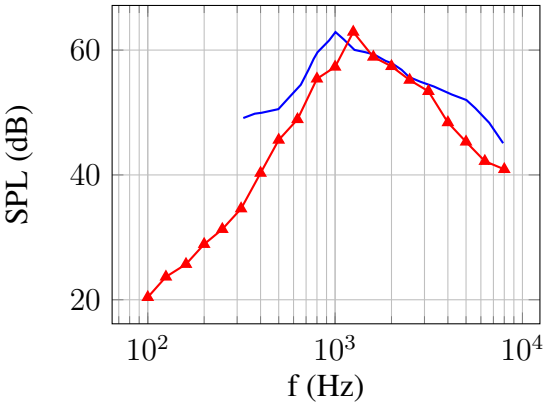

(b) AoA=10.8°.

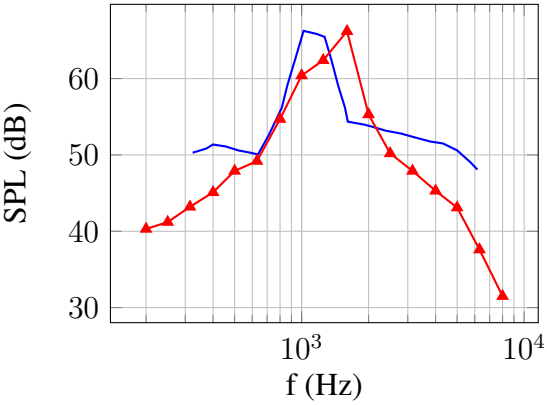

(c) AoA=14.4°.

Figure 8.15: Comparison of the SPL of the LES model with the experimental data.

Similar to the cylinder test case, it is here also very important to observe the acoustic

sources predicted by different turbulence models. As can be seen from Fig. 8.16, the LES simulation provides the maximal values at the trailing edge. The leading edge here does not contribute to the noise generation. Compared with the LES model, the LNS and the VLES models both underestimate the source term in the trailing edge region and overestimate the source term on the airfoil surface. The application of the RANS mode in the boundary layer and wake region is presumably the reason leading to the misestimation in these regions.

Figure 8.19 displays the latency factor α for the LNS model. In the shear layer and the wake region, it is seen that α is gradually increased up to 1, indicating that the LNS operates in these regions mainly as a RANS model, while in the remaining regions, it is switched to a DNS model.

When the Reynolds number is in the range of 5.5×10^4 to 2.1×10^5, the flow separation occurs at 9.25° [65]. Therefore, when the AoA is increased to 10.8°, the flow should separate from the airfoil. This phenomenon is confirmed by the LES simulation, shown in Fig. 8.17. The VLES model and the LNS model provide totally different simulation results. The VLES model reproduces the acoustic sources generated by the Kelvin-Helmholtz instability quite well, while the flow separation is not predicted. The LNS model correctly predicts the flow separation, however, the acoustic sources in the free shear layer and in the wake region are significantly less accurate than that of the LES model. These behaviour of the hybrid LES/RANS models can be explained using the distribution of the RANS and LES modes. While the LNS model uses sufficient RANS mode in the shear layer and the wake region, the VLES uses too much DNS mode here. Therefore, the boundary layer in the VLES simulation is not adequately resolved, since the grid here is not sufficiently fine.

When the AoA reaches $14.4°$, all three turbulence models are capable to predict the flow separation correctly, as shown in Fig. 8.18. The VLES model provides here more small scale structures, while the LNS model predicts only large scale sources. This is, again, because of the different amount of the RANS and DNS contents in the shear layer and the wake region.

The directivity characteristics of the acoustic pressure is obtained by collecting the acoustic pressure at 36 different points with the same distance to the airfoil's leading point but with different angles starting from 10° to 360°. Figure 8.20 shows the directivity characteristics from different turbulence models. A dipole pattern is observed for all three turbulence models, when AoA=0°. When the flow starts to separate from the airfoil (AoA=10.8°), the LNS model delivers better prediction than the VLES model. When the flow is fully separated (AoA=14.4°, both the LNS model and VLES reproduce the directivity characteristics correctly.

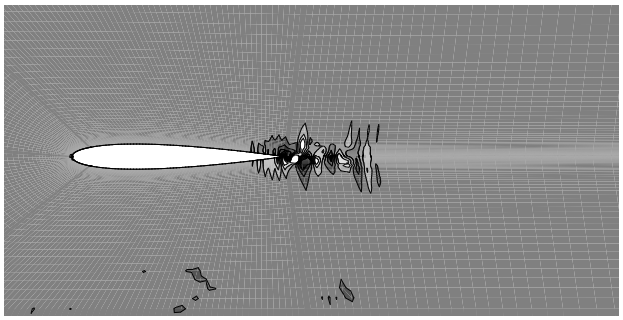

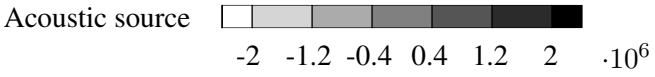

(a) Acoustic source of LES model in [Pa/s]

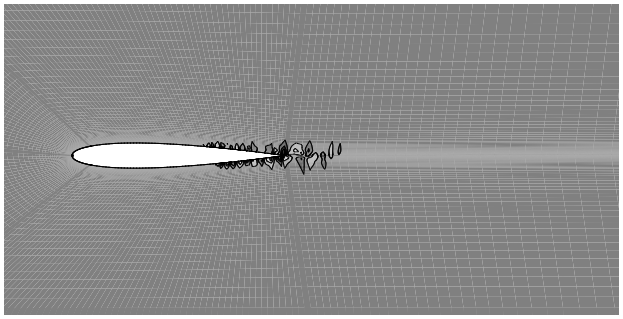

(b) Acoustic source of VLES model in [Pa/s]

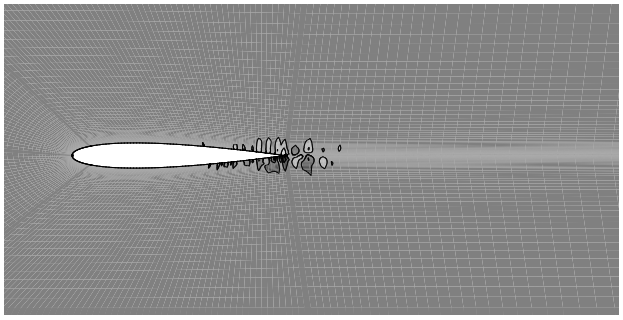

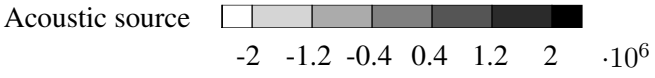

(c) Acoustic source of LNS model in [Pa/s]

Figure 8.16: Acoustic source of different turbulence models for AoA=0°

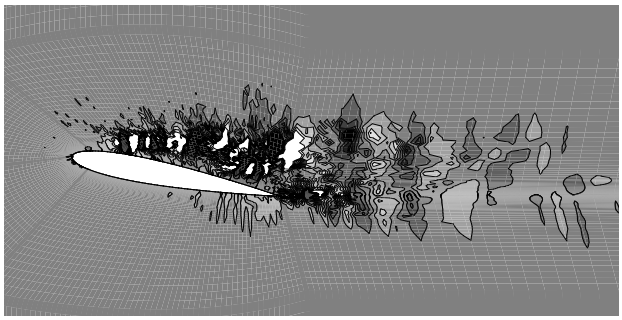

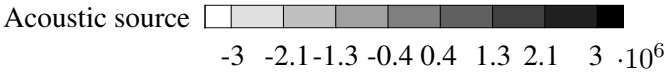

(a) Acoustic source of LES model in [Pa/s]

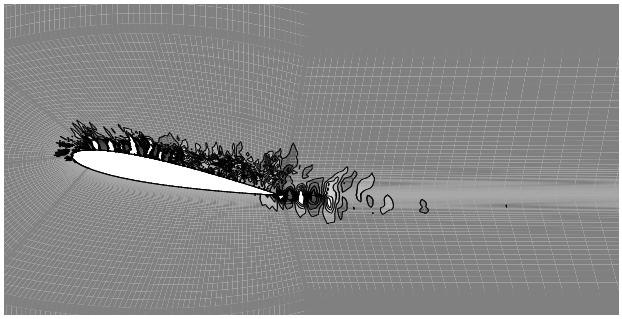

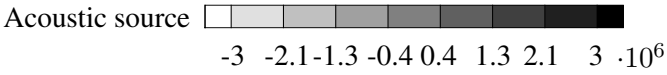

(b) Acoustic source of VLES model in [Pa/s]

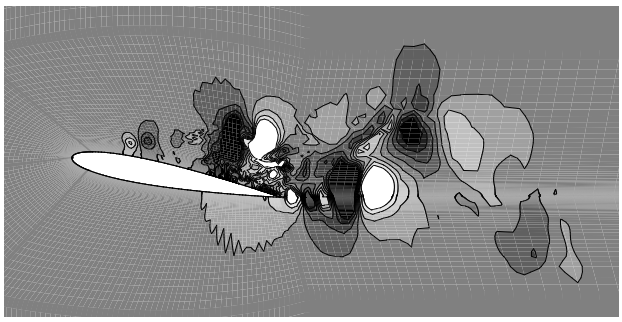

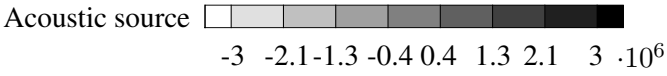

(c) Acoustic source of LNS model in [Pa/s]

Figure 8.17: Acoustic source of different turbulence models for AoA=10.8°

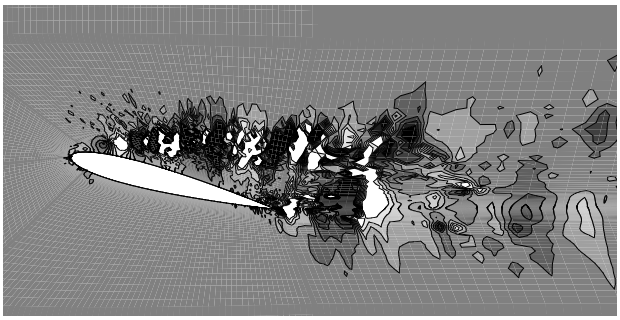

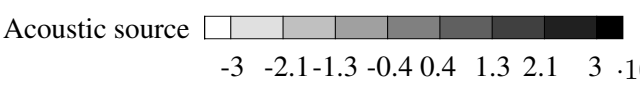

(a) Acoustic source of LES model in [Pa/s]

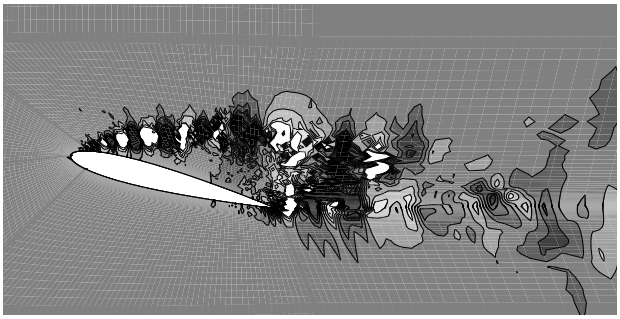

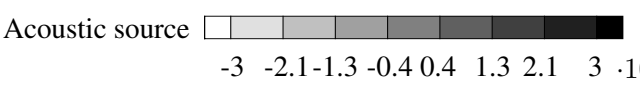

(b) Acoustic source of VLES model in [Pa/s]

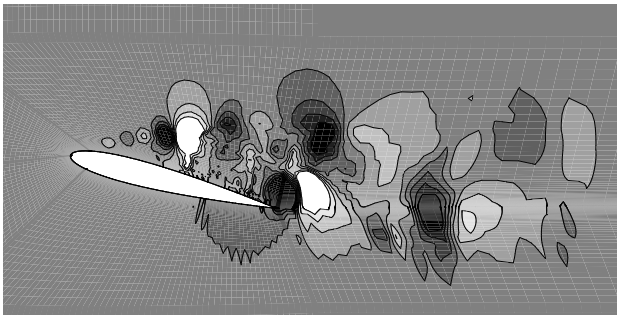

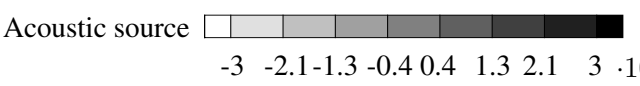

(c) Acoustic source of LNS model in [Pa/s]

Figure 8.18: Acoustic source of different turbulence models for AoA=14.4°

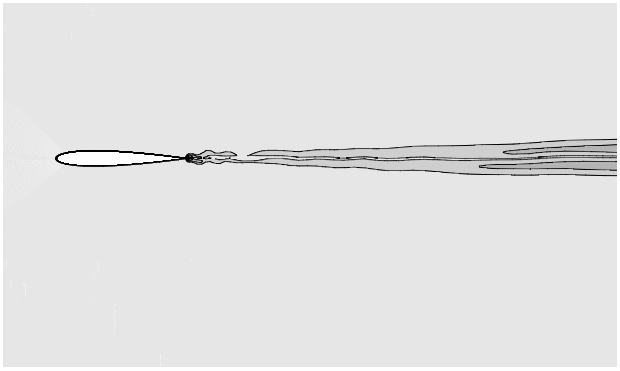

(a) AoA 10.8°

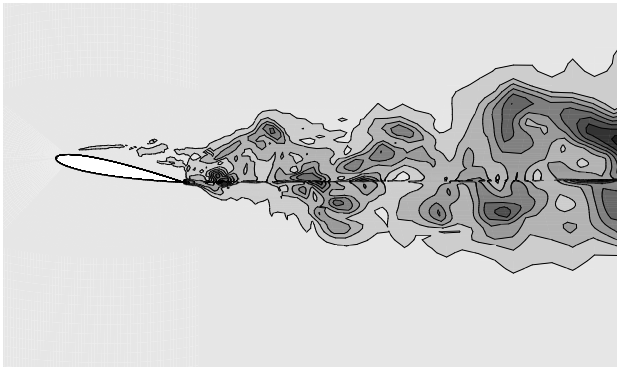

(b) AoA 10.8°

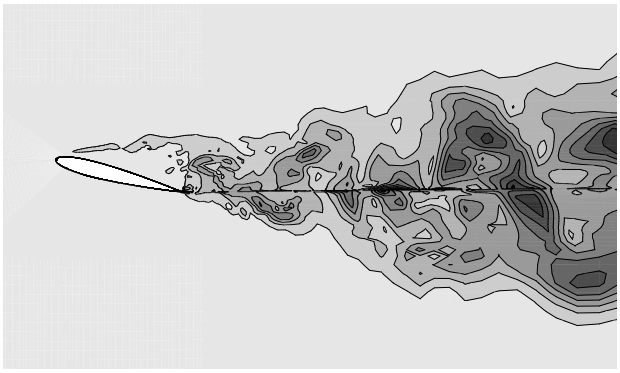

(c) AoA 14.4°

Figure 8.19: The latency factor α in the LNS model

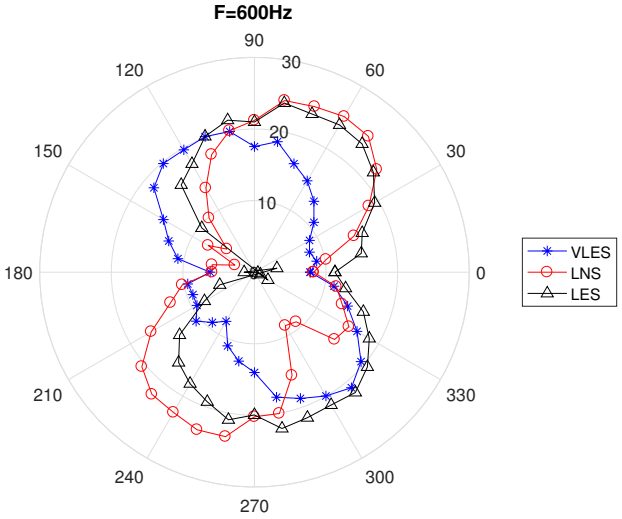

(a) AoA=0°

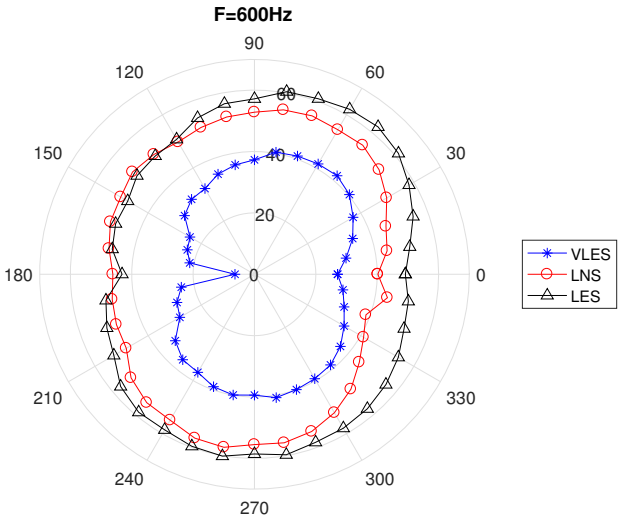

(b) AoA=10.8°

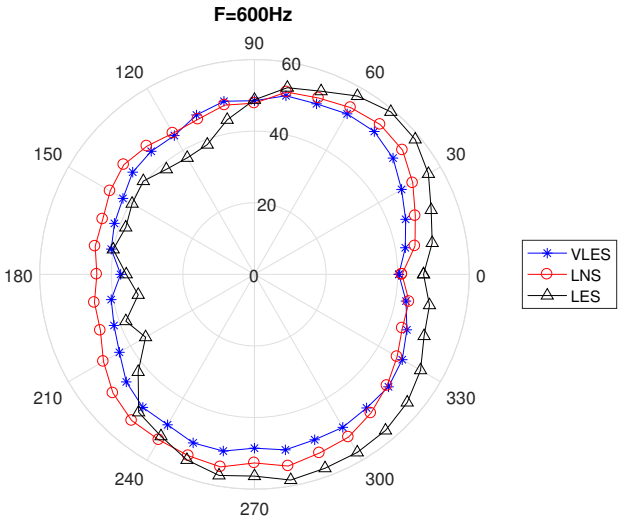

(c) AoA=14.4°

Figure 8.20: Directivity characteristics of different turbulence models [32].

CHAPTER 9

SUMMARY AND OUTLOOK

9.1 Summary

In this dissertation, aeroacoustic simulations coupled with hybrid LES/RANS turbulence modeling strategies are investigated. For this purpose, a framework for efficient aeroacoustic simulations in turbulent flows was developed in the in-house CFD solver FASTEST. A new coupling strategy between the flow solver and the acoustic solver was implemented, which enables the application of different computational domains and different space discretizations for the flow and the sound. By doing so, the computational cost for the acoustic simulation is substantially reduced compared with the existing coupling strategy. The new implemented coupling part was verified using two test cases. In the first test case, the acoustic sources were given by an analytical function. It was shown that the interpolation operation works correctly, since the error of the interpolation decreases with an order of approximately 2 as the number of CVs increases. In the second test case it was further verified that the time-dependent acoustic variables obtained from the coupled acoustic solver converge correctly to the reference values as the number of CVs increases.

The existing modeling library of FASTEST was extended by a new hybrid LES/RANS turbulence model, the limited numerical scales (LNS) model. The latency factor determining which part uses RANS and which uses LES models was first derived for the Chien $k-\epsilon$ and the $\zeta-f$ based LNS models. Especially the $\zeta-f$ based LNS model yielded quite satisfactory results, owing to the introduction of some scales of anisotropy in the turbulence modeling. Thus, the $\zeta-f$ bases LNS model was applied in the further aeroacoustic simulations.

The LES model resolves the large eddies and implicitly accounts for the small scale

structures, indicating that a part of the high frequency noise cannot be reproduced by the LES model. The hybrid LES/RANS model uses RANS models in certain regions to reduce the computational cost. It can be expected that the range of scales obtained from the hybrid turbulence models is further narrowed. In order to predict the noise from the unresolved scales, a synthetic method capable of randomly generating small scale motions using the local turbulence length scales and time scales was implemented, which was then verified by means of a benchmark channel flow with $Re_\tau = 395$. The verification illustrated that the synthetic method implemented here is able to generate small scale fluctuations and improve the spectral results significantly.

With the help of a cylinder test case, it was shown, that the hybrid LNS model delivers more accurate sound spectra than the RANS model, even when the same computational discretization was applied for both models. By observing the acoustic sources provided by the LNS model, the RANS model and the reference LES model, some insightful conclusions were drawn. In the free shear layer, the RANS model fails to provide any acoustic sources, while the LNS model performs only slightly better than the RANS model in this region. The reason is that the latency factor of the LNS model is approximately 0.5, meaning that the LNS model here is actually somewhere between a pure RANS model and a pure DNS model. The use of RANS contents in the shear layer leads to the under-prediction of the acoustic sources. The LNS model reproduces the sound spectrum quite accurately with only minor mismatches in the region around the fundamental frequency. Again, this mismatch is caused by the use of the RANS mode in the wake region, which leads to under-prediction of acoustic sources in the von Kármán street vortex.

The synthetic method was then used to examine its performance in the acoustic simulation. It was determined that random small scale acoustic sources were successfully generated with the application of the synthetic method, and the spectrum in the high frequency region is increased. However, the spectrum obtained using the synthetic method is even farther from the experimental spectrum. Therefore, the physical correctness of the generated synthetic fluctuations is still questionable.

A test case with the NACA 0012 airfoil was used to compare the LNS model and the VLES model. The LNS model here uses more RANS contents in the near wall region and the shear flow region than the VLES model. Hence, the VLES model provides more detailed information in terms of acoustic sources. On the other hand, the use of too much LES contents in the near wall region and the shear flow region in the VLES model causes another severe problem, namely the VLES fails to predict the separation of flow when the angle of attack is set to 10.8°.

9.2 Outlook

In the present work, it has been shown that the hybrid LES/RANS models are able to provide accurate results while saving a large amount of computational time compared to the LES models. For the future work, it would be interesting to investigate the performance of the hybrid LES/RANS models with fluid-structure-aeroacoustics-interaction (FSA) problems. The application of the hybrid LES/RANS models in the fluid-structure-interaction problems was discussed in [1, 39, 87], where excellent results were reported. Therefore, the hybrid LES/RANS models are expected to be also advantageous in the more general FSA problems.

In addition, the aeroacoustic simulation consisting of a two phase fluid would be a challenging task for the hybrid LES/RANS models. In particular, the velocity differences on the phase surface would cause a Kelvin-Helmholtz instability, which represents one of the difficulties for the hybrid LES/RANS models.

LIST OF FIGURES

LIST OF TABLES

BIBLIOGRAPHY

[1] A. Ali. *On the simulation of turbulent fluid-structure interaction*. PhD thesis, TU Darmstadt, Darmstadt, 2017.

[2] G. K. Batchelor. *An Introduction to Fluid Dynamics*. Cambridge Mathematical Library. Cambridge University Press, 2000.

[3] P. Batten, U. Goldberg, and S. Chakravarthy. Interfacing statistical turbulence closures with large eddy simulation. *AIAA Journal*, 43(3):485–492, 2004.

[4] P. Batten, U. Goldberg, and Chakravarthy S. Lns - an approach towards embedded les. *40th AIAA Aerospace Sciences Meeting & Exhibit*, 2002.

[5] P. Batten, U. Goldberg, and Chakravarthy S. Reconsructed sub-grid methods for acoustics predictions at all reynolds numbers. *8th AIAA Aeroacoustics Conference & Exhibit*, 2002.

[6] R. D. Blevins. *Flow-induced vibration*. Van Nostrand Reinhold Co., Inc., 1990.

[7] M. S. Bloor. The transition to turbulence in the wake of a circular cylinder. *Journal of Fluid Mechanics*, 19(2):290–304, 1964.

[8] V. Bonneau, C. Polacsek, L. Castillon, J. Marty, Y. Gervais, and S. Moreau. Turbofan broadband noise predictions using a 3-d zdes rotor blade approach. *Aeroacoustics Conferences, (AIAA 2016-2950)*, 2016.

[9] J. Boussinesq. *Théorie de L'Écoulement Tourbillonnant Et Tumultueux Des Liquides Dans Les Lits Rectilignes a Grande Section*. Gauthier-Villars, 1897.

[10] M. Breuer, N. Jovičić, and K. Mazaev. Comparison of des, rans and les for the separated flow around a flat plate at high incidence. *International Journal for Numerical Methods in Fluids*, 41:357 – 388, 2003.

[11] T. F. Brooks, D. S. Pope, and M. A. Marcolini. *Airfoil Self-noise and Prediction*. NASA reference publication. National Aeronautics and Space Administration, Office of Management, Scientific and Technical Information Division, 1989.

[12] C. Bailly, C. Bogey, and O. Marsden. Progress in direct noise computation. *International Journal of Aeroacoustics*, 9(1):123–143, 2010.

[13] C. Bailly and D. Juvé. A stochastic approach to compute subsonic noise using linearized euler equations. *AIAA Paper*, pages 99–1872, 1999.

[14] C.-Y. Chang and S. Jakirlić. Swirling flow in a tube with varialby-shaped outlet orifices: An les and vles study. *International Journal of Heat and Fluid Flow*, 49:28–42, 2014.

[15] K.-Y. Chien. Predictions of channel and boundary-layer flows with a low-reynolds-number turbulence model. *AIAA Journal*, 20(1):33 – 38, 1982.

[16] N. Curle. The influence of solid boundaries upon aerodynamic sound. *Proceedings of the Royal Society (London)*, 231(A):505–514, 1955.

[17] J. W. Deardorff. The use of subgrid transport equations in a three-dimensional model of atmospheric turbulence. 95:429, 09 1973.

[18] P. Durbin. On the k-3 stagnation point anomaly. *International Journal of Heat and Fluid Flow*, 17(1):89–90, 1996.

[19] B. Etkin. Acoustic Radiation from a Stationary Cylinder in a Fluid Stream (Aeolian Tones). *Acoustical Society of America Journal*, 29:30–36, 1957.

[20] J. A. Fay. *Introduction to Fluid Mechanics*. MIT Press, 1994.

[21] J. H. Ferziger and M. Peric. *Computational Methods for Fluid Dynamics*. Springer Berlin Heidelberg, 2012.

[22] U. Fey and M. K˙ A new strouhal-reynolds-number relationship for the circular cylinder in the range 47<re<2×10^5. *Physics of Fluids*, 1998.

[23] F. Flemming, A. Sadiki, and J. Janicka. Investigation of combustion noise using a les/caa hybrid approach. *Proceedings of the Combustion Institute*, 31(2):3189 – 3196, 2007.

[24] J. Fröhlich, C. P. Mellen, W. Rodi, L. Temmerman, and M. A. Leschziner. Highly resolved large-eddy simulation of separated flow in a channel with streamwise periodic constrictions. *Journal of Fluid Mechanics*, 526.

[25] J. Fröhlich and D. Terzi. Hybrid les/rans methods for the simulation of turbulent flows. *Progress in Aerospace Sciences*, 44(2008):349–377, 2008.

[26] P. Germano, U. Piomelli, P. Moin, and W. H. Cabot. A dynamic sub-grid scale eddy viscosity model. *Physics of Fluids*, 7(3):1760–1765, 1991.

[27] S. S. Girimaji. Partially-averaged navier-stokes model for turbulence: A reynolds-averaged navier-stokes to direct numerical simulation bridging method. *ASME. J. Appl. Mech*, 73(3):413–421, 2005.

[28] K. Hanjalić, M. Popovac, and M. Hadžiabdić. A robust near-wall elliptic-relaxation eddy-viscosity turbulence model for cfd. *International Journal of Heat and Fluid Flow*, 25(6):1047–1051, 2004.

[29] J. C. Hardin and D. S. Pope. An acoustic/viscous splitting technique for computational aeroacoustics. *Theoretical and Computational Fluid Dynamics*, 6(5):323–340, 1994.

[30] X. Huang and M. Schäfer. On the simulation of aerodynamic noise with different turbulence models. In M. Papadrakakis, V. Papadopoulos, G. Stefanou, and V. Plevris, editors, *ECCOMAS Congress 2016*, volume 1, pages 7599–7608, Crete, Greece, 2016.

[31] X. Huang and M. Schäfer. Investigation of advanced turbulence modeling approaches for aeroacoustic problems. In M. Papadrakakis, E. Oñate, and B. Schrefler, editors, *COUPLED PROBLEMS 2017*, pages 1092–1099, Rhodes Island, Greece, 2017.

[32] X. Huang and M. Schäfer. An investigation of airfoil noise prediction using hybrid les/rans models. In *4th International Conference on Computational Engineering (ICCE 2017)*, Darmstadt, Germany, 2017.

[33] J. H. Humphreys. On a circular cylinder in a steady wind at transition reynolds numbers. *Jounal of Fluid Mechanics*, 9:603–612, 1960.

[34] W. P. Jones and B. Launder. The prediction of laminarization with a two-equation model of turbulence, ". 5:301–314, 01 1973.

[35] H. Kaltenbach and H. Choi. Large-eddy simulation of flow around an airfoil on a structured mesh. *Center for Turbulence Research Annual Research Briefs*, 49:51–60, 1995.

[36] T. Von Kármán. *Mechanische Ähnlichkeit und Turbulenz*. Sonderdrucke aus den Nachrichten von der Gesellschaft der Wissenschaften zu Göttingen : Mathematisch-physische Klasse. Weidmannsche Buchh., 1930.

[37] A. N. Kolmogorov. The local structure of turbulence in incompressible viscous fluid for very large reynolds numbers. *Doklady Akademiia Nauk SSSR*, 1941.

[38] A. N. Kolmogorov. On degeneration of isotropic turbulence in an incompressible viscous liquid. *Doklady Akademiia Nauk SSSR*, 1941.

[39] A. Kondratyuk. *Investigation of the very large eddy simulation model in the context of fluid-structure interaction*. PhD thesis, TU Darmstadt, Darmstadt, 2017.

[40] M. Kornhaas. *Effiziente numerische Methoden für die Simulation aeroakustischer Probleme mit kleinen Machzahlen*. PhD thesis, TU Darmstadt, Aachen, 2012. Zugl.: Darmstadt, Techn. Univ., Diss., 2011.

[41] M. Kornhaas, M. Schäfer, and D. C. Sternel. Efficient numerical simulation of aeroacoustics for low mach number flows interacting with structures. *Computational Mechanics*, 55:1143–1154, 2015.

[42] R. B. Langtry, E. A. Gren, J. V. Larssen, and P. R. Spalart. Evaluation of structured and unstrucutred grids for detached eddy simulation of flap edge noise. *15th AIAA/CEAS Aeroacoustics Conference (30th AIAA Aeroacoustics Conference)*, 2007.

[43] A. Leonard. Energy cascade in large eddy simulations of turbulent fluid flow. 18A:237–248, 01 1974.

[44] R. J. Leveque. *Finite volume methods for hyperbolic problems*. Cambridge University Press, Cambridge, 2002.

[45] M. J. Lighthill. On sound generated aerodynamically. i. general theory. *Proceedings of the Royal Society of London. Series A, Mathematical and Physical Sciences*, 211(1107):564–587, 1952.

[46] M. J. Lighthill. On sound generated aerodynamically. ii. turbulence as a source of sound. *Proceedings of the Royal Society of London. Series A, Mathematical and Physical Sciences*, 222(1148):1–32, 1954.

[47] W. D. McComb. *The Physics of Fluid Turbulence*. Oxford Engineering Science Series. Clarendon Press, 1992.

[48] F. R. Menter. Zonal two equation $k-\omega$ turbulence models for aerodynamic flows. 1993, 02 1993.

[49] F. R. Menter. Two-equation eddy-viscosity turbulence models for engineering applications. *AIAA Journal*, 32(8):1598–1605, 1994.

[50] F. R. Menter and Y. Egorov. The scale-adaptive simulation method for unsteady turbulent flow predictions. part 1: Theory and model description. *Flow, Turbulence and Combustion*, 85(1):113–138, 2010.

[51] F. R. Menter, M. Kuntz, and R. Langtry. Ten years of industrial experience with the sst turbulence model. *Turbulence, heat and mass transfer*, 4:625–632, 2003.

[52] F. R. Menter, J. Schütze, and M. Gritskevich. Global vs. zonal approaches in hybrid rans-les turbulence modelling. In *Progress in Hybrid RANS-LES modelling. Notes on Numerical Fluid Mechanics and Multidisciplinary Design*.

[53] C. Mockett. *A comprehensive study of detached-eddy simulation*. PhD thesis, TU Berlin, Berlin, 2009.

[54] Parviz Moin, , and Krishnan Mahesh. Direct numerical simulation: A tool in turbulence research. *Annual Review of Fluid Mechanics*, 30(1):539–578, 1998.

[55] R. D. Moser, J. Kim, and N. N. Mansour. Direct numerical simulation of turbulent channel flow up to re_τ=590. *Physics of Fluids*, 11(4):943–945, 1999.

[56] B. R. Munson, A. P. Rothmayer, and T. H.Okiishi. *Fundamentals of Fluid Mechanics, 7th Edition*. Wiley, 2012.

[57] Stephen B. Pope. *Turbulent Flows*. Cambridge University Press, 2000.

[58] L. Prandtl. Bericht über untersuchungen zur ausgebildeten turbulenz. 5(2), 1925.

[59] J. W. S. B. Rayleigh. *The Theory of Sound*. Number Bd. 1 in The Theory of Sound. Macmillan, 1894.

[60] T. Reimann. *Numerische Simulation von Fluid-Struktur-Interaktion in turbulenten Strömungen*. PhD thesis, TU Darmstadt, 2013.

[61] O. Reynolds. An experimental investigation of the circumstances which determine whether the motion of the water shall be direct or sinuous and of the law of resistance in parallel channels. *Philosophical Transactions of the Royal Society of London*, 174:935–982, 1883.

[62] O. Reynolds. On the dynamical theory of incompressible viscous fluids and the determination of the criterion. *Philosophical Transactions of the Royal Society of London A*, 186:123–164, 1895.

[63] L. F. Richardson. *Weather prediction by numerical process*. Cambridge University Press, 1922.

[64] S. Rienstra and A. Hirschberg. *An Introduction to Acoustics*. 08 2008.

[65] I. Rodríguez, O. Lehmkuhl, R. Borrell, and A. Oliva. Direct numerical simulation of a naca0012 in full stall. *International Journal of Heat and Fluid Flow*, 43:194–302, 2013.

[66] T. Rossing. A brief history of acoustics. *Springer Handbook of Acoustics.*, 2007.

[67] P. Sagaut. *Large Eddy Simulation for Incompressible Flows: An Introduction*. Scientific Computation. Springer Berlin Heidelberg, 2006.

[68] J. Sahu. *Unsteady numerical simulations of subsonic flow over a projectile with jet interaction*. AIAA, 2003.

[69] M. Schäfer. *Numerik im Maschinenbau*. Springer Verlag, Berlin, 1999.

[70] M. Schäfer. *Computational Engineering - Introduction to Numerical Methods*. Springer, 2006.

[71] H. Schlichting and K. Gersten. *Boundary-Layer Theory*. Springer, 9 edition, 2017.

[72] W. Z. Shen and J. N. Sörensen. Aeroacoustic modelling of low-speed flows. *Theoretical and Computational Fluid Dynamics*, 13(4):271–289, 1999.

[73] W. Z. Shen and J. N. Sörensen. Comment on the aeroacoustic formulation of hardin and pope. *AIAA Journal*, 37(1):141–143, 1999.

[74] J. Smagorinsky. General circulation experiments with the primitive equations i: The basic experiment. *Monthly weather review*, 91(3):99–163, 1963.

[75] G. D. Smith. *Numerical Solution of Partial Differential Equations: Finite Difference Methods*. Oxford Applied Mathematics and. Clarendon Press, 1985.

[76] P. R. Spalart. Detached-eddy simulation. *Annual Review of Fluid Mechanics*, 41(1):181–202, 2009.

[77] P. R. Spalart and S. Allmaras. A one-equation turbulence model for aerodynamic flows. In *30th Aerospace Sciences Meeting and Exhibit*.

[78] P. R. Spalart, S. Deck, M. L. Shur, K. D. Squires, and M. Kh Strelets. A new version of detached-eddy simulation, resistant to ambiguous grid densities. *Theoretical and Computational Fluid Dynamics*, 20(3):181–195, 2006.

[79] P. R. Spalart, W. Jou, M. Strelets, and S. Allmaras. Comments of feasibility of les for wings and on a hybrid rans/les approach. *Greyden Press*, 20(3):181–195, 1997.

[80] C. Speziale. Turbulence modeling for time-dependent rans and vles. 36(2):173–184, 1998.

[81] J. H. Spurk. *Strömungslehre: Einführung in die Theorie der Strömungen*. Sringer Verlag, Berlin, 4th edition, 1996.

[82] Christopher K. W. Tam. Computational aeroacoustics: Issues and methods. *AIAA Journal.*, 33(10):1788–1796, 1995.

[83] L. Temmerman and M. A. Leshziner. Large eddy simulation of separated flow in a streamwise periodic channel construction. *Proceedings of Turbulence and Shear Flow Phenomena Conferences.*, pages 399 – 404, 2001.

[84] H. Tennekes and J. L. Lumley. *A First Course in Turbulence*. A First Course in Turbulence. Pe Men Book Company, 1972.

[85] E. F. Toro. *Riemann Solvers and Numerical Methods for Fluid Dynamics*. Springer-Verlag, Berlin, 1997.

[86] P. G. Tucker. *Unsteady Computational Fluid Dynamics in Aeronautics*, volume 104. Springer Netherlands, Philadelphia, 2014.

[87] S. Türk. *Investigation of hybrid turbulence modeling techniques in the context of fluid-structure interaction*. PhD thesis, TU Darmstadt, Darmstadt, 2014.

[88] H. K. Versteeg and W. Malalasekera. *An Introduction to Computational Fluid Dynamics: The Finite Volume Method*. Pearson Education Limited, 2007.

[89] V. R. Voller and F. Porté-Agel. Moore's law and numerical modeling. *Journal of Computational Physics*, 179(2):698 – 703, 2002.

[90] C. A. Wagner, T. Hüttl, and P. Sagaut. *Large-Eddy Simulation for Acoustics*. Cambridge Aerospace Series. Cambridge University Press.

[91] L. Wang, C. Mockett, T. Knacke, and F. Thiele. Noise prediction of a rudimentary landing gear using detached-eddy simulation. In W. Haase, S. H. Peng, and D. Schwamborn, editors, *Progress in Hybrid RANS-LES Modelling. Notes on Numerical Fluid Mechanics and Multidisciplinary Design*, volume 117. Springer, Berlin, Heidelberg, 2012.

[92] M. Wang. Computation of trailing-edge noise at low mach number using les and acoustic analogy. *Center for Turbulence Research Annual Research Briefs*, pages 91–106, 1988.

[93] D. C. Wilcox. Reassessment of the scale-determining equation for advanced turbulence models. 26:1299–1310, 11 1988.

[94] D. C. Wilcox. *Turbulence Modeling for CFD*. Number Bd. 1 in Turbulence Modeling for CFD. DCW Industries, 2006.

[95] C. H. K. Williamson. Vortex dynamics in the cylinder wake. *Annual review of fluid mechanics*, 28:477 – 539, 1996.

[96] O. C. Zienkiewicz and R. L.Taylor. *The Finite Element Method: Fluid dynamics*. Referex collection.Mecánica y materiales. 5 edition, 2000.

[97] O. C. Zienkiewicz and R. L.Taylor. *The Finite Element Method: Solid mechanics*. Referex collection.Mecánica y materiales. 5 edition, 2000.

[98] O. C. Zienkiewicz and R. L.Taylor. *The Finite Element Method: The basis*. Referex collection.Mecánica y materiales. 5 edition, 2000.